Experimental Study on Structure Formation of Plasma Turbulence

金, 史良

https://hdl.handle.net/2324/2236281

出版情報：Kyushu University, 2018, 博士（理学）, 課程博士
バージョン：
権利関係：

Experimental Study on Structure Formation of Plasma Turbulence

Fumiyoshi Kin
Interdisciplinary Graduate School of Engineering Science, Kyushu University

February, 2019

Contents

Chapter 1

Introduction

1.1 Magnetically confined fusion

Nowadays, an energy problem has attracted much attention. Fossil fuels, like coal or oil, are known to be exhausted in about 100 years. Since energy demands in developing countries increases, greenhouse gas is also increasing, which leads to global warming. In Japan, an energy self-sufficiency rate is very low, and most of fuels are imported from foreign countries. In addition, people in Japan are getting more interested in safety energy source due to the big accidents in nuclear fission plants by Great East Japan earthquake in 2011. Therefore, large scale, renewable, carbon-free and safety alternative energy source is required. Nuclear fusion is one of the alternatives of future energy sources and particularly promising. Fuels of nuclear fusion such as deuterium and tritium are almost limitless, which can be obtained from seawater. Furthermore, nuclear fusion can produce large amount of energy from little fuels, e.g., the energy generated from 1g of deuterium and tritium is equivalent to that from 8 tons of oil. Nuclear fusion is also clean and safety. Fusion power plant can produce carbon-free energy and has no risk of a nuclear catastrophe, which is a weak point of nuclear fission plant.

To realize the nuclear fusion energy generation, confinement of plasma, which is ensemble of charged particles, is necessary. The condition of the fusion reactor to reach ignition is that the triple product of density, temperature and confinement time should be above a certain value (density $\sim 10^{20}$ [m^{-3}], temperature $\sim$ 1 billion degree, confinement time $\sim$ 1 [s]), which is known as Lawson criterion [1].

There are two methods of confining plasmas [2]; one is inertial confinement, in which high power leasers are used to compress the fuel strongly to cause fusion reactions. Another is magnetic confinement; plasmas are subjected to the Lorentz force to gyrate around the magnetic field line. Since plasma can move freely along the magnetic field, the magnetic field is designed to torus-shaped form. Then torus-shaped plasma confinement device have been developed and is widely studied to realize nuclear fusion plant. One of the advantage of the magnetically confinement fusion, compared to the inertial fusion, is continuous energy output.

The magnetic field confinement has been studied more than 70 years. To investigate burning plasma continuously, International Thermonuclear Experimental Reactor (ITER) [3] is now under construction. A schematic view of ITER is shown in Fig. 1.1. ITER is based on the tokamak concept as to demonstrate that the power amplification factor $Q = P_{\mathrm{fusion}}/P_{\mathrm{heat}}$ close to 10, where P_{fusion} and P_{heat} are power obtained by fusion and that injected externally for plasma heating, respectively. However, to keep the fusion ignition is difficult, since turbulence disturb plasma confinement. In hot and high density plasma, inhomogeneities of such pressure drive various instabilities, which finally develop into the turbulence. As is mentioned in the next section, turbulent transport causes degradation of plasma performance. Thus, a lot of researches have been focused on the turbulence and turbulent transport.

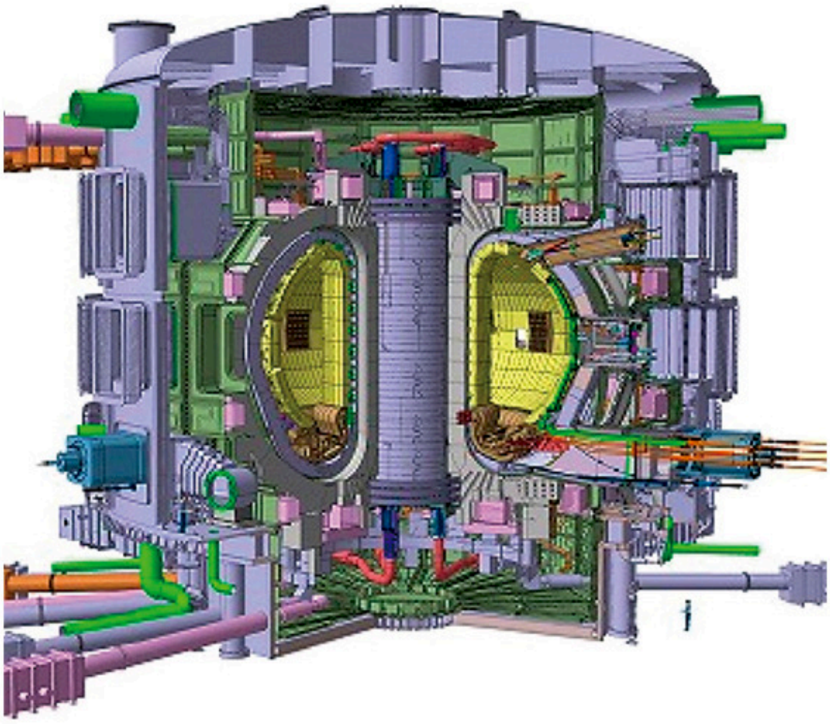

FIG. 1.1: Schematic view of ITER. The figure is cited from http : //www.mext.go.jp/a_menu/shinkou/iter/021/005.html.

1.2 Turbulent transport

The degradation of energy confinement is due to the cross field transport, i.e., loss of particles and heat across the magnetic field. The energy confinement time, τ_E, is roughly described as, $\tau_E \propto a^2/\chi$, where a and χ denote the radius of the plasma and heat diffusion coefficient. In general, the heat diffusivity is predicted as random walk process based on collisions (called as neo-classical theory), written as,

$$\chi \sim \lambda^2/\tau_c, \tag{1.1}$$

where λ and τ_c denote the step size and the collision time, respectively [2]. For the collisional process, the step size is almost determined as Larmor radius of ions or electrons. In typical tokamak plasma (T ~ 1 keV, $n_e \sim 10^{19}$ m^{-3} and B ~ 1 T), the coefficient is roughly estimated as $\sim 10^{-2}$ m^2/s.

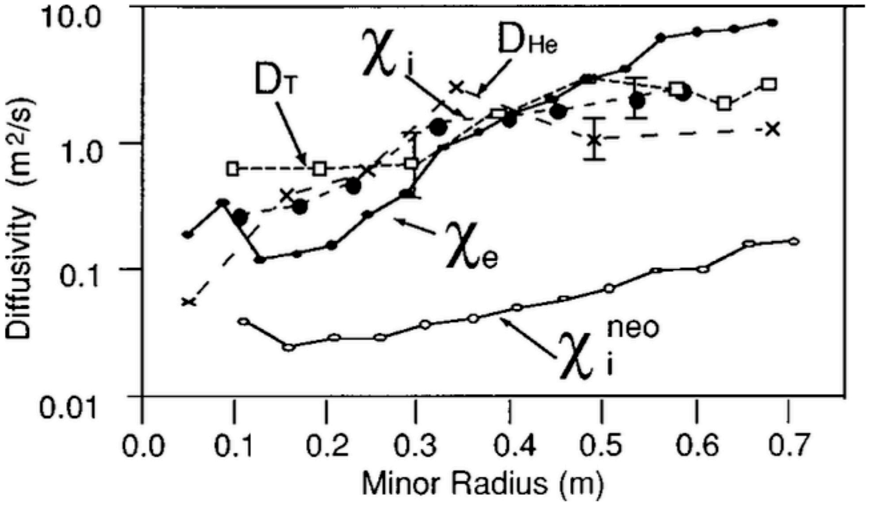

FIG. 1.2: The diffusivity coefficients of neo-classical transport and actual transport in TFTR [4].

However, experimental results dose not agree with that collisional transport, as shown in Fig. 1.2. The experimentally estimated transport coefficient is much larger than prediction based on the collisional process. At that time, that unexpected large transport process was called anomalous transport. Nowadays, it is revealed that the anomalous transport is mainly caused by the turbulence. Turbulent transport coefficient based on the quasi-linear theory is expressed as,

$$\chi \sim L_{\mathrm{turb.}}^2/\tau_{\mathrm{turb.}}, \tag{1.2}$$

where $L_{\mathrm{turb.}}$ and $\tau_{\mathrm{turb.}}$ represent the turbulence correlation length and correlation time, respectively [5]. For drift wave case, the correlation length is Larmor radius, and the correlation time is the inverse of drift frequency, respectively. Thus, transport coefficient is written as,

$$\chi \sim \frac{\rho}{L_n}\frac{T}{eB}, \tag{1.3}$$

where ρ and L_n are Larmor radius and density gradient length, respectively. Then, the transport coefficient in typical tokamak plasma is roughly 1 m^2/s. Therefore, the coefficient described in Eq. (1.3) is much larger than that in Eq. (1.1). Thus, it is obvious that the plasma confinement is mainly governed by turbulent transport.

The Eq. (1.3) is called as Gyro-Bohm scaling. In simple drift waves case, the Gyro-Bohm scaling is quite consistent [6, 7]. However, in strong turbulent states, nonlinear process deforms turbulent correlation length as $\sim \sqrt{\rho L_n}$. In this case, transport coefficient becomes,

$$\chi \sim \frac{T}{eB}, \tag{1.4}$$

which is called as Bohm scaling. Compare to the Gyro-Bohm, such a Bohm scaling induces large transport. Indeed, transports described as Bohm scaling are widely observed, and often accompanies a ballistic transport, which ejects heat and partilces instantaneously from core to edge [8–11]. Therefore, understanding of such transport mechanism and its turbulence process is important.

One of the reason of long correlated structure is due to the nonlinear process of turbulence. In plasma, micro-scale turbulence produce a number of convective cells [12], which have meso-scale structure. The convective cell is generated via Reynolds force of turbulnce, which is similar to the inverse cascade in quasi two-dimensional neutral fluid [13, 14]. One of the most famous examples of convective cells is zonal flow [15, 16]. Zonal flow is azimuthally elongated and radially localized convective cell [17–20]. Due to the such sturcture, zonal flow decorrelates turbulence radially via shearing effect [21–24]. Thus, turbulence transport is reduced [25–27]. Zonal flows are also known as a key for the transition from the low confinement mode to high confinement mode (L-H transition) [28–31].

Turbulence also can generate radially elongated and azimuthally localized structure, which is called streamer [32–35]. Similar to the zonal flow, turbulence can forms streamer via Reynolds stress [36, 37]. Streamer is expected to enhance the transport due to its elongated correlation length. However, compare to the zonal flows, the experimental observation of the streamer is few and partial. In practical, the controlling of streamer is important for plasma confinement, e.g., the streamer suppression contributes confinement improvement, while the streamer enhancement contributes releasing extra stored energy and impurities before disruption. Thus, basic understanding of streamer is required.

1.3 Streamer formation

FIG. 1.3: The contour plot of potential vorticities. The horizontal axis shows radial direction [33].

The study of streamer has progressed in simulation and theory. The various simulation results show that the turbulence, such as collisional drift waves [38], ITG (Ion Temperature Gradient mode) [32], ETG (Electron Temperature Gradient mode) [33, 34, 39] and ballooning mode [40], can nonlinearly excite large scale secondary vortex, which enhances radial transport. The famous example is observed in the ETG turbulence, as is shown in Fig. 1.3 [33]. The gyrokinetic simulation is performed for the ETG turbulence in toroidal geometry, and it is revealed that the electron heat flux was increased from ordinal ETG inducing heat flux. In the increased heat flux case, the radially elongated convective cells are formed. The convective $E \times B$ drifts can transfer plasma energy and particles from core region to edge. The resultant diffusion coefficient is thus above the gyro-bohm diffusion.

From theoretical approach, streamer is also described as nonlinear wave. It is known that the streamer is a formed from the Hasegawa-Mima equation [35–37, 41]. The equation is finally expressed as nonlinear Schrodinger equation [35, 41], which has a soliton solution. Following Ref. [41], there are two solutions, fast mode and slow mode. The structure of the fast and slow mode are described in Fig. 1.4 (a) and (b), respectively [41]. For the fast mode, amplitude of convective cells are localized in x direction, and elongate in y direction (x and y axes indicate azimuthal and radial directions). Thus, the fast mode can become a streamer. On the other hand, the slow mode has a node in y direction. This mode is called a mediator, which is nonlinearly interacted with turbulence to excite the streamer.

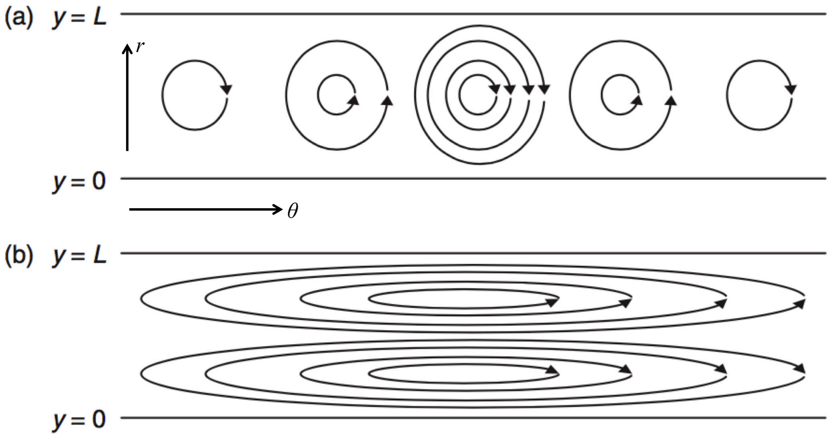

FIG. 1.4: Stream lines of (a) fast mode and (b) slow mode, obtained from the solution of the nonlinear Schrodinger equation [41].

In this way, the study of streamer has been performed through simulation and theory. However, as mentioned before, experimental observations in hot confined plasmas are very few. Since the streamer has radially elongated and azimuthally localized structure, simulatneous fluctuation measurements from core to edge and low-field side to high-field side are necessary. This is quite difficult in high temperature torus plasmas. There are only few experimental observations that the fluctuations have long radial correlations [42], but it is not clear about the streamer excitation and their impact on transport.

On the other hand, in cylindrical plasmas, since plasma temperature is relatively low, direct fluctuation measurements from core to edge are possible. Therefore, cylindrical plasmas help us to understand basic physics of the nonlinear process, structure and transport driven by streamer. The cylindrical device, LMD-U (Large Mirror Device Upgrade), which was in Kyushu University, is a linear magnetized plasma with low temperature [43]. Besides, in LMD-U plasma, large density gradient can be formed, and can excite drift wave instability. These diagnostic advantages enable to observe streamer for the first time [44].

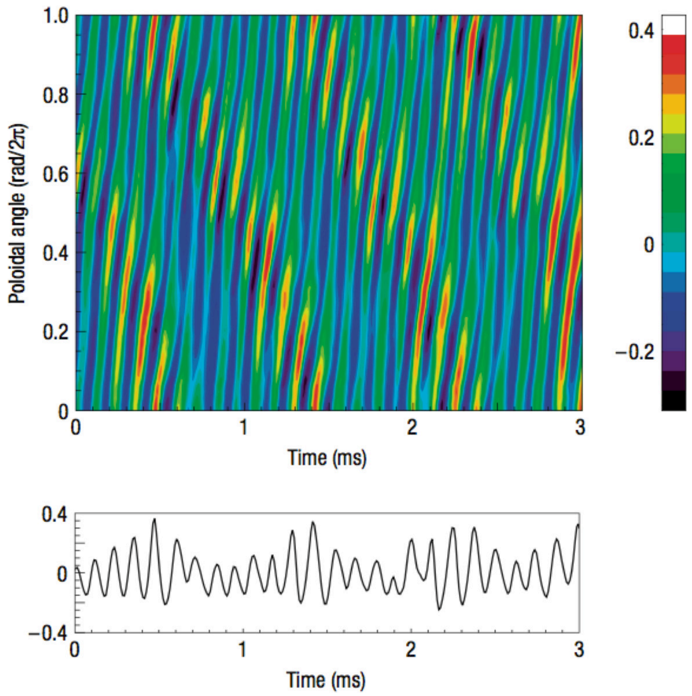

FIG. 1.5: The modulation of the fluctuation can be seen in time evolution of ion saturation current fluctuation. The vertical axis of the contour indicates the poloidal angle, where its direction is electron diamagnetic. Under the contour plot, ion saturation current fluctuation at poloidal angle $\theta = 0$ is shown [44].

As is shown in Fig. 1.5, streamer was observed as a modulation of the fluctuations. In the contour plot, thin line of drift wave components rotates in electron diamagnetic direction, while envelope of the Drift waves rotates in ion diamagnetic direction. This bunching structure, or amplitude modulation of fluctuations, is the streamer. The amplitude modulation is carried out through low frequency flute type mode, which is called as mediator. Nonlinear coupling between the drift waves and the mediator generates the radially elongated structures. Such structure is experimentally confirmed by bi-phase analysis, which clarifies the phase relationship among nonlinear couplings [45]. The observed components of mediator and streamer are predicted with slow and fast mode in ref. [41]. In addition, the fluid simulation code, which is called as NLD (Numerical Linear Device) code, is performed for the varidation [38]. The code is based on the reduced fluid model in the cylindrical geometry. In the nonlinear saturation phase, the drift waves form long radial wavelength and azimuthally localized structures. Figure 1.6 shows the result of NLD. Snapshots of the contour plot of the electrostatic potential are shown in the figure. The amplitude of radially elongated vortex is localized in azimuthal direction, and also extended in the axial direction. The vortex is sustained for much longer duration than the drift wave oscillation period. It is also confirmed that the vortex is come from the nonlinear couplings between drift waves and mediator.

The radial phase relation and nonlinear process of streamer formation have been studied in LMD-U, however, there are still some tasks. In the previous results, the real structure of streamer, which might be a nonlinear waves, are not yet observed. More important point is that it is not confirmed that whether streamer really enhances transport. The causality between radially elongated structure and enhanced transport is still not revealed. In addition, the streamer control is necessary for confinement plasmas. One of the candidates for streamer suppression is electric field shear. Therefore, the understanding the relation between streamer

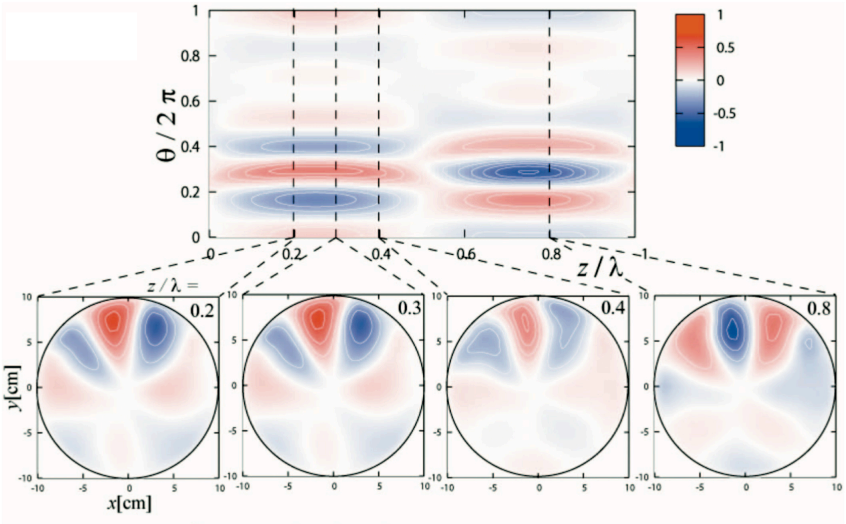

FIG. 1.6: Counter plot of the potential fluctuation in the r-θ and θ-z plane. The bunching of drift waves are localized in azimuthal and elongate in radial [38].

and electric field is required.

1.4 Purpose of this thesis

The purpose of this thesis is focused on the basic understand of streamer structure and its impact on transport. As is already mentioned, streamer is a key for large magnitude of turbulence transport, degradation of confinement and expelling extra energy and impurities, thus the understanding of their structure, inducing transport and the controlling are important. Up to know, the streamer is identified in linear plasma machine, PANTA, by observing the structure of the streamer are radially extended, azimuthal localized and formed by nonlinear couplings. Thus, important studies of streamer are remained that (i) how the spatio-temporal structure of the streamer determined and what is their associated transport and (ii) the controlling of streamer and its transport by inducing electric field.

To achieve the purpose, the data analysis and experimental methods are developed. The observation of streamer structure and its transport should be performed in quantitative and dynamical ways. Hence, the conditional averaging technique is developed, and the dynamics of streamer are reconstructed qualitatively. For investigating the electric field dependence on streamer, the external voltage source is necessary. Thus, an end-plate biasing experiment is performed to induce electric field perturbation to the streamer.

This thesis is organized as follows: in Chapter 2, linear machine PANTA and main measurement tools are explained. Basic idea of Langmuir probes, which are the main diagnostics in this thesis, are introduced. In Chapter 3, data analysis techniques are reviewed. In addition to the conventional spectral analysis, conditional averaging techniques are explained and discussed. Experimental results are shown from Chapter 4. In Chapter 4, the streamer structure, including its nonlinearity, and associated transport are mentioned. The spatio-temporal structure of streamer is revealed by the conditional averaging technique. In Chapter 5, the biasing experiment is conducted to observe the effect of the electric field on the streamer. The changes of nonlinear interaction and transport degradation are discussed. The conclusion of the thesis is in Chapter 6.

Chapter 2

Experimental device and diagnostics

In magnetically confined hot plasmas, instabilities can develop into the fully turbulent states, which are composed of wide range of frequency and wave number components. In such hot plasmas, because of restriction of access of diagnostic tools, the experimental investigation of turbulence is difficult. Even if accessibility of the diagnostics is possible, the interruption of obtained data is very complicated due to lots of factors, e.g., high energy particles and bent magnetic field effects. Therefore, for studying basic physics of nonlinear interaction of plasma instabilities, a relatively low temperature plasma and a simple magnetic field configuration is appropriate. The experimental device, PANTA (Plasma Assembly for Nonlinear Turbulence Analysis), successor device of LMD-U, is a linear magnetized plasma, and produces various type of instabilities through radial inhomogeneities. These instabilities nonlinearly interact with each other, and can generate mesoscale structures. In PANTA, because of the relatively low temperature, Langmuir probe measurement is possible with fine time and space resolutions. In addition to the probes, a tomography system is developed in PANTA to investigate fluctuations with various scales simultaneously. In this way, the experimental device PANTA and the methodology of these diagnostics tools are introduced in this chapter.

2.1 PANTA

PANTA is a cylindrical device and can produce a linear magnetized plasma. For studying the basic processes of turbulence [46–48], nonlinear interaction [49,50], turbulent transport [51,52], etc., such a small simple device has lots of advantages as shown in the following.

- Accessibility of diagnostics from core to edge
- Measurements with fine time and space resolutions
- Good reproducibility, easy to obtain large ensembles of data for statistical analysis
- Simple interpretations of data because of simple magnetic field geometry
- Easy to try new experiments and diagnostics

A lot of works, which are focusd on plasma turbulence, are carried out in various linear device, i.e., CSDX [53,54], LAPD [55,56], MIRABELLE [57], KIWI [58], VINETA [59], COLLOMBIA [60], MISTRAL [61], LMD-U [62,63], Q-Machine [64, 65] and HYPER-II [66]. Compare to these device, PANTA is constructed especially focused on turbulence studies.

The vacuum vessel configuration of PANTA is shown in Fig. 2.1. The cylindrical vacuum vessel has the diameter of 457 mm and the length of 4050 mm, and is composed of 16 modular chambers for frexiblility of diagnostics. Axial magnetic field is produced by 17 coils and can be set in the range up to ~0.15 T. Mainly, Argon gas is injected to produce plasmas at the source region and its filling pressure is controlled by mass-flow controller. The filling neutral pressure is kept constant around the 0.45 ~ 5 mTorr. The vessel is continuously pumped out with five turbo-molecular pumps, where their exhaust capability is around 1400 L/s. In addition, two baffle plates with inner diameter of 150 mm are installed to prevent the neutral gas from being released to main plasma region [67]. The plasma is produced by helicon wave (1.5k ~ 6 kW, 7 MHz) with a double loop antenna. The double-loop antenna is equipped on the surface of quartz tube with the inner diameter of 100 mm, and it is connected with the matching circuit box and RF power supply. A pair of capacitors in the matching box can be adjusted before experiment to minimize the ratio of reflection power to input power. The stainless flange, called end plate, is installed at the end of the device to terminate the plasma.

The characteristics of fluctuations depend on neutral gas pressure, magnetic field and RF input power [68]. The radial pressure gradient can change with modifiying these external parameters. In addition to the radial pressure inhomogenity, the velocity shear and axial pressure inhomogenity, which are candidate for free energy source of the fluctuations, are observed in PANTA [46]. These inhomogenities also can be controled by changing the external parameters. Note that the collisonal parameter, e.g. ion-neutral collison frequency, is also modified by changing the external parameter. The collisonal parameter is important for the growth and damping of the instabilities. In adition to the experiments, various simulation studies have been done in PANTA for varidation and prediction of fluctuations [69–71].

The streamer is observed in relatively low gas pressure, at around 0.06 ~ 0.13 Pa (or 0.45 ~ 1 mTorr) [68]. Typical central density and electron temperature are $0.5 \times 10^{19} \mathrm{m}^{-3}$ and 2 eV, respectively. The electron density gradient is steep in the region of r = 30 - 40 mm, where drift wave instabilities are excited [72]. The linearly excited drift waves form self-focused (bunching) structure through

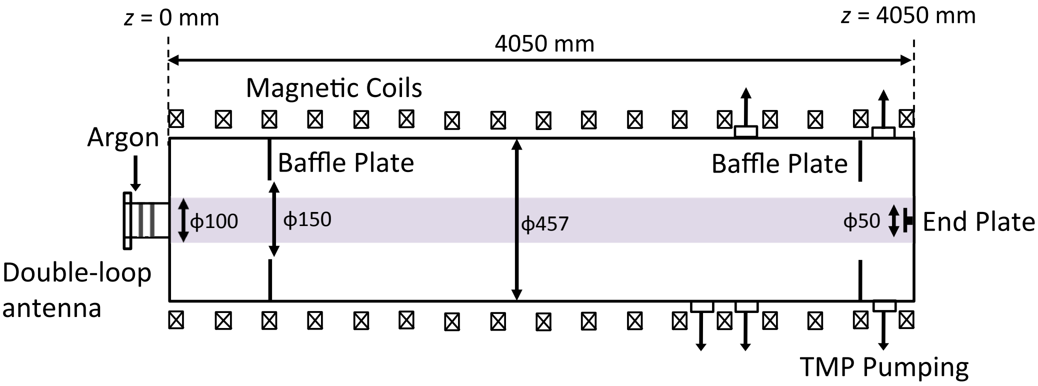

FIG. 2.1: Configuration of linear cylindrical plasma device, PANTA.

Parameters	Streamer condition	Available range
Background Pressure	1.0×10^{-4} Pa	$1 \times 10^{-4} - 5 \times 10^{-3}$ Pa
Filling Gas Pressure	6.0×10^{-2} Pa	6.0×10^{-2} - 6.7×10^{-1} Pa
Magnetic Field	0.09 T	up to 0.15 T
RF Power for Helicon	3 kW	1.5 – 6 kW
Peak Electron Density	5×10^{18} m^{-3}	$10^{18} - 10^{19}$ m^{-3}
Electron Temperature	2 eV	1 – 6 eV
Ion Temperature	0.1 eV	0.1 – 0.3 eV

Table 2.1: Typical values of plasma parameters in the streamer condition and available ranges for various experiments.

amplitude modulations by the mediator. Operation conditions and typical plasma parameters in the streamer condition are summarized in Tab. 2.1.

In PANTA, data acquisition is performed through Analogue-to-Digital converters (ADC) called ”WE7000”, which was manufactured by YOKOGAWA. The 192 channels are used for obtaining basic parameters and probe diagnostics. The sampling rate of the ADC at the experiment is 1 MHz. Figure 2.2 shows the data acquisition and network in the experimental room. Every channel data is stored in a data server through FTP transmission. It is noted that the data acquisition of tomography system is different. The details are shown in the later section.

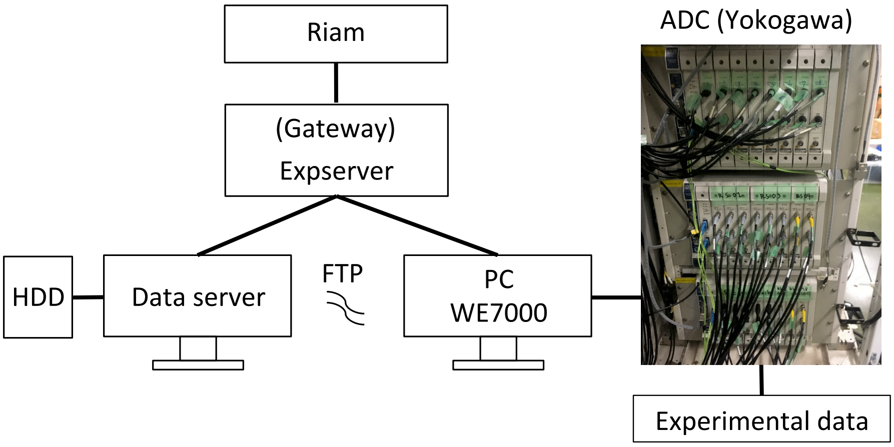

FIG. 2.2: The data acquisition and network system in PANTA.

2.2 Diagnostics

To measure plasma fluctuations, Langmuir probe is a suitable tool for its accessibility and wide variety of measurable parameters. The advantages of probes are simple design mechanism and feasibility with fine spatio-temporal resolution measurements, while the disadvantages are that the probes disturb plasma and could not access to the hot plasma. Therefore, measurement tools, which are not disturbing plasma, are also developed in PANTA. The tomography system is now developed and could detect wide spatio-temporal range of fluctuation simultaneously. In the following section, the methodology of probes and tomography system in PANTA are introduced.

2.2.1 Basics of Langmuir probe

Langmuir probe was invented by Langmuir and Mott-Smith in 1926, as a plasma measurement facilitate tools [73]. The probe tip is composed by tungsten or molybdenum to withstand high heat flux. Langmuir probe can measure following quantities; plasma density, electron temperature, floating and plasma potential and their fluctuations. The probe measurement is simple, however, the interruption of the data is not straightforward. The basic idea of the probe measurement is mentioned here.

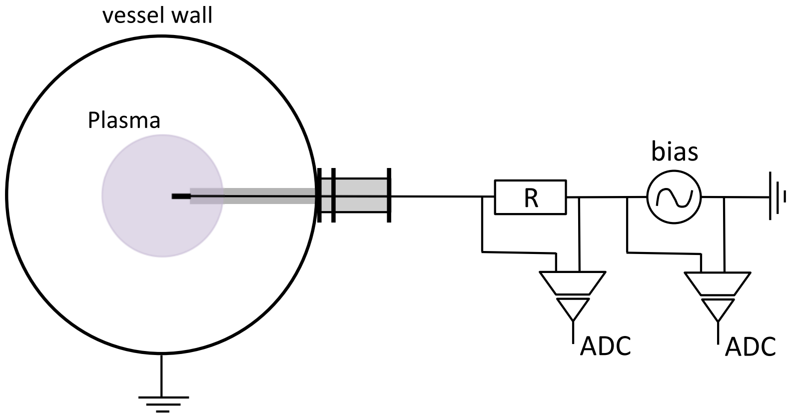

FIG. 2.3: Typical circuit for single probe measurement. The bias voltage amplitude is 50 V, and the sweeping frequency of the triangle wave is 100 Hz. A shunt resistance is set to R = 20 Ω.

• Single probe measurement

The single probe measurement is the most basic and essence of the probe measurement [74]. The typical circuit for the single probe is shown in Fig. 2.3. The probe tip is biased sweepingly by probe voltage V_p, and the probe current I_p is measured by a shunt resistor. In PANTA, the triangle waveform with amplitude of 50 V and frequency of 100 Hz is applied to the probe tip. The obtained I_p-V_p curve contains an information of density, electron temperature and plasma potential of bulk plasma.

Figure 2.4 shows the typical I_p-V_p curve. When the bias voltage equals to the plasma potential V_s, the plasma is not affected by the biasing. In this case, thermal motion of ion and electron flow into the probe as,

$$I_j = \frac{1}{4} A q_j n_j \bar{v}_j \equiv I_{j0}, \quad j = i, e, \tag{2.1}$$

where A is the collective area of probe tip, q_j, n_j and $\bar{v}_j$ indicate charge, density and mean thermal speed of ion and electron. Here, the mean thermal speed is defined as,

$$\bar{v}_j = \sqrt{\frac{8T_j}{\pi m_j}}, \quad j = i, e, \tag{2.2}$$

where T_j and m_j are temperature and mass of ion and electron. Therefore, in the $V_p = V_s$ case, the probe current is represented as,

$$I_p = I_{e0} + I_{i0}. \tag{2.3}$$

Since the electron mean thermal speed is much larger than ions, the probe current is mostly dominated by the electron current.

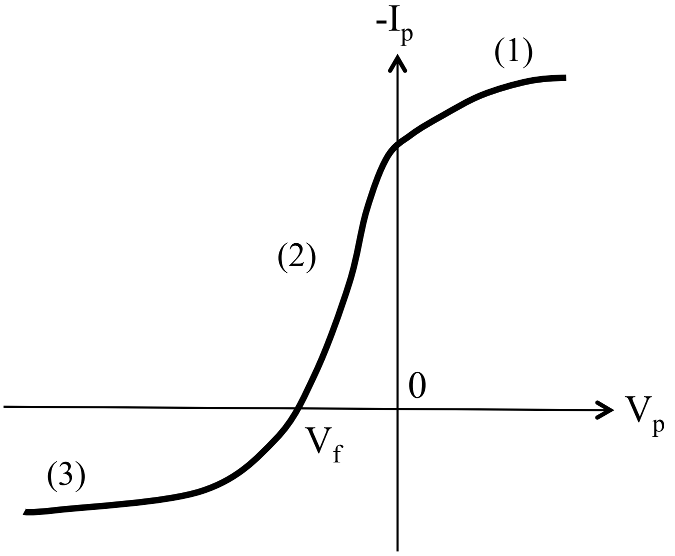

FIG. 2.4: Schismatic of typical $I_p - V_p$ curve.

According to the bias voltage, the characteristic of probe current changes and can be categorized in three domains; (1) electron saturation region (electron sheath region), (2) electron deceleration region and (3) ion saturation region (ion sheath region).

(1) Electron saturation region

When the bias voltage is beyond the plasma potential, i.e., $V_p > V_s$, ions are repelled and electrons are accelerated to the probe tip. The probe tip is surrounded by the electrons, which is called electron sheath. In this case, the probe current is dominated by the electron current as,

$$I_p \cong I_{e0}. \tag{2.4}$$

(2) Electron deceleration region

When the bias voltage is less than the plasma potential, i.e., $V_p < V_s$, ions are accelerated and electrons are repelled from the probe tip. Then the probe tip is start to surrounded by the ions, which is called ion sheath. However, since the electron thermal speed is large, the probe current is still dominated by the electron current. The decrease of the electron density can be followed with Boltzmann relation as,

$$n_e = n_{e0} \exp\left(-\frac{e(V_p - V_s)}{T_e}\right). \tag{2.5}$$

Therefore, electron current is written as,

$$I_e = I_{e0} \exp\left(-\frac{e(V_p - V_s)}{T_e}\right). \tag{2.6}$$

For ions, at the sheath edge, the Bohm's ion sheath criterion indicates that the ions are accelerated to the sound speed by the sheath potential drop $V_{sheath} = T_e/2e$ (relative to the plasma potential) as,

$$v_i = \sqrt{\frac{2eV_{sheath}}{m_i}} = \sqrt{\frac{T_e}{m_i}} \equiv c_s. \tag{2.7}$$

At the sheath edge, where the quasi-neutrality is preserved, ions flow into the probe tips with the density given as,

$$n_i = n_e = n_{e0} \exp\left(\frac{eV_{sheath}}{T_e}\right) = n_{e0} \exp\left(-\frac{1}{2}\right). \tag{2.8}$$

Thus, the ion current is represented as,

$$I_i = I_{i0} + Aq_i n_i c_s = I_{i0} + Aq_i n_{e0} c_s \exp\left(-\frac{1}{2}\right). \tag{2.9}$$

Since the ion thermal motion is sufficiently small, the heat diffusion current I_{i0} is negligible. Finally the probe current is obtained as,

$$I_p = Aq_i n_{e0} c_s \exp\left(-\frac{1}{2}\right) - I_{e0} \exp\left(-\frac{e(V_p - V_s)}{T_e}\right). \tag{2.10}$$

This formula provides to measure the electron temperature by subtracting the ion current components and then calculate the slope of the semi-logarithmic plot. In addition, when I_p becomes 0, the ion and electron current is equivalent. Such a bias voltage is called floating potential V_f.

(3) Ion saturation current region When the bias voltage is much smaller than the plasma potential, electrons are almost repelled from the probe tip and complete ion sheath is created. The probe current is dominated in the ion current as,

$$I_p = Aq_i n_{e0} c_s \exp\left(-\frac{1}{2}\right). \tag{2.11}$$

This is called ion saturation current. The electron density n_{e0} is easily calculated by substituting T_e.

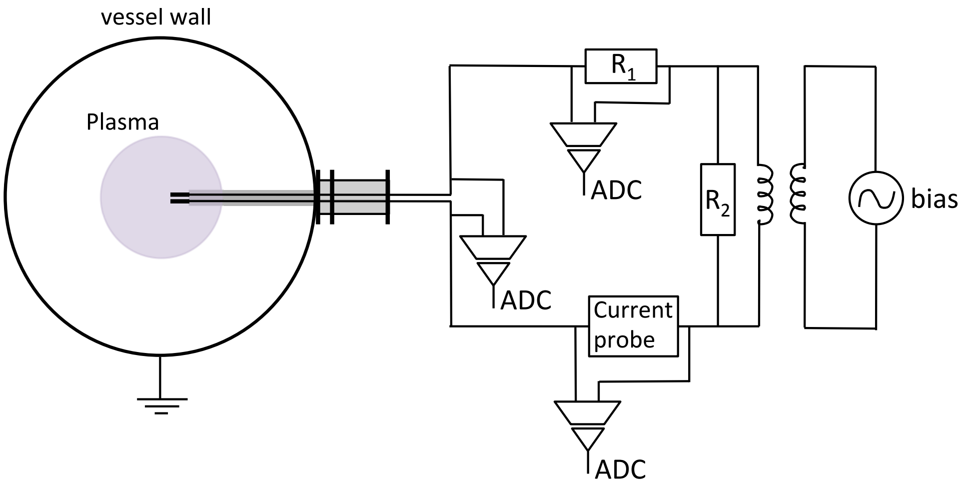

FIG. 2.5: Typical circuit for double probe measurement. The bias amplitude is 50 V, and the sweeping frequency of the triangle wave is 100 Hz. The bias current is monitored by the Shunt resistance of R_1 = 51.1 Ω and current probe. Bias voltage is traced directly from probe tips. Parallel resistance is R_2 = 500 Ω.

• Double probe measurement

Single probe measurement is attained through biasing the probe tips against reference potential ground, which is often set by the vessel ground. When the plasma potential changes temporally from the vessel ground (e.g. in the situation of biasing experiment), the appropriate I_p-V_p curve do not be obtained.

Double probe measurement is performed by using two probe tips with floated circuit relative to the vessel ground, as shown in Fig. 2.5. Since the circuit is floated, the appropriate probe current is obtained even if the plasma potential changes temporally. The typical I_p-V_p curve is shown in Fig. 2.6. Here, the bias current is restricted to the ion saturation current. The electron temperature is deduced from the I_p-V_p current as,

$$\frac{T_e}{e} = -\frac{\Sigma I_i}{A_1\left(\frac{dI_p}{dV_p}\right)_{V_p=0} - A_2\left(\frac{dI_p}{dV_p}\right)_{V_p=sat.}}, \qquad (2.12)$$

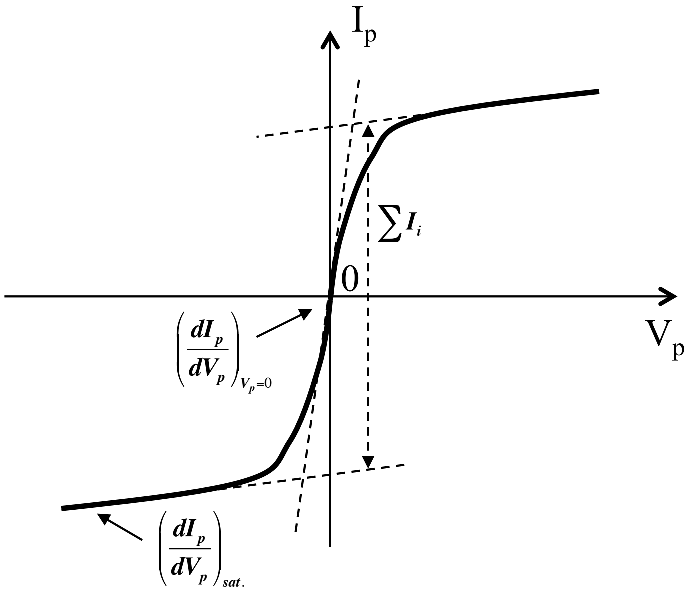

FIG. 2.6: Schematic of typical I_p-V_p curve for double probe measurement.

where ΣI_i indicates summation of ion saturation current for each probe tip (see Fig. 2.6), and coefficients $A_1 = 4$ and $A_2 = 3.28$ for laboratory plasmas. In practical way, the slopes and ΣI_i are obtained from I_p-V_p curve by fitting linear (for $\left(\frac{dI_p}{dV_p}\right)_{V_p=sat.}$) and tangent hyperbolic function (for $\left(\frac{dI_p}{dV_p}\right)_{V_p=0}$ and ΣI_i) simultaneously.

• Fluctuation measurement : Ion saturation current

When the bias voltage is sufficiently negative to the plasma, ion saturation current flowing into the probe tips. The fluctuation of ion saturation current is measured with a constant biasing. The bias voltage of V_p = -90 V is applied for the ”black” circuit box (used for 64ch probe and 5ch probe, which will mention in the section 2.2.2), and V_p = -60 V is applied for the ”silver” circuit box (used for RS probe, which is also introduced in the section 2.2.2). The circuit is indicated in Fig. 2.7. The fluctuation components of ion saturation current, which is described in Eq. (2.11), could be represented when the electron temperature fluctuation is

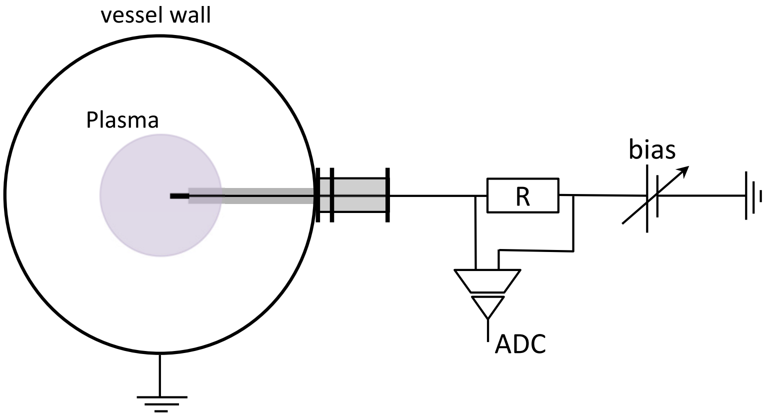

FIG. 2.7: Schematic of typical circuit for fluctuation measurement of ion saturation current. Shunt resistance of R = 20 Ω is provided.

negligibly small,

$$\tilde{I}_{is} \propto \tilde{n}_e, \tag{2.13}$$

where fluctuation components of signal x is defined as $\tilde{x} = x - \bar{x}$ ($\bar{x}$ indicates long time average of signal x). The validity of the assumption that the electron temperature fluctuation can be neglected is confirmed that the temperature fluctuations are small compared with the density fluctuations as $\frac{\tilde{T}_e}{\langle T_e \rangle} / \frac{\tilde{n}_e}{\langle n_e \rangle} \leq \frac{1}{12}$ [75].

- **Fluctuation measurement : Floating potential**

The floating potential is obtained by connecting a high impedance resistor so that the probe current becomes negligible relative to the ion saturation current. Figure 2.8 shows schematic view of floating potential measurement circuit. The pickup resistor R_2 is set to 50 kΩ for black box and 50 Ω for silver box. Floating potential is obtained by substituting $I_p = 0$ into Eq. 2.10, and is given as,

$$V_f = V_p + \alpha \frac{T_e}{e}, \tag{2.14}$$

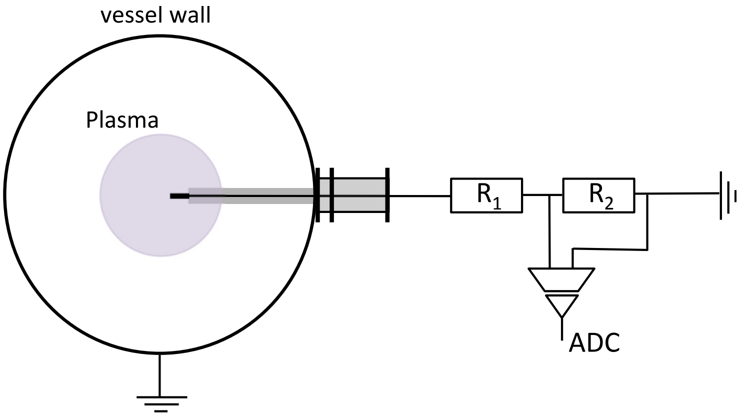

FIG. 2.8: Schematic of typical circuit for fluctuation measurement of floating potential. The resistance for voltage divider is set as R_1 = 1 MΩ and R_2 = 50 kΩ (for black circuit box) or R_2 = 50 Ω (for silver circuit box).

where α is given as,

$$\alpha = \ln\left[\exp\left(-\frac{1}{2}\right)\sqrt{2\pi\frac{m_e}{m_i}}\right]. \tag{2.15}$$

For Argon plasmas, α is approximately -4.8. Here, the same assumption, that the electron temperature fluctuation is small compared to the plasma potential fluctuation, is applied and thus,

$$\tilde{V}_f \simeq \tilde{V}_p. \tag{2.16}$$

2.2.2 Probe arrays

The combination of Langmuir probe can provide to measure a lot of quantities, i.e., wave number, electric field fluctuations, fluctuation induced particle flux and Reynolds stress. In this thesis, following three probe arrays are used.

- **64ch probe**

An azimuthal aligned Langmuir probe is one of the methods to investigate the azimuthal wave number and the frequency of fluctuations simultaneously and ap-

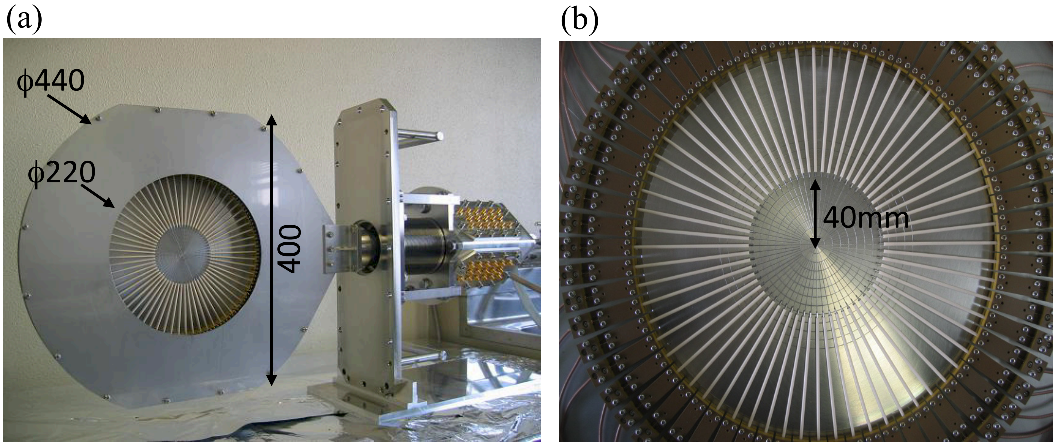

FIG. 2.9: (a) Picture of the 64ch probe array. (b) Extended view.

plied in many devices, such as KIWI [76], VINETA [57] and TJ-K [78]. A view of the 64-channel azimuthal probe array (64ch probe) is shown in Fig. 2.9 (a). Each probe consists of a tungsten tip with the diameter of 0.8 mm and the length of 3 mm. The 64ch probe is locatted at z = 1885 mm, almost middle of the PANTA. The alternatingly arranged 32 probes of the array measure ion saturation current, and the other neighboring 32 probes measure floating potential. The radial position of probe tips are 40 mm, as shown in Fig. 2.9 (b). The accurate alignment of the probe tip is demonstrated for reducing errors of azimuthal mode number [79]. After install to the PANTA, the center of the array can be adjusted to be the center of the plasma within a precision much less than few mm. The detail of alignment is referred in [79]. The 64ch probe is connected to the black circuit box. For floating potential measurement, the stray capacitance of co-axial cable could distort the high frequency power and phase. The black box includes a compensating capacitance, which is possible to measure the fluctuation with the frequency less than 20 kHz.

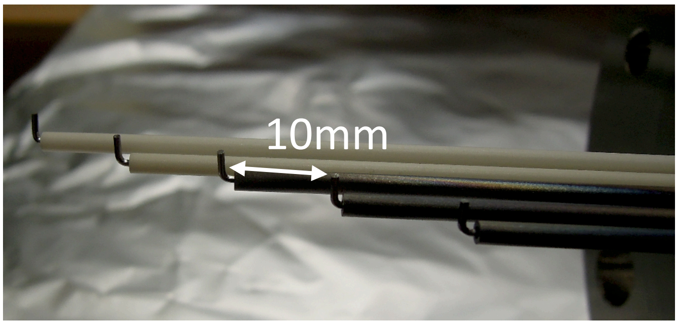

FIG. 2.10: Picture of 5ch radial probe. Distance between neighbouring two probe tips is 10 mm.

- **5ch probe**

Another basic tool in PANTA is 5-channel radial probe array (5ch probe) as shown in Fig. 2.10. The radial interval of the probe tips is 10 mm. It measures a ion saturation current or floating potential. In the experiment, 5ch probe is mostly located at z = 1375 mm (in front of the 64ch probe array). The radial position of 5ch probe is calibrated by using the position of most strong correlation between 5ch probe and 64ch probe.

- **RS probe**

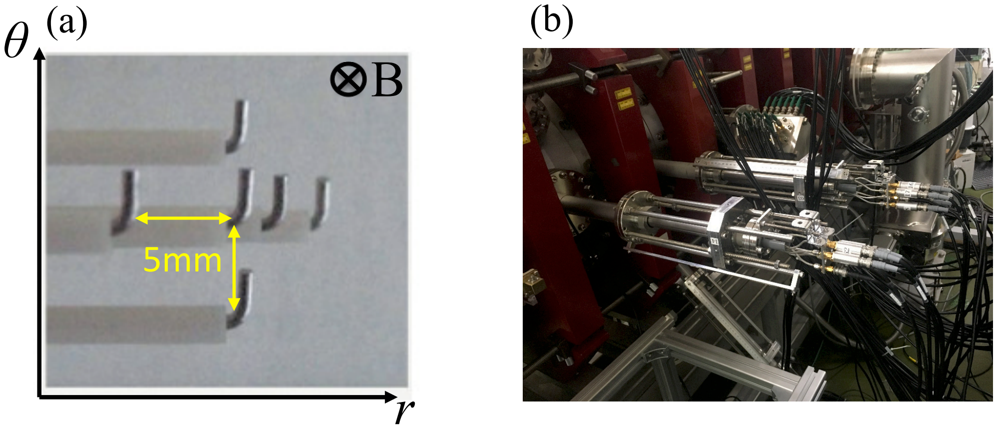

FIG. 2.11: (a)RS probe tips. (b)The resistance of 1 MΩ is prepared just before the long co-axial cable.

Reynolds stress probe (RS probe) is composed of 6 tungsten tips, as shown in Fig. 2.11 (a). Each probe tips have a distance of 5 mm from the center probe tip, except the one of tip [80, 81]. In the experiment, the center probe measures ion saturation current, and the other probe measure floating potential. The combination of potential fluctuation measurement allows to deduce radial and azimuthal electric field fluctuations. Then, Reynolds stress or particle flux is derived from the RS probe.

For the floating potential measurement, the circuit of RS probe is different from 64ch probe and 5ch probe. As shown in Fig. 2.11 (b), the large resistance of 1 MΩ is installed just after the probe system, before the long co-axial cable. This system reduces the effect of stray capacitance of the co-axial cable. Then, the co-axial cable installed to the "silver" circuit box, which has 50 Ω pick-up resistor and the signal is transmitted to the ADC through 40 dB amplifiers.

2.2.3 Tomography

For measuring multi-scale fluctuations structure, tomography system is now on developed in PANTA [82]. The emissions from Argon lines are measured through collimator at the detector, as shown in Fig. 2.12. The 4 detectors are set in the module, and each detector has 33 channels of sight. Thus, totally 132 channels are prepared to measure the integrated line of sight simultaneously. The optical filter is installed to detect the ArI (810 ± 30 nm) or ArII (476.5 ± 30 nm). In PANTA, the observation revealed that the emission intensity of ArI is stronger than that of ArII. Finally, the photons are converted to the electric signals by photo-diode and digitized by the ADC, which has the sampling rate of 1 MHz.

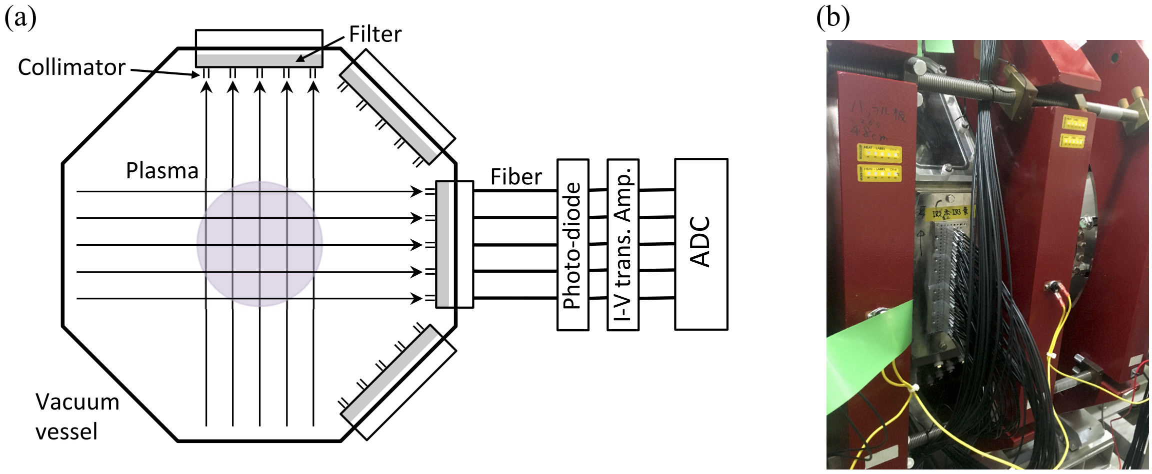

FIG. 2.12: (a) Schematic of tomography system in PANTA. (b) Picture of detectors and fibers.

• Maximum Likelihood-Expectation Maximization method

Tomography is a method to reconstruct the local emission profile from a set of line integrated emission signals. There are a number of algorithms for the reconstruction, however, maximum likelihood-expectation maximization (MLEM) method is preferable for the turbulence measurement [83]. MLEM has two advantages; (1) assumption of any basis function is not required and (2) returning only positive values. MLEM has been developed in medical application fields, as known for iterative algorithm. The goal of the reconstruction is that the estimation of the local emissions from the j-th grid, ϵ_j, as shown in the Fig. 2.13. The integrated emission y_i is measured in the i-th detector and can be written as $y_i = \Sigma_j C_{ij}\epsilon_j$, where C_{ij} indicates the contribution coefficient to the i-th line of sight from the j-th grid. Assume that the detection of photons obey Poisson distribution, the probability of the number of photons from the j-th grid x_{ij} is calculated as,

$$P(x_{ij}) = e^{-C_{ij}\epsilon_j} \frac{C_{ij}^{x_{ij}} \epsilon_j^{x_{ij}}}{x_{ij}!}. \tag{2.17}$$

Then, maximum likelihood method is applied to the probability density function of the x_{ij} for every j-th grid and i-th detector as,

$$\frac{\partial}{\partial \epsilon_j} \ln \left(\Pi_\mathrm{i} \Pi_\mathrm{j} P(x_{ij}) \right) = 0. \tag{2.18}$$

When the emission after the k-th iteration calculation is assumed as ϵ_j^k, the number of photons from the j-th grid x_{ij} is expected as,

$$E(x_{ij}) = y_i \frac{C_{ij} \epsilon_j^k}{\Sigma_m C_{im} \epsilon_m^k}. \tag{2.19}$$

Finally, the $(k{+}1)$th iterated local emission, ϵ_j^{k+1} is calculated by Eq. (2.18) and Eq. (2.19) as,

$$\epsilon_j^{k+1} = \frac{\Sigma_i E(x_{ij})}{\Sigma_i C_{ij}}. \tag{2.20}$$

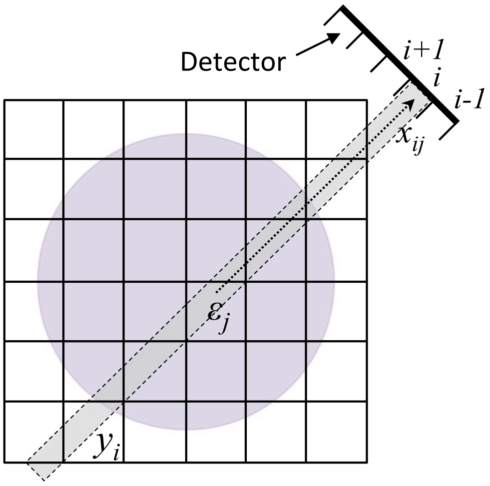

FIG. 2.13: Configuration of MLEM method.

The iteration is performed until the convergence of the emission is obtained as,

$$\left| \epsilon_j^{k+1} - \epsilon_j^k \right| < \delta, \tag{2.21}$$

where δ is chosen as $10^{-5}\times$ (maximum value of ϵ_j^k). For the practical calculation, the initial emission distribution ϵ_j^0 is selected to 1 for every j-th grid.

• Fourier-Bessel expansion

For studying the fluctuations structure effectively, the reconstructed local emission distribution could be fitted to Fourier-Bessel function [84]. The decomposition to Fourier-Bessel function is given as,

$$\epsilon\left(r,\theta\right) = \Sigma_{mn}\left[a_{mn}J_m\left(k_n r\right)\cos\left(m\theta\right) + b_{mn}J_m\left(k_n r\right)\sin\left(m\theta\right)\right], \tag{2.22}$$

where $J_m(k_n r)$ indicates normalized m-th order Bessel function. For the boundary condition, the $J_m(k_n L_{max}) = 0$ should be satisfied, where the L_{max} is the radius of the boundary.

Figure 2.14 shows examples of the tomography, ArI emission. The reconstructed emission distribution at a certain time is obtained from the MLEM method. The emission distribution is not azimuthally symmetric. It is suggested that the fluctuations with several azimuthal mode number components are coexistent. The Fourier-Bessel expansion is applied to the emission data, and the fluctuation components of $m = 0$, 1 and 2 are extracted. The counter plots in Fig. 2.14 apparently show that the fluctuations with different mode number and spatial scales coexist in the plasma.

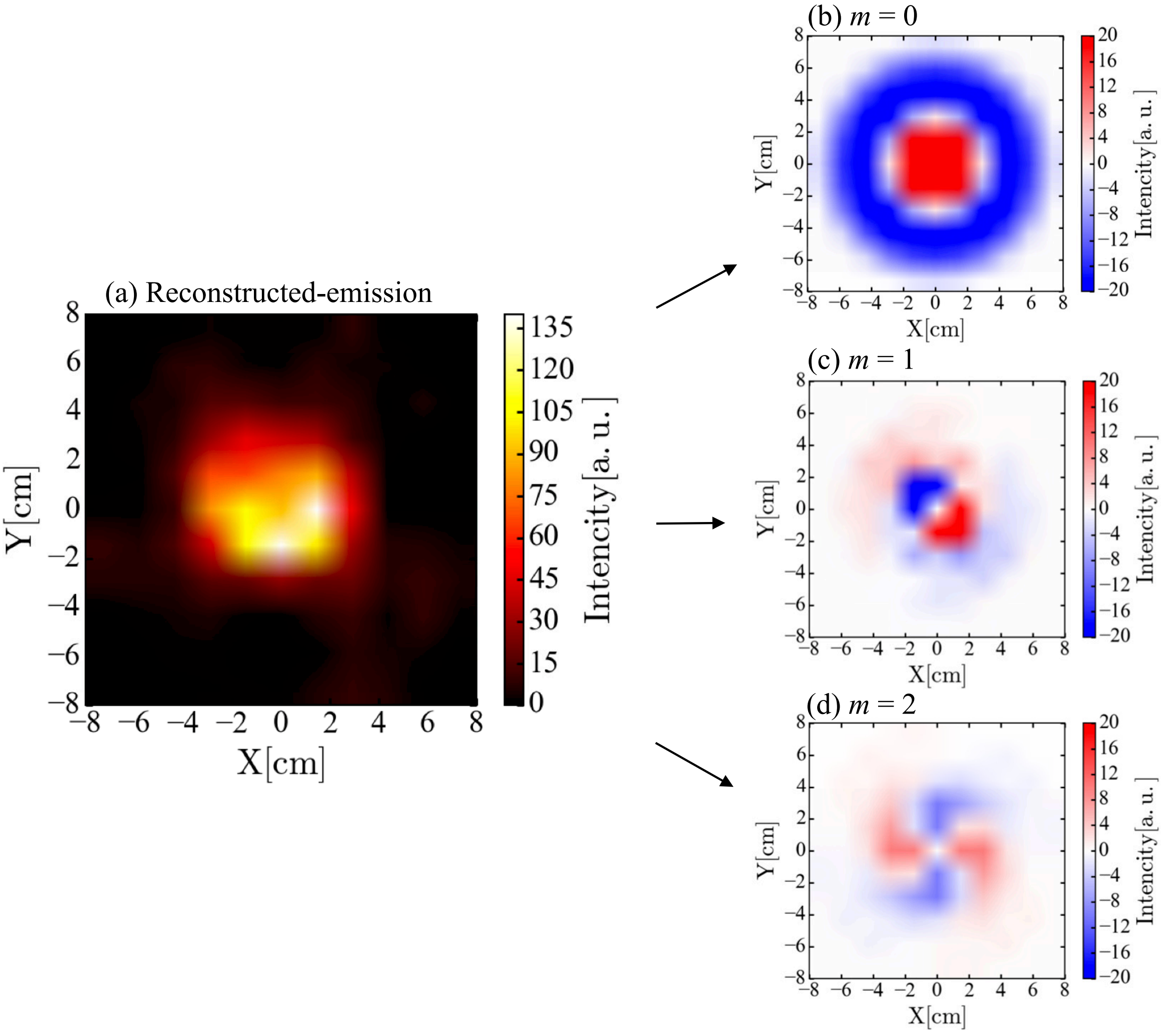

FIG. 2.14: Example of the tomography signal at a certain time. (a) Emission distribution deduced form MLEM. (b)-(d) Fourier-Bessel expansion of fluctuation components of m = 0, 1 and 2, respectively.

Chapter 3

Methods of data analysis

In magnetized plasmas, turbulence behaviours are complex in time and space. Undoubtedly, investigation of raw signals is crucial, however, the raw signals normally contain noises. Thus, statistical analysis is a strong tool to extract important information from the signal quantitatively. Since the analyzed results change depending on the process of data analysis, verification study is important. In this chapter, the methods of data analysis with the check of validity of their process are mentioned.

3.1 Spectral analysis

Idea of spectral analysis is based on the concept that the raw temporal signals are composed of superposition of fundamental waves. The decomposition of the signals are performed by two practical ways, Fourier and wavelet transforms. The decomposed complex coefficient represents the information of amplitude and phase, which are used in various analysis process. In this section, Fourier and wavelet transforms and their fundamental applications are explained.

3.1.1 Fourier Transform

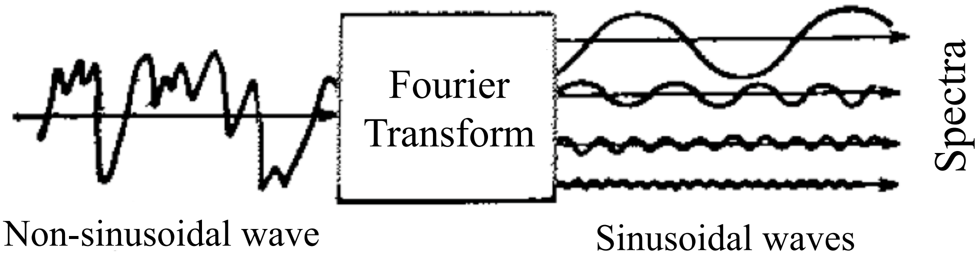

FIG. 3.1: Image of Fourier transform.

Fourier transform is a well-known method to decompose complicated wavefroms to sinusoidal waves, which contain amplitude and phase information [85]. A schematic of Fourier transform is described in Fig. 3.1. Fourier transform of time series $x(t)$ is defined as,

$$X(f) = \int_{-\infty}^{\infty} x(t) e^{-i2\pi f t} dt, \tag{3.1}$$

and inverse Fourier transform is defined as,

$$x(t) = \int_{-\infty}^{\infty} X(f) e^{i2\pi f t} df. \tag{3.2}$$

Here $X(f)$ indicates Fourier component of $x(t)$ at frequency f. Since $X(f)$ is obtained from the real numbers of $x(t)$, it becomes complex number, and satisfies $X(f) = X^{*}(-f)$. Fourier components of each frequency can be described as,

$$X(f) = |X(f)| \, e^{i\theta(f)}, \tag{3.3}$$

where $|X(f)|$ and $\theta(f)$ indicate amplitude and phase of Fourier components. To transform experimental discrete data, restriction of time resolution and finite time series length can not be avoided. Thus, for the discrete signal x_p ($p = 0 \cdots N-1$), discrete Fourier transform is adopted as,

$$X_n = \frac{1}{N}\sum_{p=0}^{N-1} x_p \mathrm{exp}\left(\frac{-i2\pi pn}{N}\right), \tag{3.4}$$

and inverse discrete Fourier transform is defined as,

$$x_p = \sum_{n=0}^{N-1} X_n \mathrm{exp}\left(\frac{i2\pi pn}{N}\right). \tag{3.5}$$

Here X_n represents discrete Fourier components. Discrete Fourier transform is usually demonstrated with fast Fourier transform (FFT) algorithm. If Fourier transform is applied to N size data in the manner of Eq. (3.4), N^2 number of calculations are required. On the other hand, FFT requires $N\log N$ number of operations. When the data size N increases, FFT is much faster than the direct calculation of Eq. (3.4).

Fourier transform can be applied to spatial series of data and it provides wave number information, i.e. mode number. Discrete Fourier transform in spatiotemporal signal $z_{p,q}$ is defined as,

$$Z_{n,m} = \frac{1}{NM}\sum_{p=0}^{N-1}\sum_{q=0}^{M-1} z_{p,q} \mathrm{exp}\left[-2\pi i\left(\frac{pn}{N} - \frac{qm}{M}\right)\right], \tag{3.6}$$

where $f = n\Delta f$ (Δf is a frequency resolution), m is a mode number, $t = p\Delta t$ (Δt is a time resolution) and $x = q\Delta x$ (Δx is a spatial resolution). N and M indicate number of measurement times and points. Great benefit of two-dimensional Fourier transform is that propagation direction of fluctuation movement can be identified. One-dimensional Fourier transform of real signals can not distinguish between positive or negative frequency (or mode number) components, due to symmetry between Fourier components and its complex conjugate, i.e., $X_n = X^*_{-n}$. Two-dimensional Fourier transform can distinguish between the positive and negative frequency (or mode number) as $Z_{n,m} \neq Z^*_{-n,m}$ (or $Z_{n,m} \neq Z^*_{n,-m}$). Therefore, mode number can be defined as $m = -M/2 \sim M/2 - 1$ for $f = 0 \sim (N-1)\Delta f/2$, or frequency can be defined as $f = -N\Delta f/2 \sim (N-1)\Delta f/2$ for $m = 0 \sim M/2 - 1$. In PANTA, 64ch probe measurement signals are frequently used to determine fluctuations rotation direction.

3.1.2 Wavelet Transform

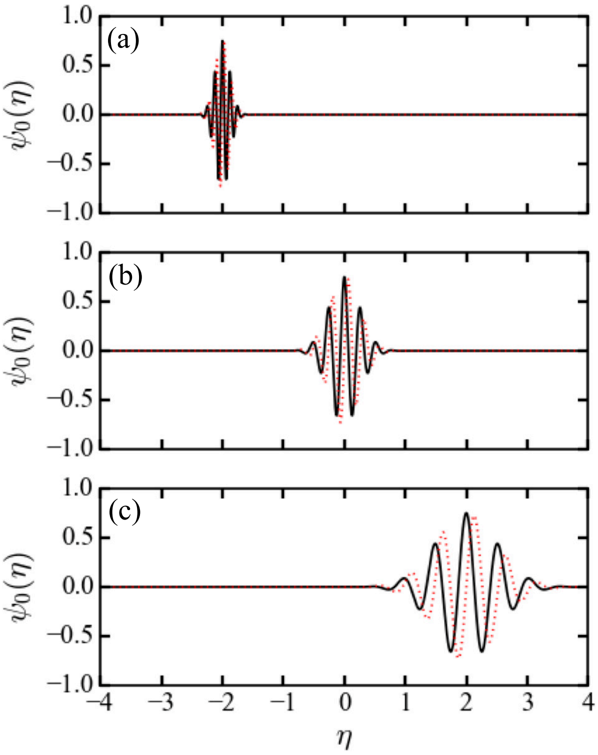

FIG. 3.2: Morlet wavelet with different scale and position in the case of the dimensionless frequency $\omega_0 = 6$. Black and red lines are real and imaginary part of the function, respectively.

The wavelet transform is commonly used as dynamical analysis. Compare to Fourier transform, wavelet basis function changes its scale in time and frequency space. The wavelet transform is conducted through convolution of the signal with the basis functions $\psi_0(\eta)$, where η is dimensionless time parameter, such as,

$$W(s,\tau) = \frac{1}{\sqrt{s}} \int_{-\infty}^{\infty} x(t)\, \psi_0^* \left(\frac{t-\tau}{s} \right) dt. \tag{3.7}$$

Here, s and τ indicate the scale and position of the basis function, respectively. Although there are several basis functions, Morlet wavelet is introduced here [86]. The Morlet wavelet is constituted by the sinusoidal wave modulated by the Gaussian as,

$$\psi_0(\eta) = \pi^{-1/4} e^{i\omega_0 \eta} e^{-\eta^2/2}, \tag{3.8}$$

where ω_0 denotes the dimensionless frequency. Figure 3.2 shows the Morlet wavelet of $\omega_0 = 6$ with different position and scale. The Morlet wavelet optimizes its position and scale to maximize the most efficient time and frequency resolutions.

3.1.3 Applications

Fourier and wavelet transforms decompose signals to frequency or wavenumber components. The coefficient of each component is usually expressed as complex number, thus there are several techniques to extract real information from amplitude and phase from the coefficient. Some important applications and verification are mentioned in this subsection. Note that the following explanations are only represented for Fourier coefficient $X(f)$, but the wavelet coefficient $W(s,\tau)$ is also can represent as same formula.

- **Auto power spectrum**

Energy of each component is estimated by its squared amplitude as $|X(f)|^2$. Obtained Fourier components are extracted from the observed signals in range of

$[-T/2, T/2]$. Thus auto power spectral density function $P(f)$ is defined as,

$$P(f) = \lim_{T\to\infty} \frac{1}{T} \langle X(f) X^{*}(f) \rangle, \tag{3.9}$$

where the bracket $\langle\cdot\rangle$ represents ensemble average. Auto power spectrum $P(f)$ denotes contributions to the total fluctuation power through frequency range within $f \sim f + df$. Therefore, the summation of auto power spectrum is identified with squared time averaged fluctuation signal as,

$$\bar{x}^2 = \lim_{T\to\infty} \frac{1}{T} \int_{-T/2}^{T/2} x^2(t)dt = \int_{-\infty}^{\infty} P(f)df. \tag{3.10}$$

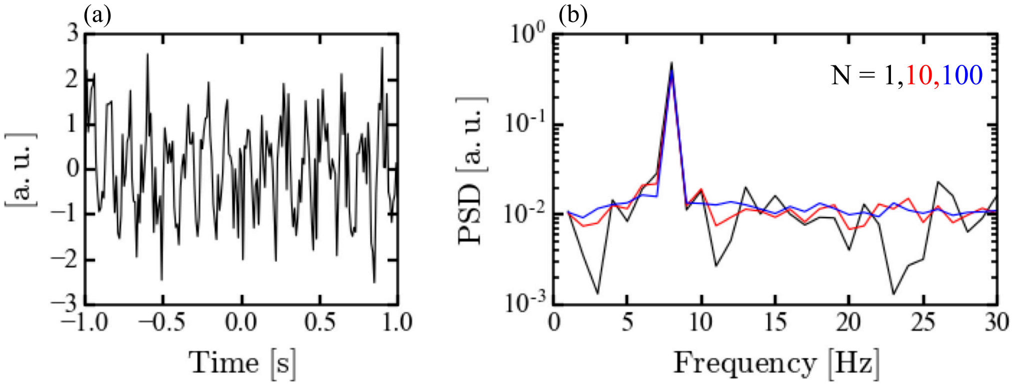

FIG. 3.3: (a)Test signal. (b) Auto power spectrum of the test signal with different ensemble number N.

If the signal $x(t)$ obeys Gaussian distribution, estimated power spectrum without ensemble averaging has relative error of 100%. One of the methods to reduce the error is the ensemble averaging. The verification study is introduced here. The test signal of $x(t) = \sin(2\pi f t) + \text{noise}$, where $f = 8$ Hz and the noise expresses the white Gaussian noise with a standard deviation of 0.8, is shown in Fig. 3.3(a). The auto power spectrum with different ensemble number N are shown in Fig. 3.3(b). It is obvious that the error of the spectrum decrease as the number of ensemble averaging increases. When data are independent from one another, variance of the power spectrum decreases with $1/N$.

- **Cross Power Spectrum**

Relationship between two different signal can be analysed by cross power spectrum. Cross power spectrum between $x(t)$ and $y(t)$ can be described as,

$$S_{xy}(f) = \lim_{T\to\infty} \frac{1}{T}\langle X^*(f)Y(f)\rangle. \tag{3.11}$$

Since cross power spectrum is generally complex, the spectrum can be written as,

$$S_{xy}(f) = \frac{1}{T}\langle |X(f)|\,|Y(f)|\,e^{-i\theta_{xy}(f)}\rangle. \tag{3.12}$$

Here, Eq. (3.3) is used. The $\theta_{xy}(f)$ is known as cross phase, indicating averaged phase difference at frequency f. The cross phase is obtained as,

$$\theta_{xy}(f) = \tan^{-1}\frac{\mathrm{Im}\left[S_{xy}(f)\right]}{\mathrm{Re}\left[S_{xy}(f)\right]}. \tag{3.13}$$

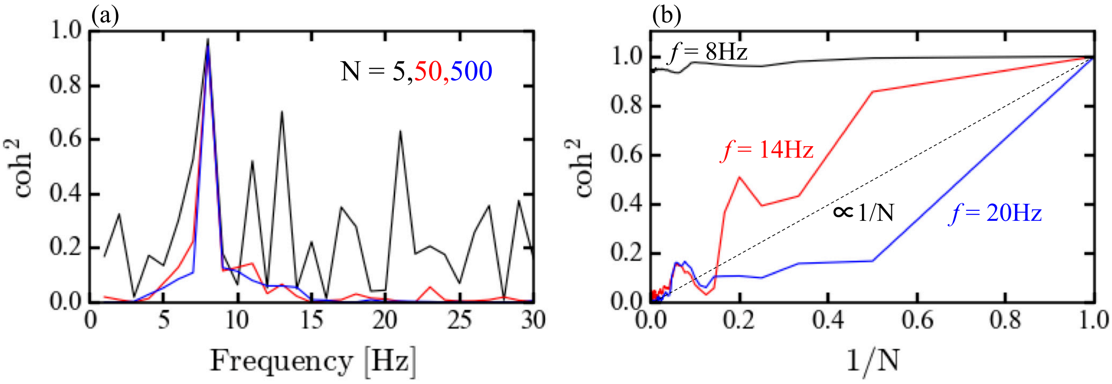

FIG. 3.4: (a)Spectrum of cross coherence for test data. (b) The convergence study shows that the noise of squared cross coherence decrease with $1/N$.

For quantifying correlation between different two signals, cross coherence is usually used. Squared cross coherence is a normalized quantity of cross power spectrum and defined as,

$$\mathrm{coh}^2_{xy}(f) = \frac{|S_{xy}(f)|^2}{S_{xx}(f)S_{yy}(f)}, \tag{3.14}$$

where $S_{xx}(f)$ and $S_{yy}(f)$ are auto power spectra of $x(t)$ and $y(t)$, respectively. Cross coherence shows the degree of conservation of the cross phase.

The error of the cross coherence decreases with the averaging number of ensemble. The test signals of $x(t) = \sin(2\pi f_1 t) + \text{noise}$, and $y(t) = \sin(2\pi f_1 t + \pi/2) + \sin(2\pi f_2 t) + \text{noise}$ are used here, where $f_1 = 8$ Hz, $f_2 = 14$ Hz and the noise expresses white Gaussian noise of standard deviation of 0.8, respectively. The obtained cross coherence with different averaging number of ensemble is shown in Fig. 3.4(a). It is clear that the coherence except $f = 8$ Hz decrease with ensembles. The decrease of the error can be considered by convergence study, as shown in Fig. 3.4(b). The reduction of the noise components of $f = 14$ and 20 Hz are proportional to the inverse of the number of ensemble, $1/N$.

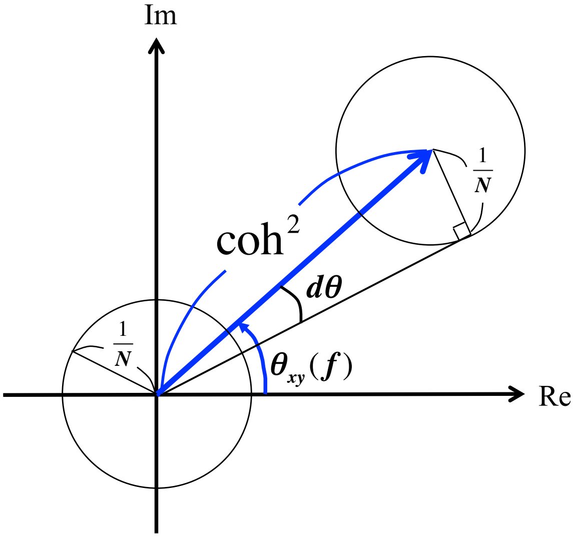

FIG. 3.5: Image of error estimation of the cross phase.

The error of the cross phase can be evaluated deduced from the error of the cross coherence. The image of the error estimation of cross phase is shown in Figure 3.5. Since the confidential level of squared cross coherence is described with $1/N$, the error of cross phase $d\theta$ could represent as,

$$d\theta = \arcsin\left(\frac{1/N}{\mathrm{coh}^2}\right). \tag{3.15}$$

• Auto bi-spectrum

Bispectral analysis is an essential tool in quantifying the conservation of phase relation among three waves couplings. Three-wave nonlinear coupling such as disparate scale interactions or parametric modulation instability are evaluated by the method [87,88]. Auto bi-spectrum shows the degree of coupling between three waves with frequencies f_1 , f_2 and f_3, where the matching condition, $f_1 + f_2 = f_3$ is satisfied. Auto bi-spectrum is defined as,

$$\hat{B} = \langle X(f_1)X(f_2)X^*(f_3)\rangle, \tag{3.16}$$

where $X(f_1)$, $X(f_2)$ and $X(f_3)$ indicate frequency components of time series $x(t)$. Auto bi-spectrum becomes finite if the phase relation between $X(f_1)$, $X(f_2)$ and $X(f_3)$ is constant. It is convenient to define the normalized quantity, i.e., squared auto bi-coherence $\hat{b}^2$, in order to estimate the occurrence of three-wave coupling qualitatively as,

$$\hat{b}^2(f_1, f_2) = \frac{|\hat{B}(f_1, f_2)|^2}{\langle|X(f_1)X(f_2)|^2\rangle\langle|X(f_3|^2\rangle}. \tag{3.17}$$

The confidence level of the squared auto bi-coherence is $1/N$, indicated in Ref. [89]. The bi-phase is the phase relations among three waves, and is defined as

$$\theta_b(f_1, f_2) = \tan^{-1}\frac{\mathrm{Im}\left[\hat{B}(f_1, f_2)\right]}{\mathrm{Re}\left[\hat{B}(f_1, f_2)\right]}. \tag{3.18}$$

Auto bi-coherence indicates the degree of conservation of bi-phase.

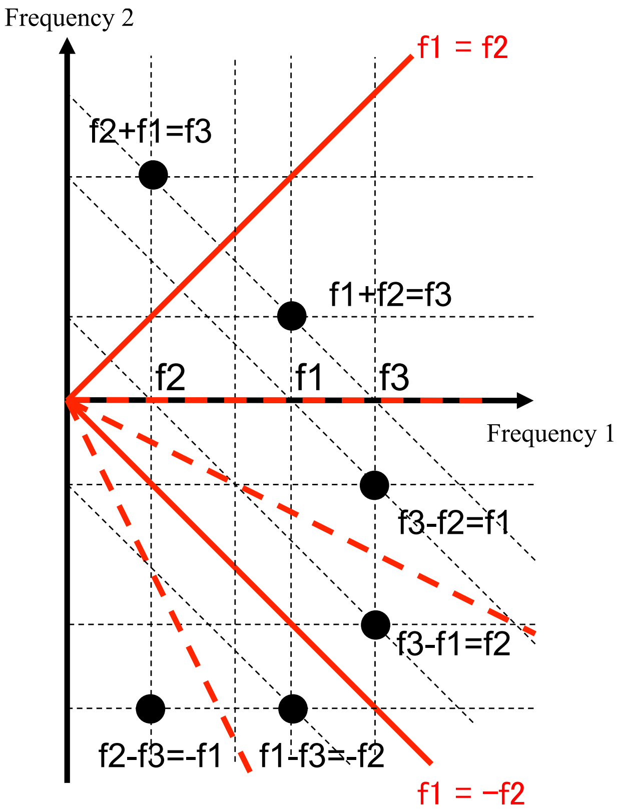

FIG. 3.6: Schematic of symmetry of squared auto bi-coherence. Black points indicate the same meaning.

Squared auto bi-coherence has symmetric relationship in f_1 - f_2 space as shown in Fig. 3.6. Every black points in the figure show the same physical meaning, i.e., three-wave coupling of $f_1 + f_2 = f_3$. The mathematical reason of symmetry of real part of squared auto bi-coherence is due to the symmetry of auto bi-spectrum, as expressed in the following.

$$\begin{aligned}
\hat{B}(f_1, f_2) &= \hat{B}^*(-f_1, -f_2) \\
&= \hat{B}(f_2, f_1) \\
&= \hat{B}(f_1, -f_1 - f_2) \\
&= \hat{B}(f_2, -f_2 - f_1) \\
&= \hat{B}^*(-f_2, -f_1)
\end{aligned}$$

From the top of the equations denote that point symmetry in f_1-f_2 coordinate, $f_1 = f_2$ line symmetry, symmetrical point across the horizontal line $f_2 = 0$, symmetrical point across the vertical line $f_1 = 0$ and $f_1 = -f_2$ line symmetry, respectively, as shown in Fig. 3.6.

The total bi-coherence is useful for analysing the contribution of many mode couplings to a certain mode f_3. It is defined as,

$$\hat{b}^2_{Total}(f_3) = \sum_{f_3 = f_1 + f_2 = const.} \hat{b}^2(f_1, f_2). \tag{3.19}$$

3.2 Numerical filter

Techniques of numerical filter can extract specific frequencies or mode ranges from signals instantaneously. Such extracted time series are useful to study dynamics of fluctuations. In this subsection, the basic idea of numerical filter and its applications, spatial filter and Hilbert transform are explained.

3.2.1 Temporal filter

Temporal filter is fundamental of the numerical filter to extract the specific frequency components from the raw signal. The temporal filter can be conducted through the convolution of raw signal $x(t)$ with window function $h(j)$ as,

$$\hat{x}(t) = \sum_{j=-m}^{m} h(j)x(t - j\Delta t), \tag{3.20}$$

where $\hat{x}(t)$ is the filtered signal. Δt is a sampling time and order of the filter is $k = 2m + 1$. When a sinusoidal wave $x(t) = \exp(i2\pi f t)$ is input to the system, the filtered signal is obtained as

$$\begin{aligned} \hat{x}(t) &= \mathrm{e}^{i2\pi f t} \sum_{j=-m}^{m} h(j)\mathrm{e}^{-i2\pi j f \Delta t} \\ &= e^{i2\pi f t} H(f) \\ &= |H(f)|\, e^{i(2\pi f t+\theta)}. \end{aligned} \tag{3.21}$$

Therefore, the amplitude of the input signal is modified by transfer function $H(f) = \sum_{j=-m}^{m} h(j)\mathrm{e}^{-i2\pi j f \Delta t}$, which is Fourier transform of the window function $h(j)$. It is noted that transfer function could change the phase of the input signal, as denoted as θ in Eq. (3.21). Since the phase delay θ should manage to be 0, the window function $h(j)$ should be finite and even function. Such a filter is called as finite impulse response (FIR) filter.

The goal of numerical filter is designing $h(j)$ for required frequency operation such as low-pass filter, high-pass filter, band-pass filter and band-reject filter. The window function $h(j)$ is obtained by inverse Fourier transform of $H(f)$. The most suitable transfer function $H(f)$ is obtained by using least squares method,

$$\delta = \int |H_{ideal}(f) - H(f)|^2\, df, \tag{3.22}$$

where $H_{ideal}(f)$ is an ideal transfer function. The design of $H(f)$ is determined to minimize the value δ.

For applying a low-pass filter, the least squares method provides transfer function as,

$$H(F) = \begin{cases} 1 & (0 \leq |F| \leq F_c) \\ 0 & \left(F_c \leq |F| \leq \frac{1}{2}\right) \end{cases}, \tag{3.23}$$

where $F = f\Delta t$ and $F_c = f_c\Delta t$ are normalized frequency and cut-off frequency, respectively. The inverse transform gives window function as,

$$h(j) = \begin{cases} 2F_c & (j = 0) \\ \frac{\sin 2\pi F_c j}{\pi j} & (j \neq 0) \end{cases}. \tag{3.24}$$

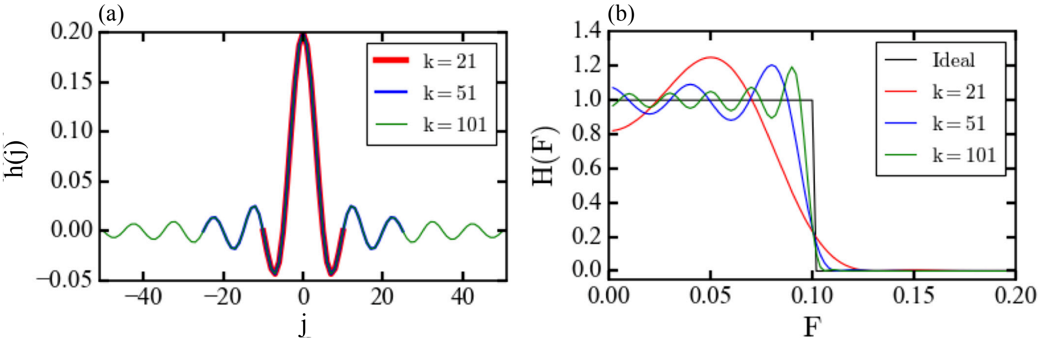

FIG. 3.7: (a) Window functions with different filter order k. (b) The ideal transfer function and obtained transfer function with different filter order. Here, the cut-off frequency is $F_c = 0.1$.

Obtained window function and transfer function with different filter order k are shown in Fig. 3.7(a) and (b), respectively. The cut-off frequency $F_c = 1$ is set. It is clear that the quality of the transfer function $H(f)$ depends on the filter order k. Increase of k makes the transfer function sharper at the cut-off frequency. However, ripples around the cut-off frequency do not disappear even if k increases (this is called as Gibbs phenomenon). Therefore, modification of the filter design is performed next.

The modification of ideal transfer function is shown in black line in Fig.3.8(b).

The discontinuity at the cut-off frequency disappears by inserting the slope as,

$$H(F) = \begin{cases} 1 & (0 \le |F| \le F_1) \\ \frac{F_2 - F}{2\Delta} & (F_1 \le |F| \le F_2) \\ 0 & \left(F_2 \le |F| \le \frac{1}{2}\right) \end{cases}, \tag{3.25}$$

where F_1 and F_2 indicates the start and end of the slope of frequency values, respectively. The Δ represents the half width of the slope, defined as $\Delta = (F_2 - F_1)/2$, and the cut-off frequency is defined as $F_c = (F_2 + F_1)/2$. The inverse Fourier transform of Eq. (3.25) derives window function as,

$$h(j) = \begin{cases} 2F_c & (j = 0) \\ \frac{\sin(2\pi F_c j)}{\pi j} \frac{\sin(2\pi j/k)}{2\pi j/k} & (j \neq 0) \end{cases}. \tag{3.26}$$

The modified window function and transfer function are shown in Fig. 3.8. The ripple almost disappears in modified transfer function.

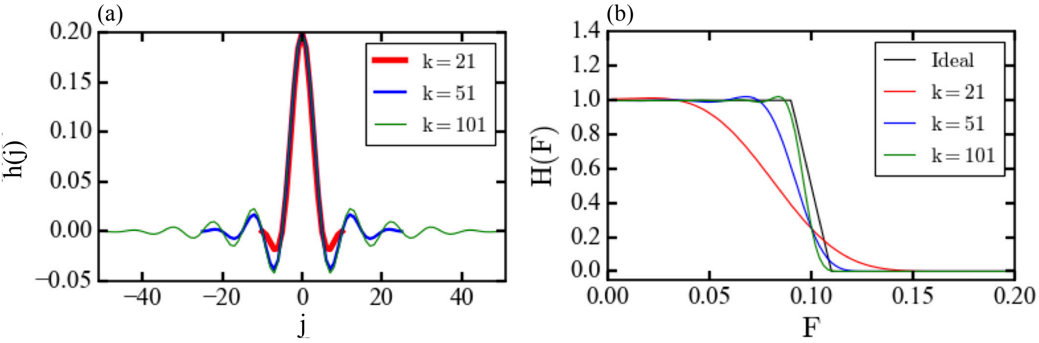

FIG. 3.8: (a) Modified window functions with different filter order k. (b) The modified ideal transfer function and obtained modified transfer function with different filter order. Here, the cut-off frequency is $F_c = 0.1$.

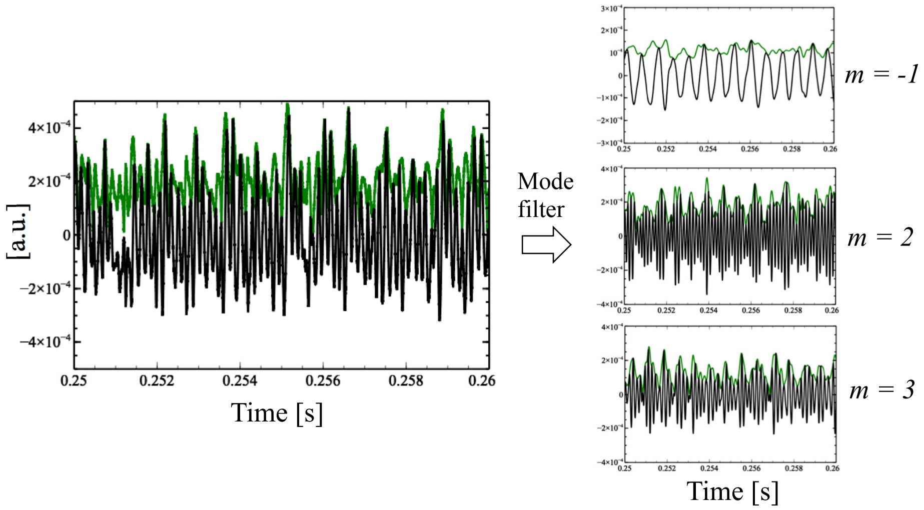

FIG. 3.9: Configuration of numerical spacial filter. The raw signal is decomposed to each mode number instantly. The green line indicates the envelope of each signals.

3.2.2 Spacial filter

The numerical spacial filter is developed through using 64ch probe signal. Image of the spacial filter is described in Fig. 3.9. The spatial filter is advantageous to decompose spatial-temporal series of signals into instantaneous temporal series of mode components, even positive or negative mode number.

The basic idea of the spacial filter is employing 2-dimensional Fourier transform. The process of extracting $m = +m_1$ is demonstrated in the following; (i) applying 2-dimensional Fourier transform to the spatio-tempolal raw signal as mentioned in Eq. (3.6). (ii) Extracting and combine one mode ($m = +m_1$, $f > 0$) and another mode ($m = -m_1$, $f < 0$) components. (iii) Demonstrate inverse Fourier transform in frequency domain. Figure 3.10 shows schematics of above (ii) process.

The obtained temporal series conserves the mode amplitude and phase, which was confirmed by the spectral analysis. The spacial filter provides to observe each fluctuations dynamics without degradation of temporal resolution.

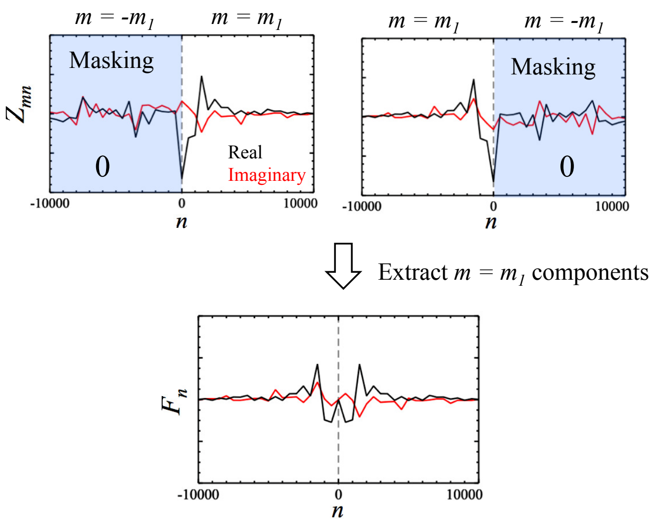

FIG. 3.10: The image of the process of spatial filter.

3.2.3 Hilbert transform

For obtaining time evolution of fluctuation amplitude and phase, Hilbert transform is available. Fourier component $X(t)$ of time series $x(t)$ can be converted to $\hat{X}(f)$ by,

$$\hat{X}(f) = -i\mathrm{sgn}(f)X(f), \tag{3.27}$$

where function $\mathrm{sgn}(f)$ is defined as,

$$\mathrm{sgn}(f) = \begin{cases} 1 & f > 0 \\ 0 & f = 0 \\ -1 & f < 0 \end{cases}.$$

Hilbert transform is performed by conducting inverse Fourier transform to $\hat{X}(f)$ as,

$$\hat{x}(t) = \mathcal{F}^{-1}\left[\hat{X}(f)\right], \tag{3.28}$$

where $\mathcal{F}^{-1}$ indicates inverse Fourier transform. This process is called Hilbert transform. Analytical signal $y(t)$ is obtained from $x(t)$ and $\hat{x}(t)$ as

$$y(t) = x(t) + i\hat{x}(t). \tag{3.29}$$

In this way, the analytical signal is complex and relation between $x(t)$ and $\hat{x}(t)$ is orthogonal. Finally, instant wave components of amplitude $A(t)$ and phase $\theta(t)$, can be written as,

$$\begin{aligned} A(t) &= \sqrt{x(t)^2 + \hat{x}(t)^2} \qquad (3.30)\\ \theta(t) &= \tan^{-1}\frac{\hat{x}(t)}{x(t)}. \qquad (3.31) \end{aligned}$$

3.3 Conditional Averaging

Conditional averaging is widely performed to quantify non periodic signals, which is not valid for Fourier transform [90–92]. Process of conditional averaging is carried out as follows. First, we determine the timing when interested phenomena happen in signal $x(t)$, and extract timing as "clocks". The i-th clock, t_i, is set to the origin of the temporal window, and the conditionally averaged signal $\bar{x}(\tau)$ is derived as,

$$\bar{x}(\tau) = \frac{1}{N}\sum_{j=1}^{N} x(t_j + \tau), \tag{3.32}$$

where N is the number of clocks, τ is defined as $\tau = -M\Delta t/2, ..., 0, ..., (M-1)\Delta t/2$, and M and Δt are the number of points in the temporal window and sampling time, respectively.

The arbitrariness of the conditional averaging is the choice of the clocks. There are lots of methods to determine the clock. Here, three representative methods are introduced in next subsections.

3.3.1 Threshold method

Threshold method is useful to detect the bursty events, e.g., edge localized mode (ELM) [93] and blobs [94]. This method is very simple; determine the threshold value and extract local peaks, which are above the threshold. Figure 3.11(a) shows the density bursts, which is detected by Doppler reflectometer, in ASDEX-Upgrade [95, 96]. The bursts are observed in the I-mode (Intermidiate mode) confinement state [97, 98], which is one of the interesting candidates for ITER discharge operation. The σ_L represents the standard deviation of the turbulence amplitude in L-mode. Here, the threshold value is determined as $5\sigma_L$, and the clocks or trigger function is extracted, as shown in Fig. 3.11(b).

Note that the threshold method is simple and useful, however, the conditionally averaged signal strongly depends on the data processing. This is again mentioned in the subsection 3.3.4.

3.3.2 Phase tracking method

Phase tracking method is efficient for extracting the nonlinear waveform [91,99]. The advantage of the technique, compared to the numerical filter, is its capability to extract the harmonic components as well as the fundamental one simultaneously, and removing the noise efficiently; thus, the technique can extract the nonlinear characteristics of the waves directly.

Figure 3.12(a) shows the raw signal of the ion saturation current in the streamer discharge. The low frequency components, mediator, are periodically detected with its fundamental frequency of $f = 1.7$ kHz, as shown in blue line in Fig. 3.12(a). The phase of the fundamental components of the mediator, $f = 1.7$ kHz,

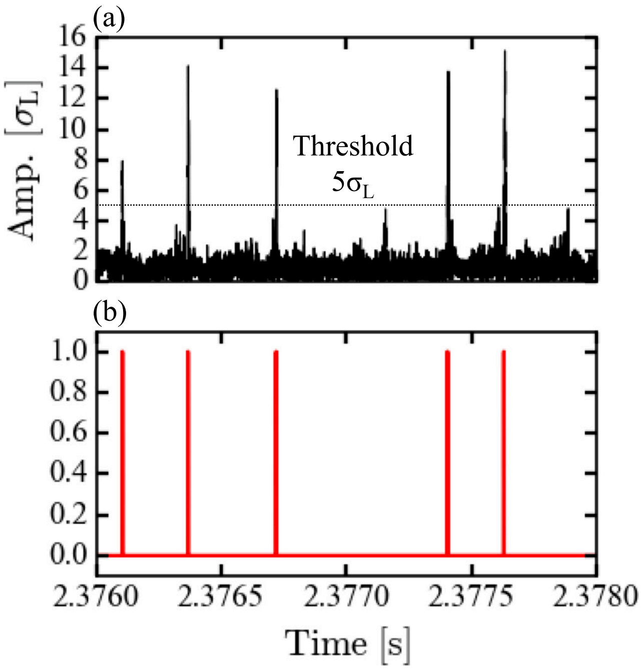

FIG. 3.11: Example for the threshold method. (a) Time evolution of the density bursts. (b) Trigger function that represents the clocks.

are tracked by the short time Fourier transform, as shown in Fig. 3.12(b). Then, the timings when the phases become zero are determined as the clocks, as shown in Fig. 3.12(c).

The higher harmonic components of the mediator remains if the phase relationship between the harmonics and the fundamental waves are conserved. The nonlinear waveform and its characters are discussed in the chapter 4.

3.3.3 Template method

Template method is developed in heartbeat analysis of medical field, and now starts to be applied in plasma experiments [48, 99, 100]. The template is a waveform, which is provided by iteration. Therefore, template method provides strong uniformity, since the template is iterated calculation until the convergence.

Here, the magnetic fluctuations measured by Mirnov coils in ASDEX Upgrade

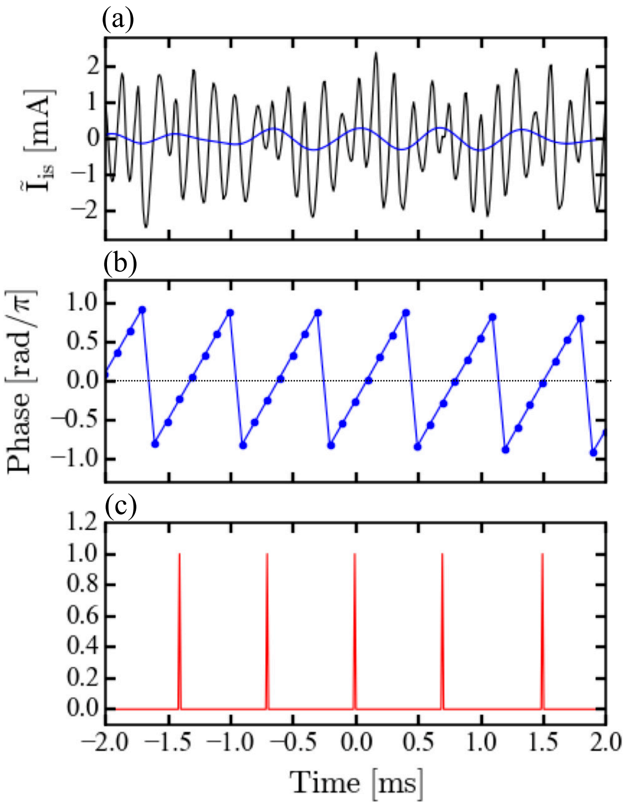

FIG. 3.12: Example for the phase tracking method. (a) Raw signal of the ion saturation current. Blue line indicate the low frequency components of $f = 1.7$ kHz. (b) Time evolution of the phase of $f = 1.7$ kHz components. (c) Trigger function that represents the clocks.

in the I-mode plasma are used for test analysis. Figure 3.13(a) shows that the magnetic fluctuations increase intermittently. In the I-mode plasma, the bursts are not only observed in the Doppler reflectometer, as shown in 3.11(a), but also in the Mirnov coils.

In the beginning, the method requires initial template for the first iteration. The initial template is usually chosen as a waveform similar to target signals. Here, the modified triangle wave shown in the black line in Fig. 3.13(c) are prepared for the initial template. The cross correlation $C_i(t)$ between raw signal $x(t)$ and the

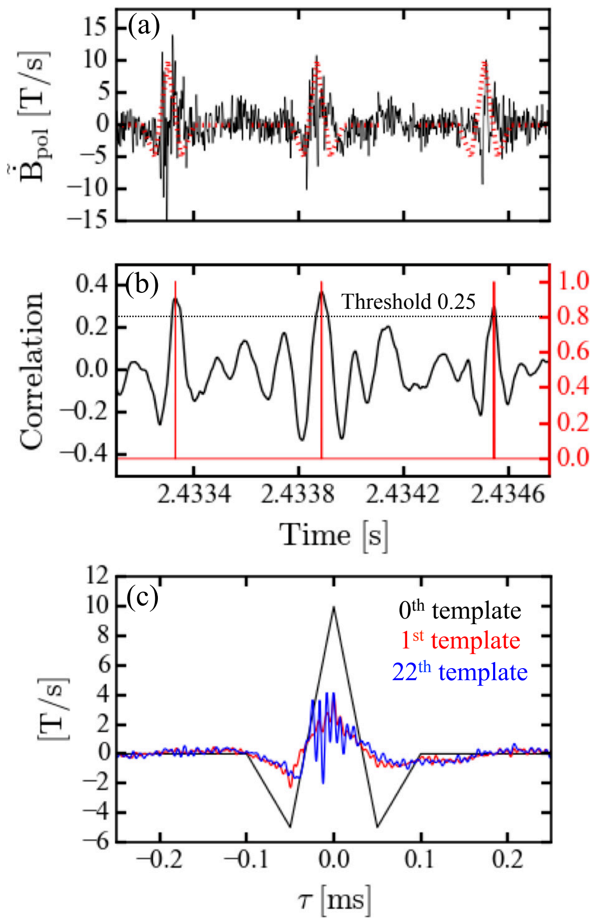

FIG. 3.13: Example for the template method. (a) Raw signal of the magnetic fluctuations with over-plot of the initial template as red dotted line. (b) Time evolution of the cross correlation and trigger function. (c) The 0th (initial), 1st and 22th (converged) templates are shown.

initial template $X_i(\tau)$ is calculated as,

$$C_i(t) = \frac{\overline{x(t+\tau)\,X_I(\tau)}}{\sqrt{\overline{x(t+\tau)^2}}\,\sqrt{\overline{X(\tau)^2}}}, \tag{3.33}$$

where $\bar{f}$ indicates the time average of f and the subscript i is the number of iteration ($i = 0$ is the initial iteration). Obtained cross correlation ($i = 0$) is shown in Fig. 3.13(b). The next clocks are determined from the peak of the cross correlation, which is above some threshold value. Here, the peak above 0.25 is detected, and the trigger function is shown as the red line in Fig. 3.13(b). Using these clocks, the conditional averaging is applied, and then we obtain next waveform, which is shown as red line in Fig. 3.13(c). This process is initial iteration. Again, the iteration is continue until the template converges. In this case, the template completely converges with 22 iterations, which is shown in the blue line in Fig. 3.13(c).

For the template method, only the choice of the initial template is arbitrary. The efficiency of the template method is explained in the next subsection.

3.3.4 Application of the conditional averaging to the intermittent non-monotonically bursts

In this subsection, the performances of the two different methods, threshold and template methods, are compared. The test signal includes intermittent bursts observed in the I-mode on ASDEX-U. The I-mode is known as a reduced/unchanged heat/particle transport state, and the bursts are detected by Mirnov coils, Doppler reflectometry and bolometry [95]. However, the characteristics of the bursts detected by many diagnostics are not identical. For example, while the Doppler reflectometer detects the monotonically peaked burst, as shown in Fig. 3.11(a), the bursts observed by the Mirnov coils contains high frequency fluctuations and non-monotonically increasing bursts, as shown in Fig. 3.13(a). Therefore, careful investigation for the conditional averaging is necessary.

Here we focus on the magnetic bursts, which is detected by the Mirnov coils. The threshold method and the template method are compared for the verification study. Figures 3.14 show difference among three processed signals, which are (a) raw signal, (b) envelope of raw signal and (c) 100 kHz low-pass filtered signal, respectively.

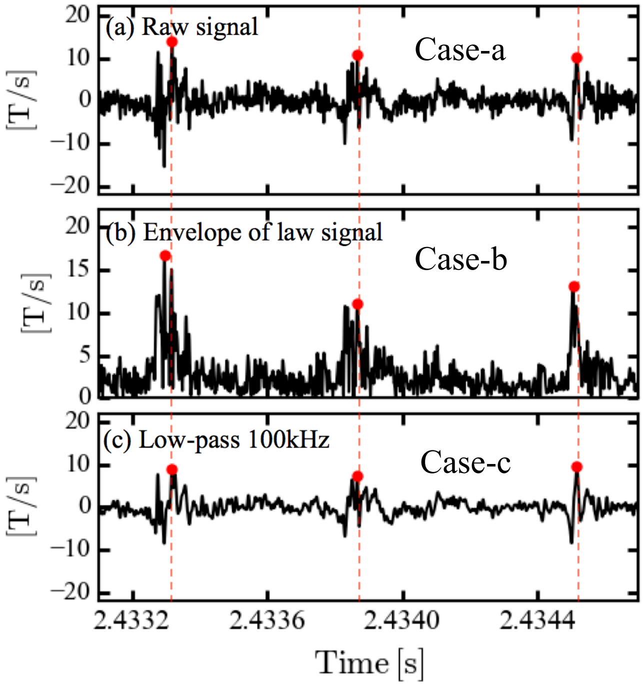

FIG. 3.14: Different three proceeded signals, (a) Raw signal, (b) envelope of the raw signal, and (c) low-pass 100 kHz signal are prepared for the verification study. For threshold method, thresholds are defined as 10, 10 and 7 T/s, respectively. The red points indicate the local peaks, where the timing are defined as clocks.

First, results of the threshold method is shown in Fig. 3.14. The peak of each signal, which is above the threshold values of 10 T/s, 10 T/s and 8 T/s, is extracted as clocks for the conditional averaging. The red points in Fig. 3.14 show the detected clocks, which seem not to be identical among different signals. These clocks are applied to raw signal to extract the events of bursts, and the timing of clocks are set as the center of the time window of 500 μs for the conditional analysis. Then, the obtained ensembles of data windows are averaged, and the averaged waveform at the bursts are estimated, as shown in Fig. 3.15. Fig. 3.15 (a), (b) and (c) show the extracted waveforms from the clocks obtained by raw signal, envelope of raw signal and low-pass 100 kHz filtered signal, respectively. These three cases in Fig. 3.15(a), (b) and (c) are named as Case-a, Case-b and

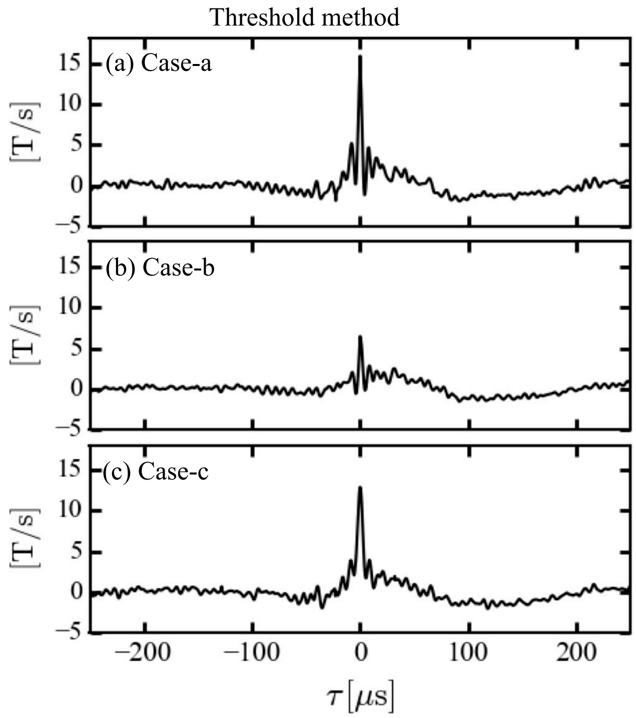

FIG. 3.15: Conditionally averaged waveforms obtained by threshold method are shown in (a) Case-a, (b) Case-b and (c) Case-c, respectively.

Case-c, respectively. These waveforms are clearly different from one another, in the point of their amplitudes, phases and temporal behaviours. This is due to difficulty in determining the peak values for such non-monotonously bursts. For the threshold method, reproducibility is poor, and the physical interpretation could depend on the signal processing.

Next, the template method is applied to the signals shown in Fig. 3.14. Comparing to the raw signal, it is obvious that the initial templates described in section 3.3.3 are not sufficient, since the converged template, shown in the Fig. 3.13, represents smaller amplitude. Hence, we use different initial template here. The initial template is determined by the statistical way, i.e., provided by the threshold method. The identical waveforms of Fig. 3.15(a), (b) and (c) are used as the initial template. We also named different process of template method as Case-a,

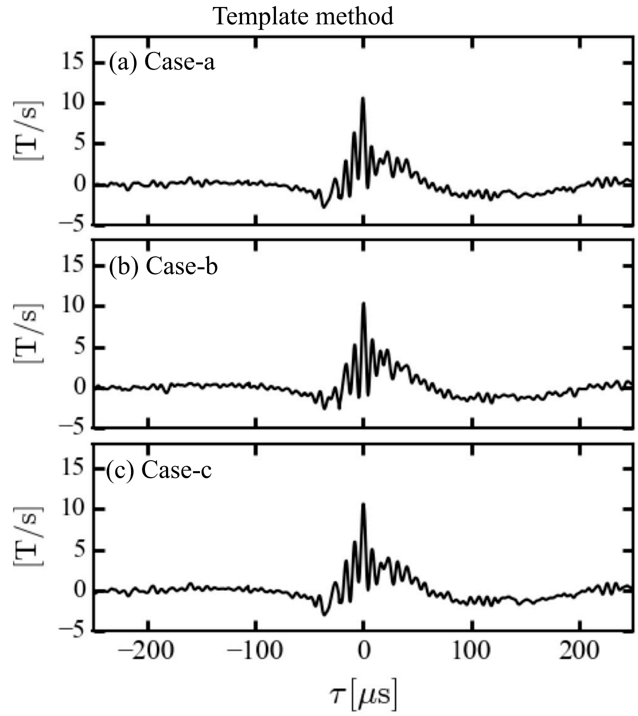

FIG. 3.16: Conditionally averaged waveforms obtained by template method are shown as (a) Case-a, (b) Case-b and (c) Case-c, respectively.

Case-b and Case-c again, similar to the case of the threshold method. Each initial template is applied to at the beginning of the iteration process with the thresholds of the correlation set to be 0.45. Figures 3.16(a), (b) and (c) show the converged waveforms of Case-a, Case-b and Case-c, respectively. In spite of the different initial templates, obtained waveforms seem to be very similar to one another.

For quantifying performance of the conditional averaging, first, the convergence study is performed. Figure 3.17 shows the convergence of the amplitude of the waveforms at $\tau = 0\ \mu$s for the threshold method and template method, respectively. The amplitude at $\tau = 0\ \mu$s are estimated from Hilbert transform, i.e., envelope of the signals. Horizontal axes in Fig. 3.17 are the inverse of the number of ensemble averaging, $1/N$. Here the ensemble number N is identical to the number of the clocks, which are (49, 79, 49) for Case-a, Case-b and Case-C of

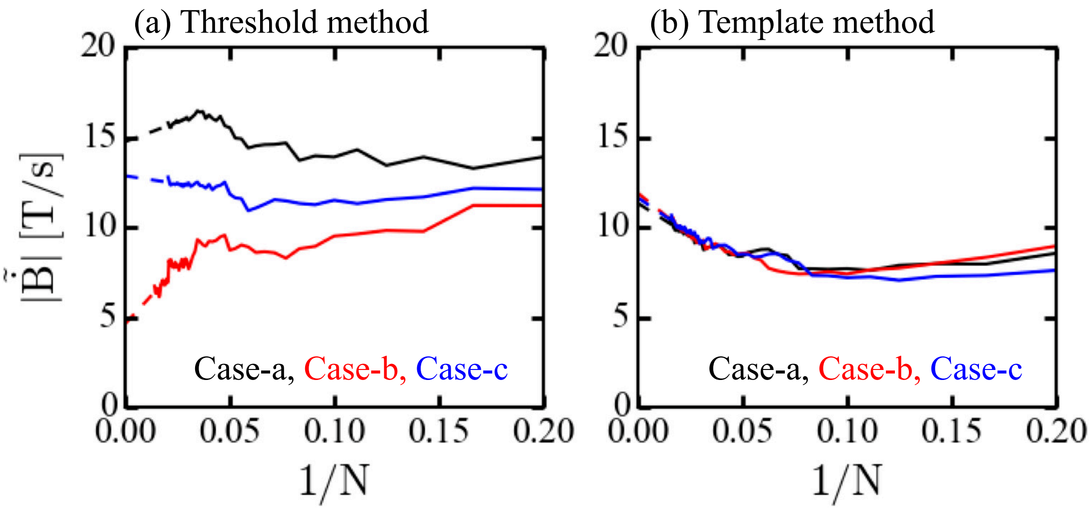

FIG. 3.17: Convergence of amplitude of obtained waveforms at $\tau = 0\ \mu$s. The Case-a (black), Case-b (red) and Case-c (blue) of (a) threshold method and (b) template method are shown. Here, amplitude is estimated as Hilbert transform and N means the number of ensembles for conditional averaging.

the threshold method, and (67, 61, 63) for Case-a, Case-b and Case-C of the template method, respectively. The amplitude converges towards the different values in case of the threshold method, as shown in Fig. 3.17(a). While results of the template method indicates that all cases converge towards almost the same values. The equivalent convergence of the peak value indicates that the template method doesn't depend on the initial template.

The direct comparison among results by using different clocks is also performed. Figure 3.18 shows probability density functions (PDF) of the time difference of the clocks from Case-a in threshold method and template method, respectively. The time lags of the clocks of Case-a and Case-b and those of Case-a and Case-c are calculated. The green/purple histogram indicates the time lag between Case-b/Case-c and Case-a. Compared to the threshold method, the both PDFs of the template method are concentrated around 0 μs, which indicates that properties of the clocks are similar. These results indicate that compared to the threshold

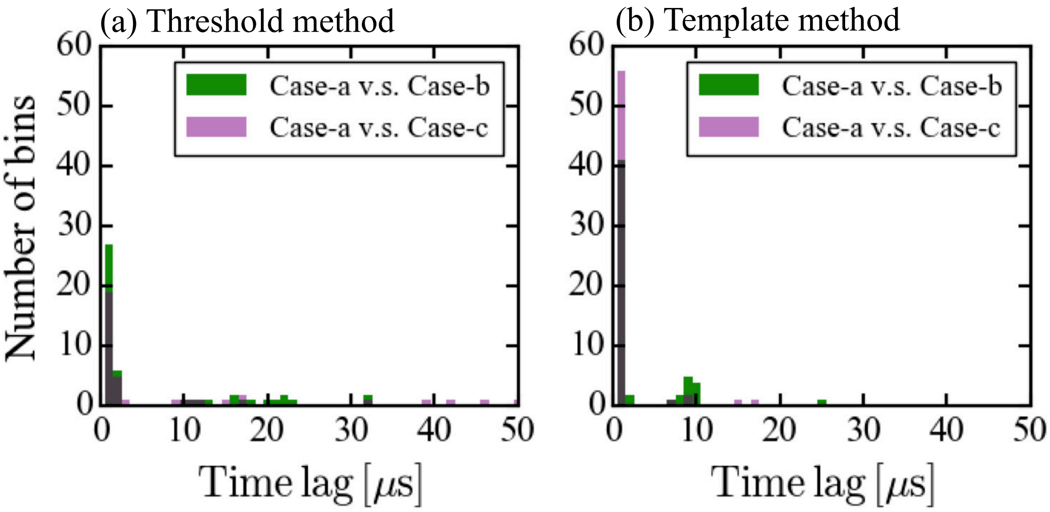

FIG. 3.18: PDF of the time difference between the clock of Case-a and Case-b (green) and the clock of Case-a and Case-c (purple) for (a) threshold method and (b) template method.

method, the template method doesn't depend on the different signal processing cases and provides unique results. Thus, template method is useful to quantify intermittent, non-monotonously peaked bursts.

To summarize the result of this subsection. For quantifying intermittent, non-monotonously peaked bursts, the conditional averaging is a strong technique, however, unique results are expected and shouldn't depend on process parameters. The threshold method and the template method are applied to the intermittent, non-monotonously peaked magnetic bursts observed at ASDEX-U. Different three cases of the both method are tested, and the template method provides more preferable results. In the three cases, the averaged waveforms are similar, and converge towards the same value of amplitude, and the clocks timings are almost identical. The results indicate that the template method can produce unique conditionally averaged waveforms, which enable us to understand the abrupt events quantitatively.

Chapter 4

Nonlinear structure and associated transport of streamer

As mentioned in Chapter 1, this thesis focuses on a streamer in PANTA, which is generated by the modulation of the drift waves through mediator [44, 45]. Figure 4.1 shows the mode-frequency (m and f) decomposed power spectrum. The previous works revealed that the linearly driven drift waves of (m, f) = (2, 8.4 kHz) are nonlinearly couple with the mediator, which appears in the spectrum as (m, f) = (-1, 1.7 kHz). There nonlinear coupling may generate the side-band modes, where are (m, f) = (3, 6.7 kHz) or (m, f) = (1, 10.1 kHz).

Up to date, the nonlinear coupling of the streamer and phase structure are studied, however, there are several questions remained. For instance, higher harmonic components of streamers, phase and amplitude structures of streamers, and the associated transport are not clarified. The conditional averaging technique is used to resolve the problems. In this chapter, first parameter dependence of the streamer is mentioned. Then, observation of the nonlinear spatio-temporal structure of the streamer are observed as nonlinear waves. Finally, transport mechanisms of streamers are discussed.

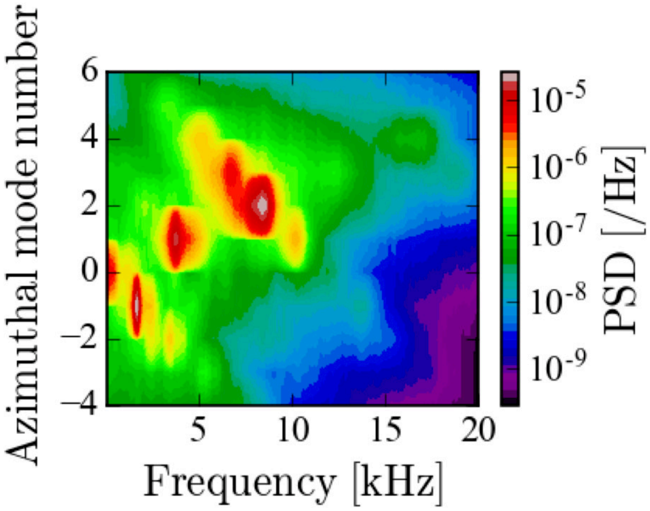

FIG. 4.1: Two-dimensional power spectrum of ion saturation current. The positive mode number indicates propagation in the electron diamagnetic direction.

4.1 Streamer condition

In PANTA, main external control parameters for plasmas are neutral gas pressure and magnetic field strength. The streamer is only observed in relatively low gas pressure. While the streamer exists under some conditions of the magnetic field strength [68]. Thus, the magnetic field dependence of the streamer has been observed in detail. In this section, the fluctuations including their radial structure and nonlinear couplings are studied by changing the magnetic field strength with constant RF power of 3 kW and constant gas pressure of 0.45 mTorr.

Since the streamer is formed by the nonlinear coupling between drift waves and the mediator, three-wave coupling is strongly conserved. Thus, the streamer is considered the significant correlation between the mediator and the envelope of drift waves. Figure 4.2(a) and (b) show the ion saturation current fluctuation of $m > 0$ components with its envelope and that of the mediator components of m = -1. The mode decomposed time evolution of fluctuations are extracted by spatial filter. The time evolution shows that the envelope and the m = -1 components seems to correlate.

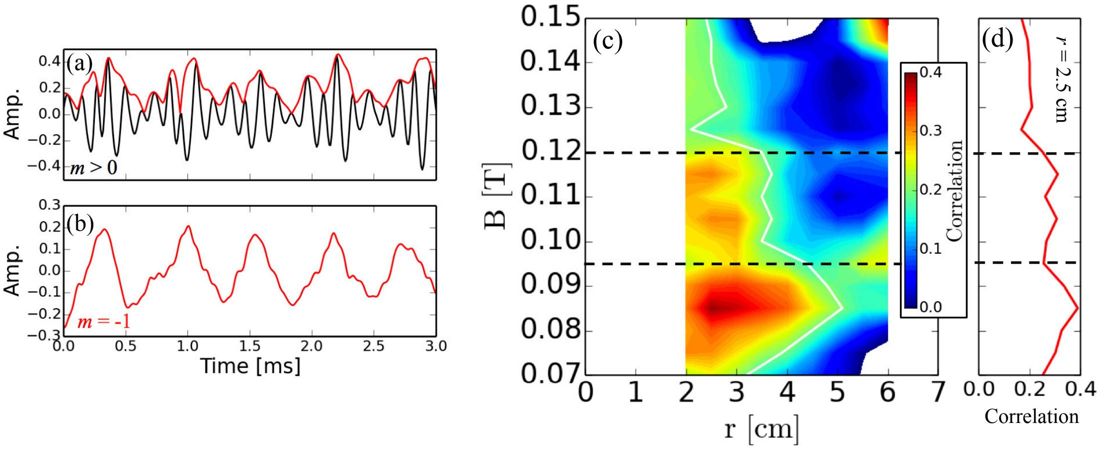

FIG. 4.2: Ion saturation current fluctuations of (a) m ¿ 0 components (drift waves) with its envelope and (b) m = -1 components (mediator), respectively. (c) Dependence of cross correlation between the envelope of $m > 0$ and m = -1 on magnetic fields and radial positions. (d) Magnetic field dependence of the correlation of (c) at r = 2.5 cm.

By changing the magnetic field, the radial profile of the maximum value of cross correlation coefficient between enelope of drift waves and the mediator are provided in Fig. 4.2(c), and the slice at r = 2.5 cm are shown in Fig. 4.2(d). The strong correlation between the envelope and the mediator are radially elongated in the low magnetic field condition. The conter plot also indicates that the magnitude of the correlation decreases with the magnetic field. Thus, the fluctuation status can be categorize to three conditions in terms of the magnetic field; (i) streamer conditions (B = 0.07 ~ 0.10 T), (ii) intermediate conditions (B = 0.10 ~ 0.12 T), (iii) solitary conditions [43, 68] (B = 0.12 ~ 0.15 T).

The waveforms and spectra of fluctuations are shown in Fig. 4.3. In Fig. 4.3(a), (d) and (g), a clear streamer structure is shown; the envelope of fluctuations rotates in the ion diamagnetic direction and the power spectrum constitutes the side band structure. For the B = 0.11 T, the waveform and associating side band spectrum change temporally. One side-band is similar to the streamer, but the

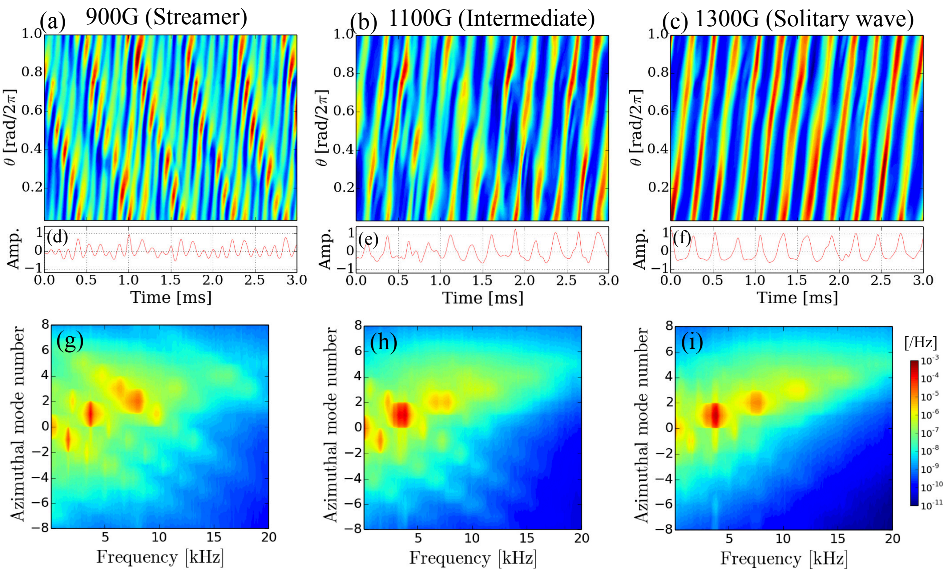

FIG. 4.3: (a)-(c) Spatio-temporal evolutions, (d)-(f) temporal evolutions and (g)-(i) power spectra of ion saturation current fluctuations under streamer, intermediate and solitary wave conditions. The positive θ and azimuthal mode number indicate the electron diamagnetic direction.

other is similar to the solitary waves. The clear solitary structure appears with high magnetic field, and constitutes the abruptly increasing waveform and higher harmonics spectrum, as shown in Fig. 4.3(c), (f) and (i). It is noted that the spectra show that the power of drift waves don't change significantly, or even increase with the magnetic field (or Larmor radius). In addition, it is observed that the inverse of density scale length (the strength of density gradient) decreases with the magnetic field strength. These are inconsistent with linear drift wave theory, where the linear growth rate decreases with Larmor radius and density scale length.

The changes of the fluctuations status are also seen in the nonlinear couplings. Figure 4.4 represents the auto bi-coherence of the ion saturation current fluctuation at $r = 4$ cm. In case of the streamer condition, the vertical line at $f_1 = 1.7$ kHz are seen. This line indicates the couplings between the mediator and other modes.

Drift waves of f_2 = 8.4 kHz and its side-band 6.7 kHz have a strong value, which indicates the three-wave coupling between the drift waves and the mediator. In the intermediate state, weak but finite couplings with the mediator are seen. In addition, the large self-coupling of $f_1 = f_2$ = 4.0 kHz are investigated. The dynamical observation of bi-coherence revealed that the combination of nonlinear couplings changes, as well as the waveform of fluctuations changes in time. In the high magnetic field condition, the nonlinear characteristics of solitary waves are clearly shown that the fluctuation at f_1 = 4.0 kHz is interacted with its higher harmonics at f_2 = 8.0 or 12.0 kHz.

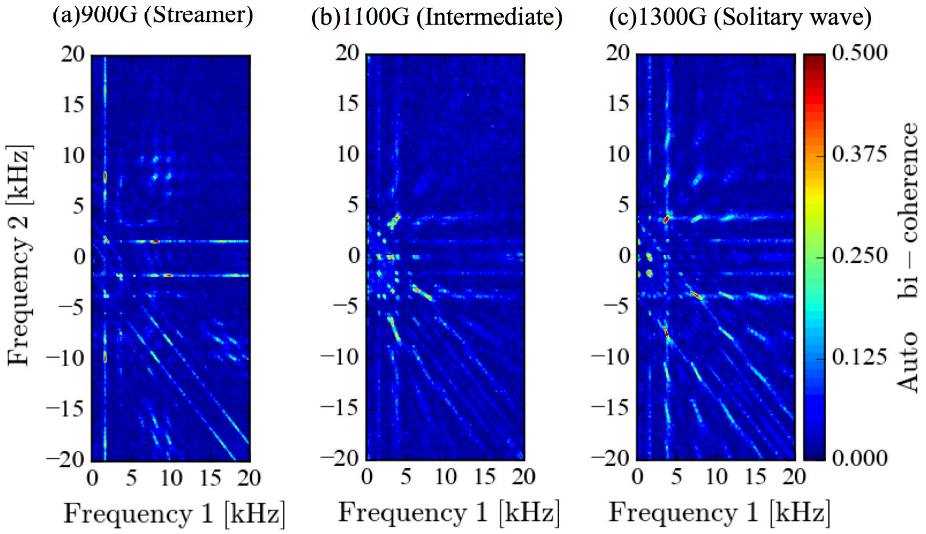

FIG. 4.4: The squared auto bi-coherence $\hat{b}(f_1, f_2)$ of ion saturation current fluctuations for (a) streamer, (b) intermediate and (c) solitary wave conditions.

The clear magnetic field dependence of the nonlinear coupling among the fluctuations are seen in Fig. 4.5. To represent the fluctuations status, the cross correlation of the streamer envelope and the mediator of m = -1 at r = 2.5 cm is shown in Fig. 4.5(a). The main components of nonlinear couplings of the streamer are represented as m = 2 and -1 or m = 3 and -1. On the other hand, the solitary waves are composed by the coupling between m = 1 and 1 or m = 1 and 2. These couplings of fluctuations are summed in frequency space, shown in Fig. 4.5(b). The figure indicates that the nonlinear couplings dramatically change with the magnetic field, and the fluctuations status changes.

In short summary, the streamer exist with the long radial correlation length in the magnetic field range around 0.7-0.10 T. The fluctuation status nonlinearly changes by magnetic field increase, i.e. from streamer region to intermediate states and finally to solitary wave region. It is suggested that the nonlinear status of drift waves are sensitively changes with magnetic field or Larmor radius. This indicates that the magnetic field strength is one of the control parameter to change the nonlinear status of drift waves, which is essential for study on the transport.

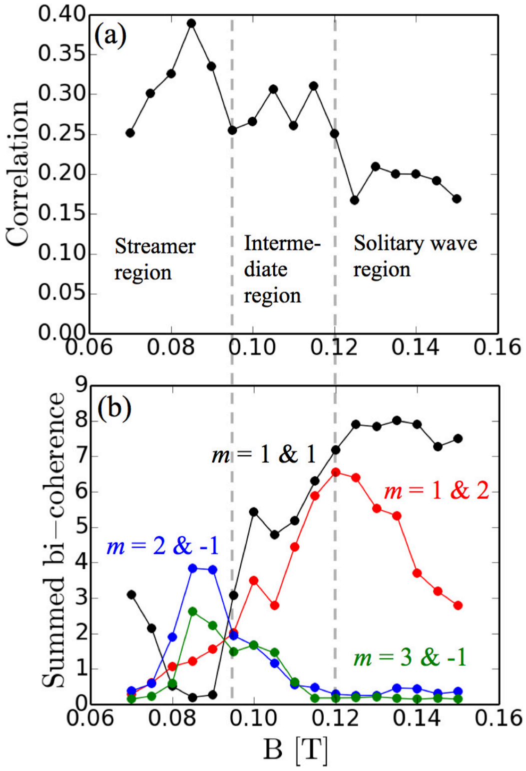

FIG. 4.5: (a) Correlation coefficient between the envelope and the mediator at r = 2.5 cm. (b) Dependence of the summed squared bi-coherence on the magnetic field.

4.2 Nonlinear waves of streamer

The previous works [44] have confirmed that the streamer and the mediator could correspond to the fast mode and the slow mode, respectively, which were predicted by a theoretical work based on Hasegawa-Mima equation [41]. Thus, theoretically, the streamer and mediator could be described in nonlinear Schrodinger equation, which is known as general equation of nonlinear waves. However, to date, the mediator has been treated simply as a linear wave without taking into account contribution of its higher harmonic components. Here we present the nonlinear characteristics of the mediator including the higher harmonic components by applying conditional averaging [99]. Moreover, the method to deduce the waveform of the mediator from the signal makes it possible to extract the exact waveform of envelope of the streamer, which has the same frequency as that of the mediator. The higher harmonic components of the mediator contribute to the generation of the distortion of the envelope of the streamer and their nonlinear relationship that both heights of the mediator and the envelope of the streamer increases as their localization becomes narrower, as is commonly observed for solitary waves. This chapter presents these new findings on the mediator and the streamer in a linear cylindrical plasma of PANTA.

4.2.1 Extraction of nonlinear waveforms using conditional averaging

The nonlinear waveform of the mediator can be directly extracted using conditional averaging based on phase tracking method as described in Chapter 2. Here, the raw signal is obtained from the ion saturation current measured with 64ch probe, similar to the previous experiment, since its signal-to-noise ratio is better than that of the floating potential. The conditional averaging is done by the

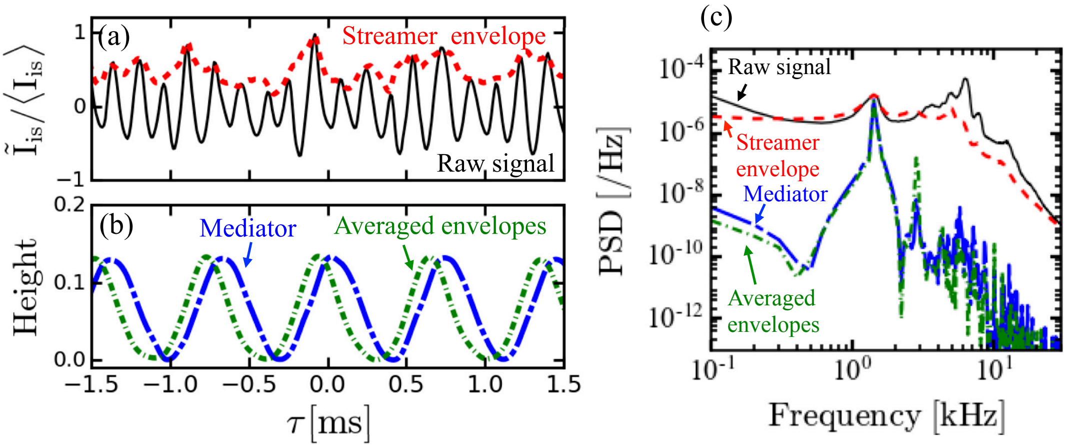

FIG. 4.6: (a) Raw signal (black solid line) and streamer envelope (red dashed line) are shown. The origin of time, $\tau = 0$ ms, indicates when the phase of the mediator is zero. (b) The waveforms of the mediator (blue dash-dashed line) and the streamer envelope (green dash-dotted line) are observed by the conditional averaging. (c) Spectra of the raw signal, the streamer envelope, the conditionally averaged mediator and the streamer envelope.

following procedure.

First, in order to extract the waveform of the mediator, phase tracking method is applied. The short time Fourier transform is performed to track the phase of its fundamental component in its temporal evolution. Here, the frequency of the fundamental component of the mediator is found to be $f = 1.4$ kHz from the power spectrum, as shown in Fig. 4.6(b). Then, conditional averaging is applied to the raw signal. The blue dash-dashed line in Fig. 4.6(b) shows the obtained (or typical) waveform of the mediator after the conditional averaging is applied on the temporal windows of the raw signals. The base level of the waveform is adjusted to zero by subtracting its minimum value, then the peak value of the wave is termed mediator height here, as described in Fig. 4.7.

Next, the streamer is obtained by subtracting the waveforms of the mediator from the raw signal. The envelope of the streamer (equivalent to the term streamer envelope in this thesis) deduced by Hilbert transform and its spectrum are shown

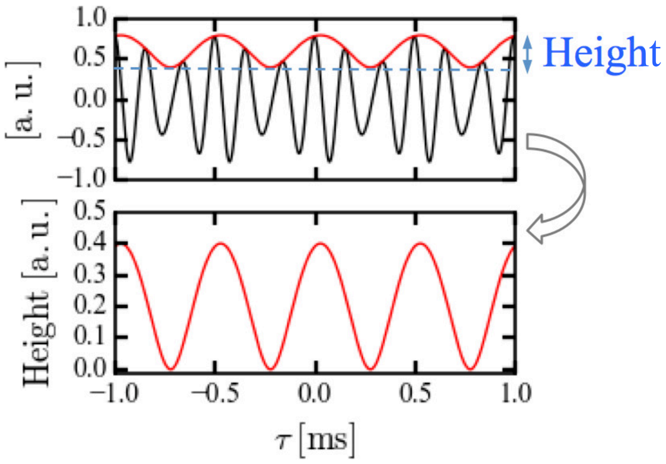

FIG. 4.7: Definition of height.

in Figs. 4.6(a) and (c), respectively. The spectrum shows that the fundamental component of the streamer envelope should also be at $f = 1.4$ kHz in accordance with the mediator. Therefore, the typical shape of the streamer envelope is also extracted by the conditional averaging on the envelopes with the same temporal windows of the mediator. The result is shown in Fig. 4.6(b) in the green dash-dotted line. For comparison, the spectra of the raw signal,the streamer envelope, the conditionally averaged mediator, and the conditionally averaged streamer envelope are shown in Fig. 4.6(c). The spectra of averaged waveforms reveal the existence of clear peaks at the second harmonic frequency at 2.8 kHz. Note that the peaks at higher harmonic frequencies are buried in the background powers of the spectra; therefore, they cannot be identified without the conditional averaging. The results demonstrate that the modulation of the drift waves to generate the streamer is not only through fundamental components of the mediator, but also through higher harmonic components of the mediator.

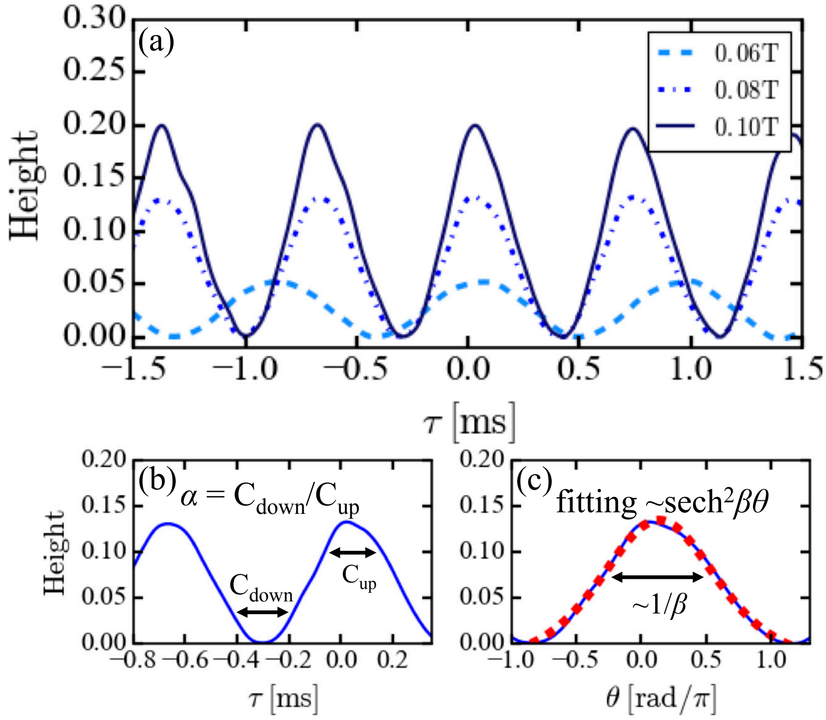

FIG. 4.8: (a) The waveforms of the mediator with the magnetic field strength of 0.06, 0.08 and 0.10 T are described. The degree of nonlinearity is estimated by two methods, deducing the (b) anharmonicity parameter, α, and (c) localization parameter, β. The waveform of the mediator at B = 0.08 T is used for the example fitting.

4.2.2 Evaluation of nonlinear characteristics of waveform

In the previous section, it shows that the nonlinear characteristics of the mediator and envelope of streamer change with the magnetic field. Figure 4.8 (a) illustrates examples of temporal evolution of the mediator under three values of magnetic field conditions B = 0.06, 0.08 and 0.10 T. The figure demonstrates that the height and the degree of localization of the mediator may increase with the magnetic field. Similar tendency can be seen for the streamer envelope.

The nonlinear characteristics of the waveform, or the degree of wave localization, can be quantified by evaluating the anharmonicity as a general method for periodic waves in the present case. The anharmonicity is defined as the ratio of

C_{down} to C_{up}, where C_{up} and C_{down} represent the full width of half maximum from the time averaged value of local maximum and that of half minimum of local minimum, respectively, as is shown in Fig. 4.8(b), and the example of its description is shown in Fig. 4.9. The anharmonicity increases as the deviation from the sinusoidal wave ($C_{down}/C_{up} = 1$) becomes larger. An example of the analysis on the mediator in Fig. 4.8(a) shows that the anharmonicity parameter α are evaluated as 0.9, 1.0 and 1.2 for B = 0.06, 0.08 and 0.10 T, respectively.

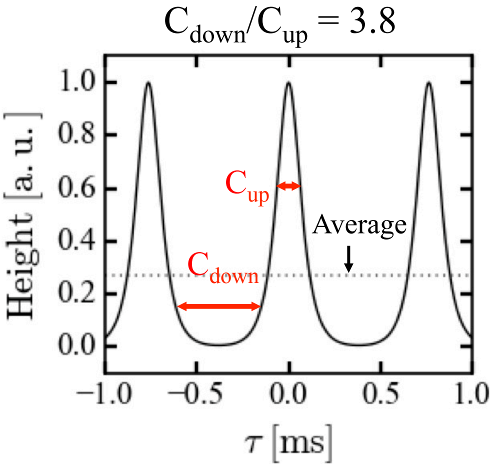

FIG. 4.9: Description of anharmonicity.

Besides, an additional method is introduced here as a support to evaluate the degree of localization of the waveform by fitting under the assumption that the structure is in the state of rigid body rotation. Thus, the azimuthal position θ is introduced by replacing time τ, as the transformation $2\pi f\tau \rightarrow \theta$, where f is the fundamental frequency of the nonlinear wave. Figure 4.8 (c) shows an example of the fitting result for the waveforms of mediator. The fitting function is $f(\theta) = y_0 + a * \mathrm{sech}^2\beta\theta$, which corresponds to the solution expected in the theory [41]. Here, y_0, a and β are the minimum value of the amplitude, the height and the localization strength, respectively. In this case, the localization width β, for the mediator of B = 0.06, 0.08 and 0.10 T are 1.50, 1.84 and 2.02, respectively. Both results, estimating α and β, indicate that the mediator should be more localized with increasing the magnetic field strength.

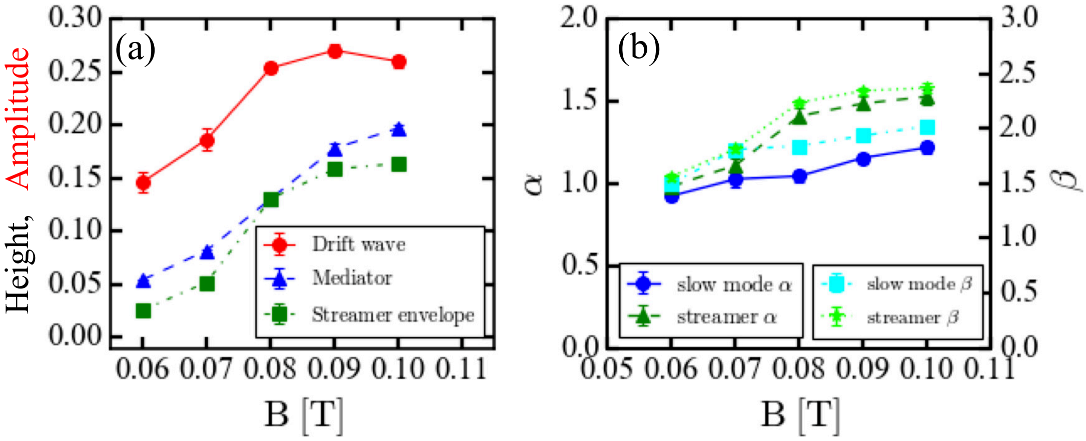

FIG. 4.10: Magnetic field dependence of (a) the height and (b) of the anharmonicity α and the localization parameter β for the mediator and the streamer envelope.

Figure 4.10 plots the height and localization parameters α and β for the mediator and the streamer envelope as a function of magnetic field. The plots show a clear dependence that the height and localization parameters increase with the magnetic field strength. It is noted that the power of the drift waves ($\sim y_0 + a/\sqrt{2}$, where y_0 and a are minimum values of the amplitude and the height) also increases with the magnetic field strength. These results indicate that both the height and localization parameters of both waves increase with the magnetic field strength.

The direct relationship between the height and localization can be evaluated as is generally investigated for the both waves. Here, the characteristic changes in the drift wave [see Fig. 4.10(a)], which reflect the background plasma conditions, are taken into account, since the resultant height of the streamer envelope is expected to increase proportionally with the drift wave and its side-band amplitudes owing to the couplings with drift waves. In order to remove the effect due to the change in the background plasma, or the change due to magnetic field strength, the heights of the waves need to be normalized by the drift wave amplitude, which

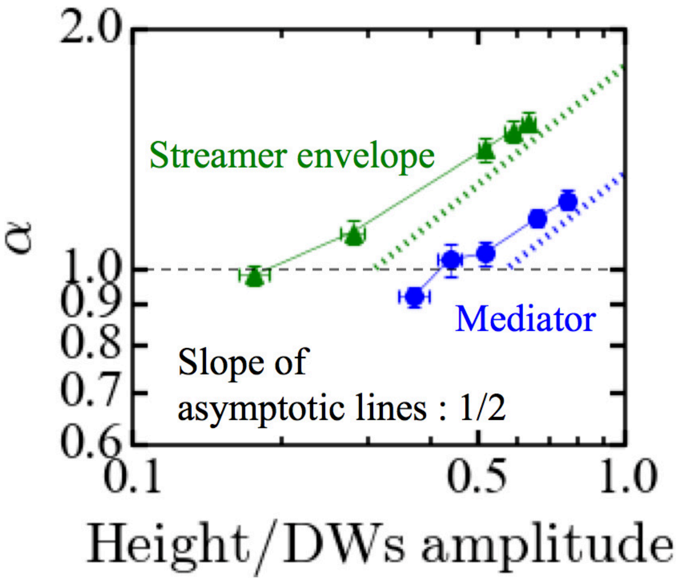

FIG. 4.11: Dependence of anharmonicity α on the normalized height is shown as a double logarithmic plot. The slope of asymptotic lines is 0.5, which indicates that height converges proportionally to α^2.

includes its side-band. Figure 4.11 shows the relationship between the height and the localization parameter, α, in a double logarithmic plot. The results show that the both normalized heights should increase, asymptotically, with the square of the localization parameter, α. The mediator and the streamer envelope have a common feature known for solitons, such as the solution of the Korteweg-de-Vries equation.

4.2.3 Discussion of nonlinear couplings

The discussion is focused on the nonlinear couplings. Here, the phase relationships among the component modes of the mediator are investigated to understand the origin of the distortion from sinusoidal wave in the mediator. For this purpose, bi-coherence analysis is adopted to investigate how the nonlinear couplings change for the mediator, as the magnetic field strength changes. Since the bi-coherence indicates the degree of phase coherency among the three waves, we can evaluate the changes in nonlinear coupling strength between the mediator and its higher harmonic components.

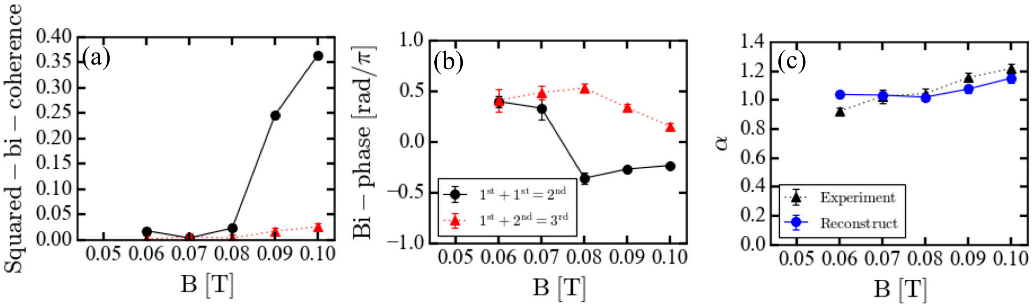

FIG. 4.12: Magnetic field dependence of the (a) squared-bi-coherence and (b) bi-phase of the components of mediator. The ensemble number is 150. Reconstruction of the mediator is performed by bi-phase analysis. The anharmonicities α of the mediator for the observed (black) and reconstructed (blue), which is performed by bi-phase analysis, are shown in (c). A good agreement with experimental observation can be seen.

Figure 4.12 (a) shows the result how the squared-bi-coherence among the fundamental mode of the mediator and its harmonic modes changes as a function of the magnetic field strength. In Fig. 4.12 (a), the black solid and red dashed lines represent the coupling among the fundamental mode and the second harmonic mode (i.e., m = -1 and m = -2), and that among the fundamental mode, second and third harmonic modes (i.e., m = -1, -2 and m = -3). The results simply demonstrate that the coupling strength increases as the magnetic field increases, or the nonlinear characteristics of the mediator become clear. Particularly, the tendency is significant for the coupling between the fundamental mode and the second harmonic mode, as shown in the black solid line in Fig. 4.12 (a).

Next, the waveform of the mediator can be reconstructed from bi-phase analysis, which provides the necessary phase relationships between the fundamental and higher harmonic modes for the reconstruction. Figure 4.12 (b) shows the bi-phase for these couplings; the bi-phase among the fundamental and second harmonic modes and that among fundamental, second and third harmonic modes are calculated. As a result, by using these phase relations and the mode amplitudes obtained from the power spectra, the waveform of the mediator can be reconstructed. Figure 4.12(c) shows the comparison between anharmonicites α obtained by reconstructions and observation. The reconstructed anharmonicity indicates a similar tendency that of observation. This suggests that the main mechanism of the nonlinear distortion of the waveform of the mediator is self-couplings of the fundamental mode to the second harmonics. It is also suggested that the distortion of the streamer envelope is generated from the higher harmonic components of the mediator and the drift waves.

In short summary, the conditional averaging is applied to extract the waveforms of the mediator, which include higher harmonic components. Due to the modulation by the higher harmonic components of the mediator, the envelopes of the streamer also contain higher harmonic components. Furthermore, the height and the localization of the both waveforms are found to increase with the magnetic field strength. The heights of the waves are found to increase with the square of localization degree, α^2, as is commonly valid for the solitary waves. Additionally, the bi-coherence analyses confirmed that the self-couplings of the fundamental mode of the mediator become strong with the magnetic field and should be the major cause of nonlinear characteristics of the mediator.

4.3 Structure of streamer and its effect on transport

Causality between radially elongated streamer structure and transport enhancement is studied in this chapter. In previous chapter, temporal waveform analysis reveal that the streamer localizes in the azimuthal direction and fluctuates in time. Thus, the discussion through using conventional method, i.e., averaged in time and space, are not efficient. Since the dynamical observation of the streamer is important, the conditional averaging is provided again in this section.

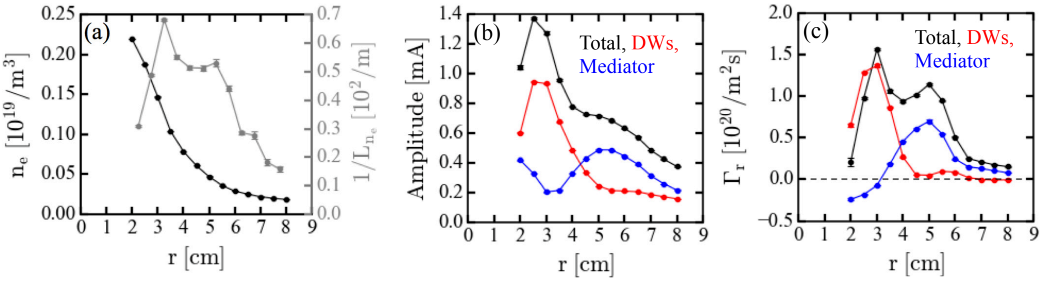

FIG. 4.13: Time averaged radial profiles of (a) electron density and inverse scale length of the density, (b) fluctuations amplitude obtained by root-mean-squared of signal and (c) fluctuation induced particle flux.

The experiment is conducted with the RS probes and 64ch probes, which are described in Chapter 2. Discharge conditions are, the magnetic field strength B = 0.09 T, argon gas pressure of 0.45 mTorr and RF power of 3 kW. The power spectrum of ion saturation current fluctuation is similar to Fig. 4.1, which corresponds to the streamer condition in PANTA.

First, time averaged radial profiles of quantities are shown in Fig. 4.13. The electron density and inverse of its scale length indicate that the strong density gradients are found at $r < 5$ cm. The fluctuation amplitude profiles reflect the radial density gradient, as shown in the Fig. 4.13(b). The amplitude is estimated as time averaged root-mean-squared of ion saturation current fluctuation. The dominant fluctuation components are the drift waves and the mediator. Those amplitudes are obtained through numerical band-pass filter. The range of band-pass filter for drift waves and mediator are $6 < f < 10$ kHz and $1 < f < 3$ kHz, respectively. Figure 4.13(b) shows that the drift waves are strong in $r < 5$ cm, which corresponds to strong density gradient region, and mediator exists in broad radial region.

The radial particle flux driven by $\tilde{E}_\theta \times B$ drift fluctuations, Γ_r is defined as, $\Gamma_r(t) = \tilde{n}_e(t)\tilde{v}_r(t) = \tilde{n}_e(t)(\tilde{E}_\theta(t))/B$, where $\tilde{n}_e$ and $\tilde{E}_\theta$ represent electron density

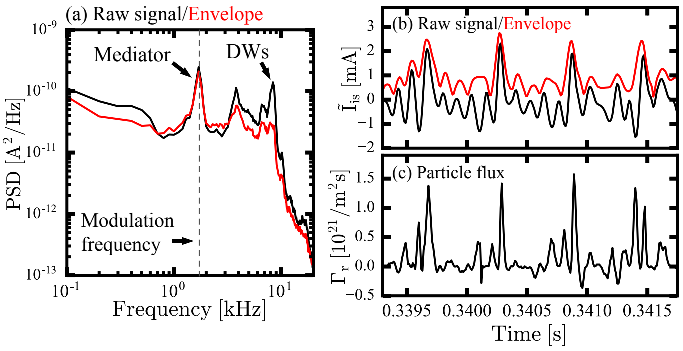

FIG. 4.14: (a) Power spectra of ion saturation current fluctuations and its envelop. (b) Temporal evolution of ion saturation current fluctuations with its envelope, and (c) radial particle flux induced by fluctuations. The measurement point is $r = 4$ cm.

fluctuations and azimuthal components of electric field fluctuations, respectively. Since the electron temperature fluctuation is sufficiently small in PANTA [75], the density fluctuation and electric field fluctuation are derived from ion saturation current fluctuation and floating potential fluctuation, respectively. Figure 4.13(c) shows the time averaged particle flux profiles. Here, the positive value of Γ_r indicates outward flux. The figure shows that the total flux is outward from $2 < r < 8$ cm. The outward flux is mainly driven by the drift waves ($2 < r <$ 4cm) and the mediator ($4 < r <$ 6cm). The residual of the flux is driven by the 2nd or higher harmonics of the mediator, D'Angelo-like mode and high frequency components.

4.3.1 Conditionally averaged structure and flux patterns

As mentioned before, Figure 4.13 is not sufficient for discussing that the streamer really enhances transport or not, and the dynamical observation is necessary. Figure 4.14 show the power spectra of $\tilde{I}_{is}$ and its envelop, $|I_{is}|$, with their temporal evolutions and that of the associated particle flux, $\Gamma_r(t)$. In the spectrum of $\tilde{I}_{is}$, a peak at 1.7 kHz and rather broad-band fluctuations from 6 to 10 kHz reflect the existence of the mediator and the DWs, respectively [45]. The existence of a peak at the same frequency of 1.7 kHz in the spectrum of the envelop, $|I_{is}|$, shows the amplitude modulation of fluctuations due to the mediator. Figure 4.14(b) shows the temporal evolution of streamers *i.e.*, quasi-periodic events of sudden increases of fluctuations in $\tilde{I}_{is}$ and $|I_{is}|$. Note that the envelope is calculated by the Hilbert transform. On the other hand, Fig. 4.14(c) shows the temporal evolution of fluctuation-driven particle flux, in which the periodic increases should be synchronized with the envelope of streamer, $|I_{is}|$. Therefore, the outward flux should be, as is expected in theories and simulations, driven by the formation of streamers.

In the case of PANTA, the streamer is observed as a quasi-periodic phenomenon, thus, the conditional averaging technique can be used to study the typical behavior of streamer and its associated flux. Since the phase of streamer is controlled with the mediator, a typical temporal evolution should be extracted with a conditional average with using the mediator period as a clock. Here, the fixed probe at $r = 4$ cm and $\theta = 90°$, which has axial distance of 225 mm from the RS probe array, is used as a reference signal to evaluate the phase of the mediator [99].

Figure 4.15 shows the conditionally-averaged temporal evolution of the fluctuation part of $|I_{is}|$, or strength of amplitude modulation, and the associated particle flux with their snap shots. In Fig. 4.15(a), the shape of the streamer is expressed in the fluctuation part of the envelop, $\widetilde{|I_{is}|} = |I_{is}| - \langle |I_{is}| \rangle$, where <> denotes temporal average. On the other hand, Fig. 4.15(b) and (c) show the averaged value and shape of the streamer-driven fluxes. It is obvious that both envelop and adjoint particle flux are radially elongated, and localized in a short duration, $\sim 2/5$ for a cycle period of the streamer emergence. Figure 4.15(b) shows time averaged (solid) and maximum value (dotted) of flux profiles. The comparison shows that the instantaneous maximum flux should be 1.5-2.5 times larger than the time averaged one.

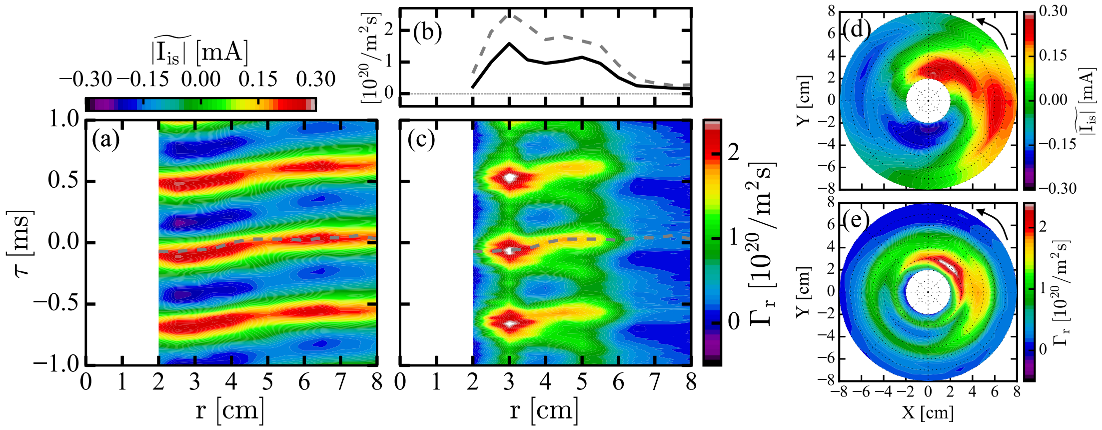

FIG. 4.15: ((a) The fluctuation part of the conditionally-averaged envelop $|\widetilde{I_{is}}|$, (b) temporally-averaged flux profiles (solid) with temporally maximum value of flux (dotted), and (c) the conditionally-averaged total particle flux. (d) The reconstructed cross section image of the envelop, and (e) that the particle flux. The gray dotted lines in (a) and (c) show the time at maximum value of the fluxes.

The periodic appearance of the almost same patterns should be regarded as that the streamers should rotate with keeping its shape almost constant over the entire radial extent. Then, assuming the rigid body rotation of the streamers, the 2D snap shots of the streamers and the associated flux shape, $f(r, \theta, \tau = 0)$, can be obtained using the relationship $f(r, \theta, \tau) = f(r, \theta_0, \tau - \Delta\theta/\omega)$, where θ_0 and ω represent the azimuthal position of the RS probe and angular frequency of streamer, and $\Delta\theta = (\theta_0 - \theta)$ are the azimuthal distance to the position to estimate. The reconstructed images demonstrate the feature that the streamer-driven flux should be radially elongated and azimuthal localized as well as the streamers. The cooperative works of DWs and mediators result in not only the azimuthal localization, but also in its radially elongated shape to cause the ballistic transport.

4.3.2 Decomposition of flux patterns

It is worth a while to decompose the streamer-driven particle fluxes to the contributions of each mode along the following formula,

$$
\begin{aligned}
\langle \Gamma_r(t) \rangle &= \left\langle \sum_{\omega_1} n_e(\omega_1, t) \sum_{\omega_2} v_r(\omega_2, t) \right\rangle \\
&= \left\langle \Gamma_{r,self} \right\rangle + \langle \Gamma_{r,crs} \rangle \\
&= \sum_{\omega} \langle n_e(\omega, t) v_r(\omega, t) \rangle + \sum_{\omega_1 \neq \omega_2} \langle n_e(\omega_1, t) v_r(\omega_2, t) \rangle ,
\end{aligned}
$$

where $\langle\rangle$ means the conditional average, and the first and second terms represent the elemental mode contributions of streamers, and the interactive ones that give no finite value in the temporal average, respectively.

Figures 4.16(a-d) show the elemental mode contributions of DWs and the fundamental mode of the mediator to the streamer-driven particle flux. Here, the contributions of DWs and (fundamental) mediator-driven fluxes are calculated as the conditional averages of the band-pass filtered signals for the frequency range of f = 6-10 kHz and 1-3 kHz for DWs and mediator, respectively. As is shown in the figures, the most of the particle flux is driven by DWs in the central region (r = 2-4 cm), while it is driven by the mediator in the outer region (r = 4-6 cm). In addition, the DW-driven flux is found to be modulated at the mediator frequency, while the mediator-driven flux shows the second harmonic oscillations, which comes from the product of density and electric field fluctuations of the mediator.

Figs. 4.16(e) and (f) show the total contributions of the elemental modes, and the interactive contributions to the streamer-driven particle flux. From the figures, the total contributions of elemental modes should produce two straight lines toward the edge, corresponding to the modulations in the contribution of the

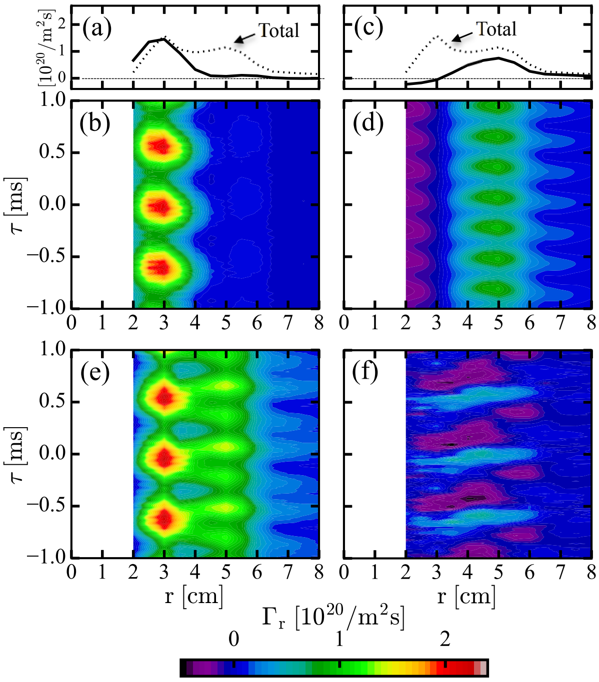

FIG. 4.16: (a) Temporally-averaged and (b) conditionally-averaged contribution of drift waves ($6 < f < 10$ kHz) to the conditionally averaged particle flux, and (c) (d) those of mediator ($1 < f < 3$ kHz). The temporally averaged total flux is shown in the dashed lines in (a) and (c). (e) Conditionally averaged total contributions of elemental modes, and (f) the interactive contribution whose temporal average is zero.

fundamental mode of mediator, although it almost could reproduce the observed streamer-driven particle flux. In contrast, the interactive contributions is found to strengthen the first lines of the particle flux (propagating from the core to edge) and weaken the second line (propagating from the edge to core), and to work to create the observed pattern of the streamer-driven particle fluxes. It is confirmed that the second harmonic of the mediator should be a dominant contributor to the interactive term. Finally, it is obvious that only the DWs should not be able to produce the radially elongated shape of the particle flux, but the cooperative works of DWs, the mediator and higher harmonic contributions can create the ballistic

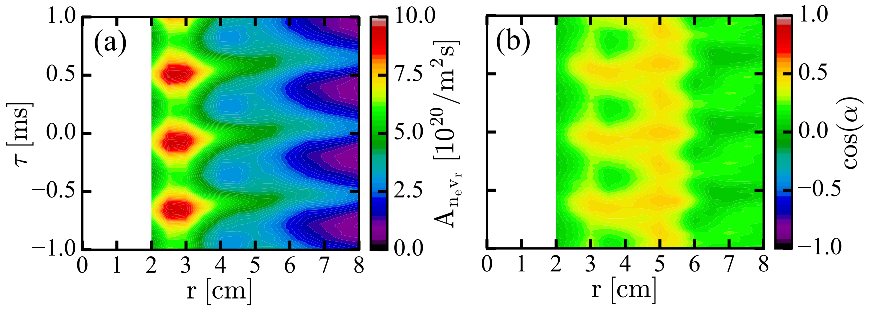

FIG. 4.17: (a) Conditionally averaged product of envelop of density and radial velocity fluctuations, and (b) the contribution of the phase difference between density and radial velocity fluctuations.

nature of the streamer and its transport.

On the other hand, Figs. 4.16(a) and (b) show another aspect, the contributions of the fluctuation amplitude and the phase difference to the streamer-driven particle flux. By using the Hilbert transform, the particle flux can be calculated as, $\Gamma_r(t) = n_e(t)v_r(t) = |n_e(t)||v_r(t)|\cos(\omega(t)t)\cos(\omega(t)t+\alpha(t)) = 0.5A_{n_e v_r}(t)[\cos(2\omega(t)t+\alpha(t)) + \cos(\alpha(t))]$, where $\omega(t)$, $\alpha(t)$ and $A_{n_e v_r}(t)$ represent time-dependent angular frequency, phase difference between n_e and v_r and the product of envelope of n_e and v_r, respectively. It is noted that the first term including the fast-varying phase, $(2\omega(t)t + \alpha(t))$, dose not contribute to the conditional average, while the second term that slowly varies should be the main contributor of the phase difference. Figure 4.17(a) and (b) shows the total conditionally-averaged envelop, $A_{n_e v_r}(t)$, and the contribution of the phase difference, $\cos(\alpha(t))$. The product of the amplitude is modulated at the fundamental frequency over the entire region, although the second harmonic modulation in the phase term becomes clearer toward the plasma edge, corresponding to the above-mentioned characteristics of the mediator [99]. Therefore, the straight line of the streamer-driven flux is produced by the pattern of the amplitudes without the second harmonic modulation.

The strengths of modulation between in amplitude and in phase are compared.

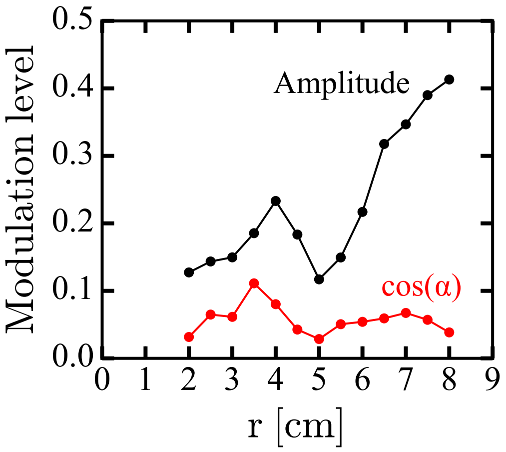

FIG. 4.18: Modulation level of amplitude and phase of particle flux. The modulation level is defined as root-mean-squared of fluctuation part of amplitude and phase, where the amplitude is normalized by its mean values.

Here, the modulation level is estimated as root-mean-squared of fluctuation parts of amplitude and cosine of phase. For comparison, fluctuations of amplitude modulation is normalized by its mean values to discuss in the dimensionless quantities. Figure 4.18 indicates that the amplitude modulation is larger than phase modulation more than factor 2. Therefore, the amplitude modulation is again important to generate flux patterns elongation in radial direction.

4.3.3 Structure of the streamer

Next, we discuss about the streamer structure, which induces the radially elongated transport. As we mentioned before, envelope structure of the streamer is formed by the nonlinear couplings. Figure 4.19(b) shows the conditionally averaged wavelet bi-coherence of ion saturation current at r = 4 cm, which is correlated at the mediator frequency of f_1 = 1.7 kHz, and the vertical axis indicates the f_2. The nonlinear couplings among the mediator and drift waves, which are around $f \sim 8$ kHz, are changes in time. Frequency summed bi-coherence, expressed as $\Sigma\hat{b}^2$, changes with in phase with streamer envelope, as is shown in

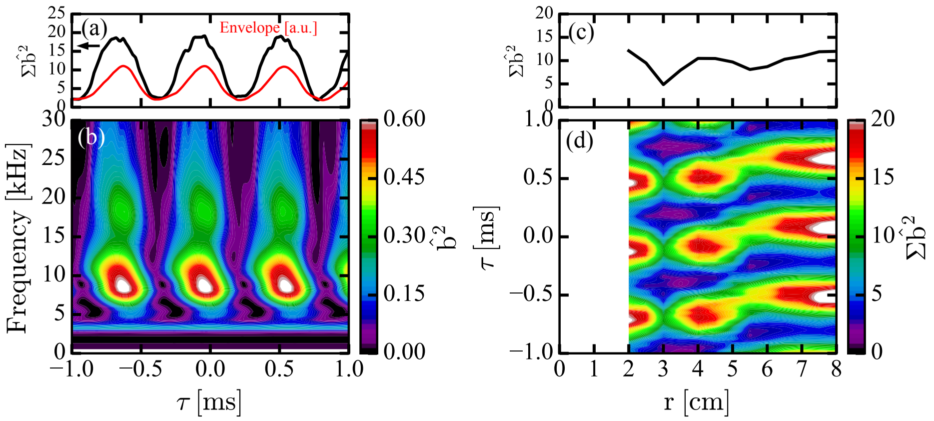

FIG. 4.19: Conditionally averaged wavelet bi-coherence at r = 4 cm is shown in (b). The vertical axis indicates f_2, and f_1 = 1.7 kHz. (a) Time evolution of summed bi-coherence (black) and the conditionally averaged envelope at r = 4 cm (arbitrary unit, red) are plotted. (d) Radial structure of conditionally averaged summed bi-coherence and (c) its time average.

the red line in Fig. 4.19(a). Therefore, the envelope structure is created by the nonlinear couplings.

The time evolution of radial changes of total bi-coherence are shown in Fig. 4.19(c) and (d). Similar to the streamer envelope, which is represented in Fig. 4.15(a), the total bi-coherence is also radially distributed. It is also confirmed that the radial structure of the streamer increase when the total bi-coherence increase.

In addition to the radial distribution of nonlinear couplings, radial convective flow of the streamer is also observed. Figure 4.20 show the fluctuation of radial $E\times B$ velocity for (a) total and (b) drift wave components, respectively. Since fluctuations of drift waves disappears after the conditional averaging of the mediator period, drift wave components are obtained by using trigger of drift waves period of f = 8.6 kHz. Compared to the drift wave components inducing fluctuations, in case of streamer, the fluctuation is radially elongated. This result is consistent with various simulation results of streamer [33, 40]. The generation of the large radial convection is the reason to enhance the radial transport.

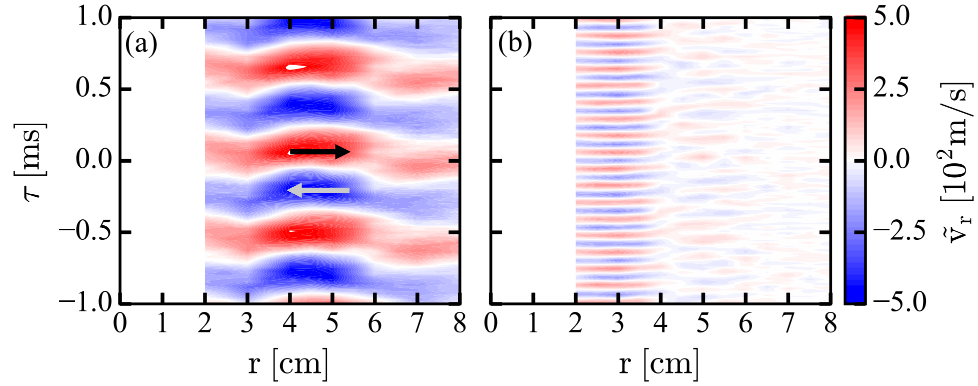

FIG. 4.20: Conditionally averaged radial velocity fluctuations, which are obtained by triggering (a) mediator (or streamer) frequency f = 1.7 kHz and (b) drift wave frequency f = 8.6 k Hz.

4.3.4 Discussions

So far we discuss the typical temporal evolution of streamers and associated particle fluxes. However, each streamer event is slightly different from each other. It is interesting how much degree the streamer-driven fluxes can be deviated from the standard value. Figure 4.21(a) shows the probability density function (PDF), $\rho(\Gamma_r)$, of the maximum value of streamer-driven fluxes for the radial position at r = 4-6 cm. The PDF shows that a finite value should still remain in the region of larger value more than a few standard deviation σ; for comparison, a Gaussian distribution for reference is also plotted. Supposed that the tail of PDF should obey the power law, $\rho(\Gamma_r) \propto \Gamma_r^{-\beta}$, as shown in Fig. 4.21(b), the most probable exponent is found to be $\beta = -4.7 \pm 0.2$ when the fitting is performed for the region of more than 2σ.

Besides, one of the most important characteristics of the streamer-driven flux is its ballistic nature of the transport. From the result in Fig. 4.15(c), it should take ~ 0.1 ms for the streamer pulse to reach from r = 2 cm to r = 6 cm. On the other hand, the diffusive time scale governed by DWs is estimated as, $\tau \sim a^2/D \sim 3$ ms, where radial distance a = 4 cm, diffusion coefficient $D \sim \omega^*/k_\perp^2$, DWs frequency

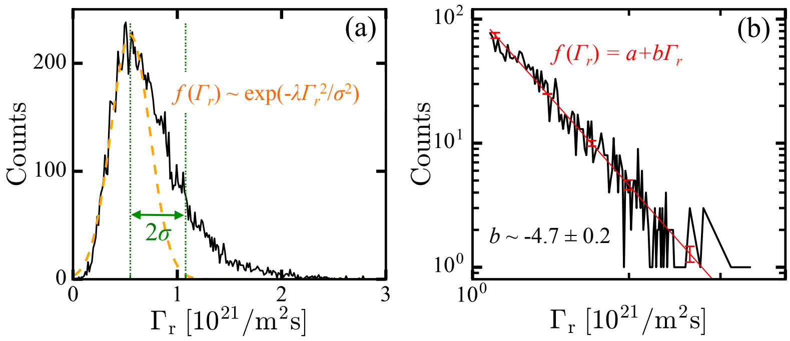

FIG. 4.21: (a) Probability density function (PDF) of maximum particle flux at r = 4-6 cm and a Gaussian (orange) distribution for reference. (b) A logarithmic plot of PDF, in the region of more than 2σ. A linear fit (red) is provided to deduce the slope.

$\omega^* \sim 2\pi \times 8$ kHz and perpendicular wavenumber $k_\perp \sim 2\pi \times 0.5$ cm^{-1} are assumed. The comparison indicates that propagation speed of flux associated with streamer is more than 30 times faster than the diffusive time scale of DWs.

It is also important to evaluate how the particles ejected from the magnetic field under steamers. Assuming that the particle should move along the trajectory of $E \times B$-drift associated with the streamer structure, the RM probe measurement gives a rough value of 2 km/s. Thus, the radial particle ejection frequency is estimated around $|E_\theta \times B|/a \sim 50$ kHz. On the other hand, the rotation frequency of the streamer is $\omega \sim 10$ kHz (f = 1.7kHz), since it is the same as the mediator frequency. The comparison between these two frequencies, the particle (and heat) should be transported to the plasma edge before the azimuthal location of the streamer does not show significant changes.

Therefore, these considerations demonstrate that streamer could make particle and energy transport instantaneously to connect the plasma core to the edge. Moreover, it has been known, in PANTA, that the azimuthal width of the streamer should become narrower with the amplitude increase [99]. If this might be valid for the streamer in toroidal plasma, a large amount of particle and heat in the confinement regime could be directly driven to the narrower region of the plasma periphery, as the streamers with larger amplitude emerge.

In short summary, the streamer-driven particle flux is evaluated experimentally in a linear cylindrical plasma, PANTA. The results show fundamental aspects of streamers and associated particle fluxes, that is, their shapes, the mechanisms to create the radially elongated structure, the individual contributions of drift waves and mediators to the transport, and the frequency of the occurrence of larger streamers and transports seems to obey the power law. The radial propagation time of transport associated with streamer is one order shorter than that of DWs. The ballistic nature of the streamer-driven fluxes that connect the high temperature core and edge, and the power laws of their emergence demonstrates the significant importance of streamers and its driven transport to the magnetically confinement plasmas for fusion.

Chapter 5

Response of streamer during biasing experiment

Previous chapter shows that the streamer forms a radially elongated structure and hence increase the radial transport. Thus, contorol of the streamer is important for plasma confinement. In PANTA, end-plate biasing experiments have been performed to observe the streamer response against electric field biasing. The privious experiments indicated that the streamer was regulated during the biasing [111], however, their suppression mechanism, nonlinear structure and transport changes are not clarified. In this chapter, experimental observations of the end-plate biasing feature and its effect on the instabilities, nonlinear structure of the streamer and associated particle transport are discussed. Main of these results are published in Ref. [103, 104].

5.1 The effect of end-plate biasing in PANTA

The biasing experiment has been performed in various experimental devices, tokamaks [105, 106], helical machines [107, 108] and linear cylindrical devices

[56, 109]. The electrode biasing is one of the techniques to control plasma turbulence through change of electric current and electric field. It is well known that the radial electric field shear generates shear flows, which cause the turbulence suppressions [110]. In this section, the effect of the end-plate biasing experiment on PANTA plasma is mentioned. Changes of two type of instabilities which forms streamer, drift waves and flute type mediator mode, are observed during the biasing.

5.1.1 Description of end-plate biasing experiment

A disk-shaped end-plate is installed at the end of the vacuum vessel, as shown in Fig. 5.1. The diameter of the end-plate is 50 mm and is located at $z = 3950$ mm. The end-plate is biased against the grounded vacuum chamber. The power supply has the maximum output power of 1500 W up to 100 V output voltage and up to 15 A output current.

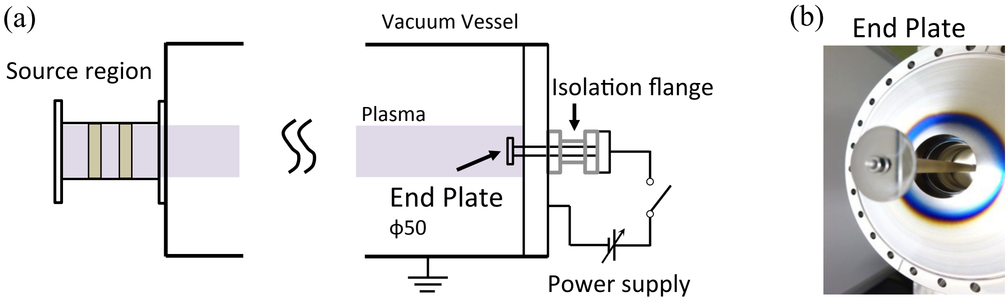

FIG. 5.1: Configuration of end-plate biasing experiment in PANTA. (a) Circuit of the biasing experiment. (b) Picture of the end-plate.

5.1.2 Discharge configuration

For investigating the effect of the biasing on the plasma, various plasma conditions are tested. Here, high RF power discharges at 6 kW are introduced in the experiment. The magnetic field strength and the neutral gas pressure are the same as those at the previous streamer discharges, as B = 0.09 T and 0.45 mTorr, respectively. The drift waves and an m = -1 of flute type mode, which is similar to the mediator, are observed in the 6 kW discharge. In this experiment, a number of the RS probes are aligned in the axial direction to investigate axial profiles of the electron density and floating potential. For instance, one is located at z = 1375 mm, in front of the 64ch probe, and the other is at z = 3885 mm, in front of the end-plate, respectively.

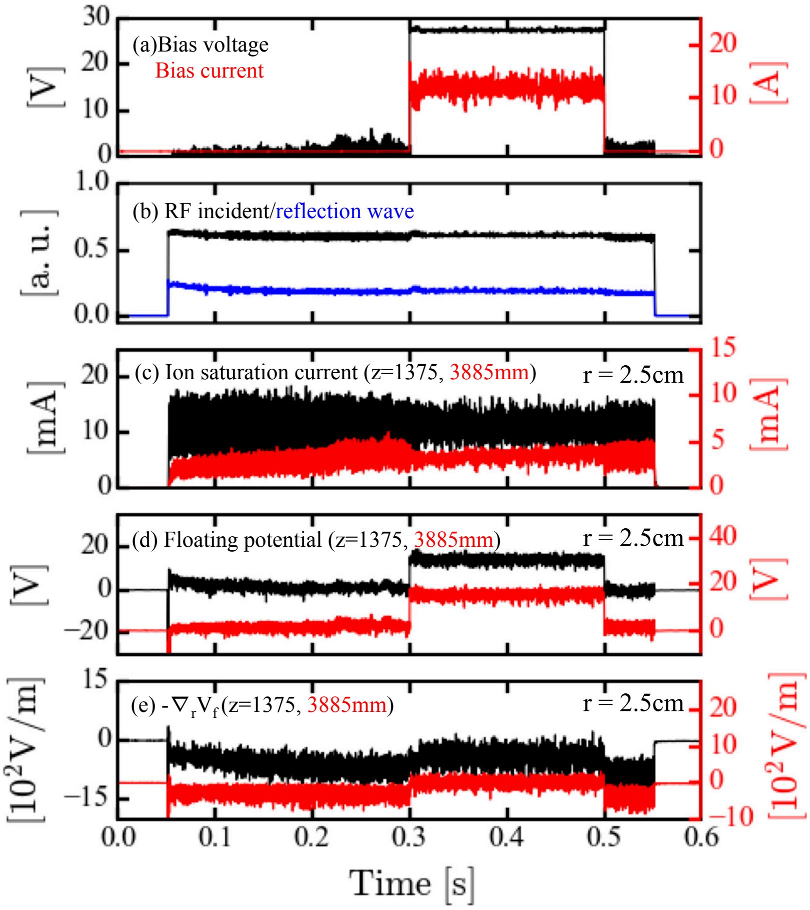

FIG. 5.2: Time evolutions of (a) biasing voltage and current and (b) RF incident and reflected waves. RS probes at different axial positions measure (c) ion saturation current, (d) floating potential, and (e) radial gradient of the floating potential, respectively.

Waveforms at a typical discharge are shown in Fig. 5.2. The biasing is applied from 0.3 s to 0.5 s. In the discharge, the positive 30 V bias is applied, and the electric current towards the end-plate is around 12 A. The RF signal shows that the net input power doesn't change during the biasing. The fluctuation level of the ion saturation current decrease at both axial positions, as shown in Fig. 5.2(c). With the biasing, the floating potential abruptly increases simultaneously in the axial direction. On the other hand, the radial gradient of the floating potential decreases with some finite time delay when the biasing starts.

5.1.3 Bias voltage dependence of profiles

For investigating bias dependence, the bias voltage is positively changed every 2.5 V. Figure 5.3 shows the dependence of the plasma quantities at z = 1375 mm, except the bias current (measured at the end-plate, z = 3950 mm). The bias current and floating potential increase gradually with the bias voltage. On the other hand, in the central region inside the end-plate radius $r < 2.5$ cm, the ion saturation current and inverse scale length of the electron density start to increase at around 20 V and saturate at around 30 V. In spite of the increase of the density gradient, the radial derivative of the floating potential starts to decrease at around 20 V.

The radial profiles at 0, 20 and 30 V biasing are shown in Figs. 5.4. They indicate that the electron density gradient in the central region ($r < 3$ cm) increase with the biasing voltage. However, the electron temperature dose not change with the biasing voltage. Thus, change in the profiles of the floating potential almost reflect change in the plasma potential by the biasing.

From above discussion, the change of radial gradient of the floating potential reflects the change of radial electric field. Figure 5.5(a) shows that the gradient of the floating potential and its shear at around r = 2.5 cm decrease with the biasing. On the other hand, the relative fluctuation levels, which are obtained from root-

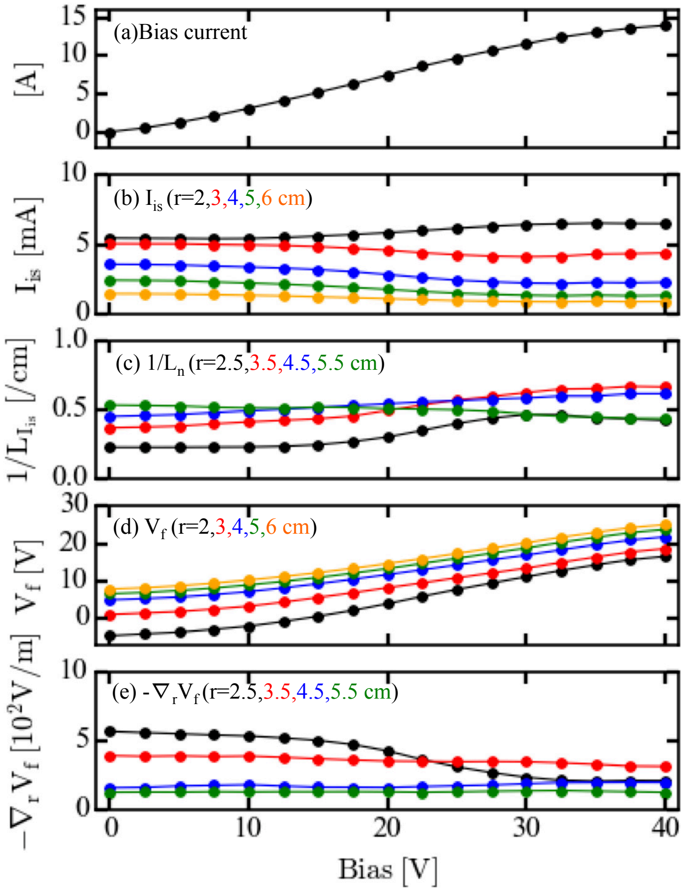

FIG. 5.3: Bias voltage dependence of (a) bias current, (b) ion saturation current, (c) inverse scale length of density profile, (d) floating potential and (e) radial derivative of the floating potential, respectively. The measurement axial position of the quantities (b)-(e) is at z = 1375 mm.

mean-squared of the ion saturation current fluctuations, decrease at around r = 2.5 cm. This is not consistent with the physics of electric field shear suppression [110]. However, since the fluctuations have large axial correlations, the variation of the electric field in the different axial position may affect the suppression of fluctuations. Figure 5.5(b) shows the gradient of the floating potential measured at z = 3885 mm. The strong radial electric field shear at around r = 2.5 cm is induced by the biasing. This radial electric field near the edge of the end-plate may reduce the fluctuations level in the whole region. The end-plate biasing changes

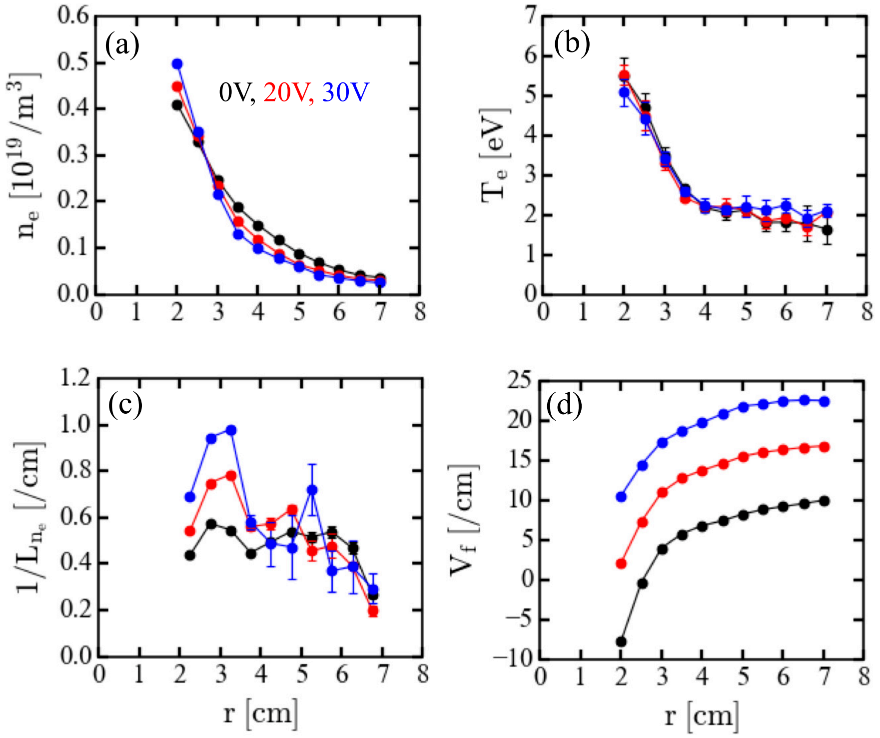

FIG. 5.4: Profiles of (a) electron density, (b) electron temperature, (c) inverse scale length of electron density and (d) floating potential are shown. The measurement position is at z = 1375 mm.

the profiles of electric field in three-dimensional space, and that changes influence the plasma, or fluctuations.

5.1.4 Fluctuations changes with biasing

In this plasma conditions, similar to the streamer discharge, the drift waves and flute type mode coexist. Since the flute mode has an m = -1 and k_z = 0, it is quite similar to the mediator in the streamer discharge. Thus, the changes of these fluctuations against bias voltage is key for the streamer suppressions.

The bias voltage dependence of the amplitude of drift waves is measured, as shown in Fig. 5.6(a). The drift waves decrease around 15 V, and saturate at 30 V. The dependence is similar with those of density gradient and radial electric field.

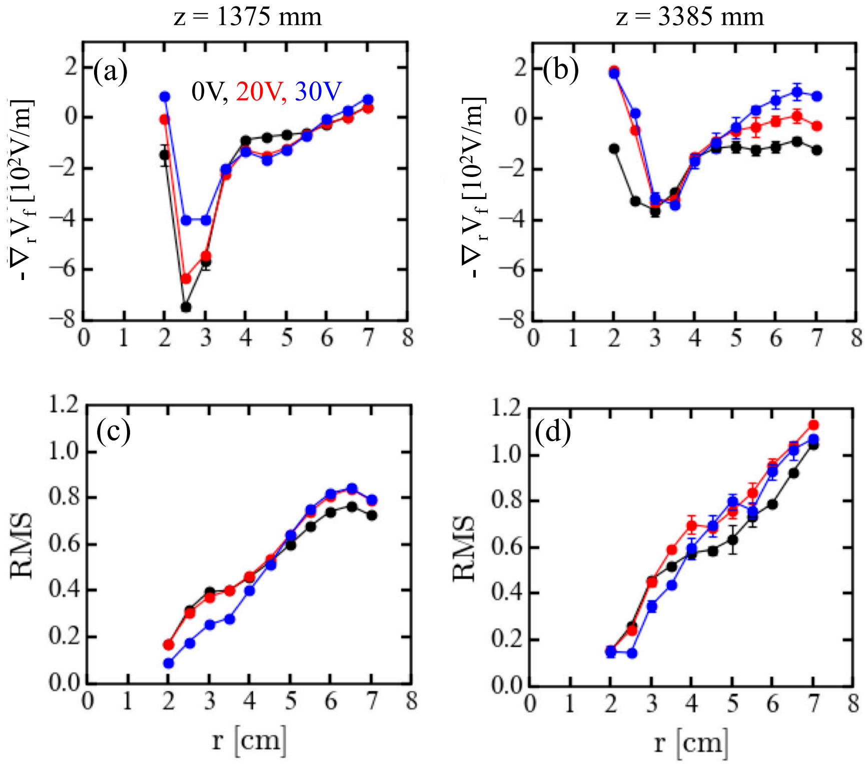

FIG. 5.5: Profiles of the radial gradient of floating potential at (a) z = 1375 mm and (b) z = 3885 mm. Fluctuation levels at (c) z = 1375 mm and (d) z = 3885 mm are also shown.

On the other hand, the amplitude of flute mode increases with the bias voltage. Therefore, the flute mode behaivior is correlated with the radial electric fields, e.g. Kelvin-Helmholtz type instabilities [64].

In short summary, the end-plate biasing in PATNA, the radial electric field changes only near the end-plate region. Since the drift waves have long axial wavelength and correlation, the radial electric field shear at the end-plate region may suppress the drift waves in the whole plasma region. The reduction of the drift waves may link the increase of the density gradient. On the other hand, the amplitude of the mediator like flute mode increase with the biasing, thus, this mode is correlated with the electric field shear driven instabilities. The changes of electric field in three-dimensional space could affect to the fluctuations, and thus

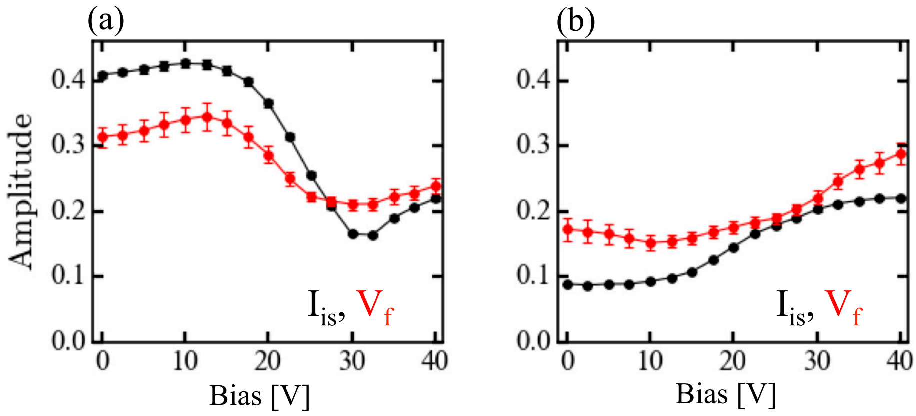

FIG. 5.6: Amplitudes of normalized ion saturation current fluctuation and floating potential fluctuation for (a) drift waves and (b) flute mode measured with the 64ch probe. The measurement location is at r = 4 cm and z = 1885 mm.

to the streamer.

5.2 The change of nonlinear structures

The end-plate biasing experiment on the streamer discharge is performed. During the biasing, bunching structure of the streamer is destroyed [111]. This is the same mechanism of the previous experiment that the strong radial electric field is generated near the end-plate, and the shear may suppresses the whole region of fluctuations [111]. Here, the changes of nonlinear structures of the streamer are discussed for studying the suppression mechanism of the streamer.

5.2.1 The discharge condition and profiles

Similar to the previous section, the end-plate biasing on the streamer discharge is conducted. The positive bias is applied for the period of 0.3 to 0.45 s as shown in Fig. 5.7. For the streamer discharge, when the biasing voltage reaches 50 V, the bias current takes two values and jumps from one to the other several times.

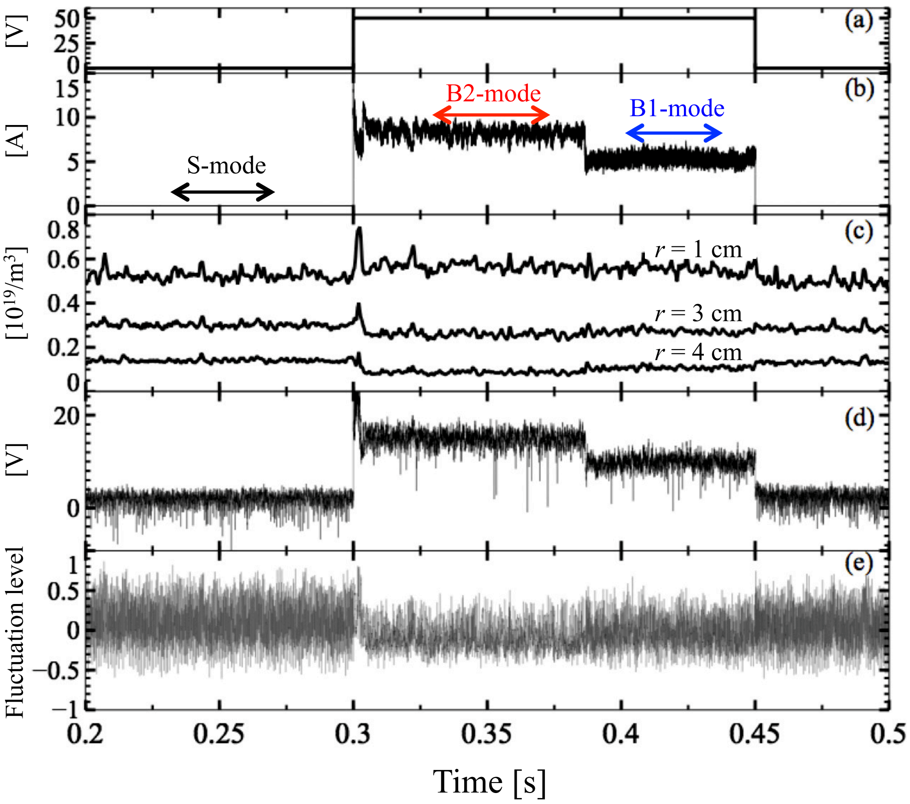

FIG. 5.7: (a) Bias voltage. (b) Bias current. Bias-less S-mode yields the streamer region. During the B2-mode, fluctuations are suppressed more than during the B1-mode. (c) Averaged electron density at three different radii (r = 10, 30 and 40 mm). (d) Floating potential measured at r = 40 mm. (e) Fluctuation component of ion saturation current at r = 30 mm.

The current jump is an indicator of the transition. Figure 5.7(b) shows a case of one current jump during a single discharge. Here we define three plasma modes; the first is S-mode (Streamer mode), which appears without biasing and is characterized by the streamer state. The lower and higher bias current phases are called as B1-mode (Biased 1 mode) and B2-mode (Biased 2 mode), respectively. Figure 5.7(c) shows time-averaged electron density at r = 10, 30 and 40 mm measured with the 5ch radial probe array, which is located at z = 1375 mm. The electron density at r = 10 mm, inside the end plate region, increases in the B1-mode, and further increases in the B2-mode. On the other hand, the density at r = 40 mm, outside the end plate region, decreases. Then, the radial profile of the density is steep in the B1-mode and becomes steeper in the B2-mode. During the biasing, the floating potential also increases rapidly as shown in Fig. 5.7(d). Amplitude of the fluctuation was reduced in the B1-mode and further reduced in the B2-mode, as shown in Fig. 5.7(e).

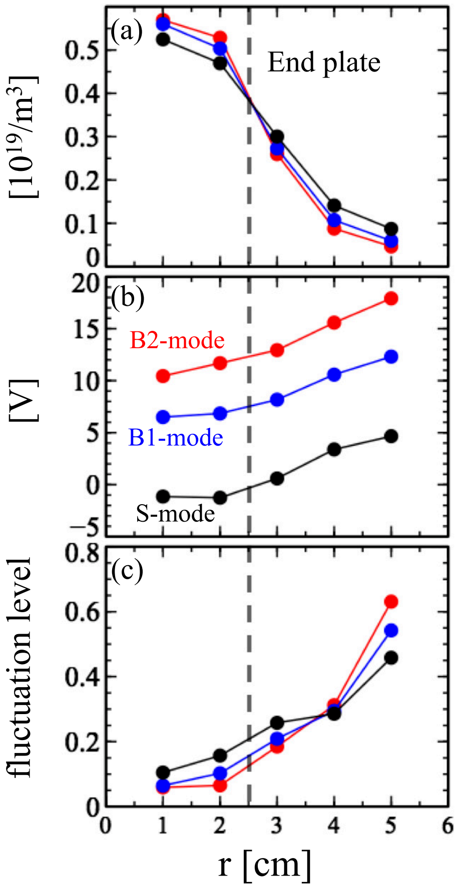

FIG. 5.8: Radial mean profiles of (a) electron density, (b) floating potential and (c) relative density fluctuation level. Black, blue and red lines indicate data in S-mode, B1-mode and B2-mode, respectively.

Time-averaged radial profiles of the electron density, floating potential and root-mean-squared fluctuation level are shown in Fig. 5.8. The profiles are obtained with the 5ch probe. Black, blue and red lines denote those in the S-mode, B1-mode and B2-mode, respectively. During the biasing, the gradient of the density profile is sharp in B1-mode and becomes sharper in B2-mode. Similar to the previous experiments, the gradient of the floating potential dosn't change, or is even weaker during the biasing. On the contrary, the gradient of the floating potential near the end-plate increases [111]. Thus, relative fluctuation levels decreases during the biasing over the whole axial positions, as shown in Fig. 5.8.

5.2.2 Changes of spectra and structure of fluctuations during biasing

Frequency-azimuthal mode decomposed Fourier analysis is applied to signals of the 64ch probe array. Figure 5.9 shows two-dimensional normalized power spectra of the ion saturation current ((a), (b) and (c)), and the floating potential ((d), (e) and (f)) fluctuations. The floating potential is normalized by the electron temperature of 3 eV, which was measured in identical plasma condtions [51]. Here, positive frequency denotes that fluctuations propagate in the electron diamagnetic drift direction. In the S-mode, the mode at (m, f) = (1, -1.5 kHz) is the mediator of the streamer, which propagates in the ion diamagnetic direction. Strong drift wave fluctuations exist as (m, f) = (2, 6.5kHz) and (3, 5kHz), which propagate in the electron diamagnetic direction.

Density fluctuations are considered during the biasing; in the B1-mode, frequency of the $m = 2$ drift wave changes from 6.5 kHz (S-mode) to 7 kHz as shown in Fig. 5.9(b). The mediator frequency also changes from -1.5 kHz (S-mode) to -2 kHz. The power of the drift wave fluctuations decreases. In contrast, the power of the mediator increases and the higher harmonics of the mediator are excited as the mode (m, f) = (2, -4.5 kHz). In the B2-mode, the frequency of the $m = 2$ drift wave changes from 6.5 kHz (S-mode) to 7.5 kHz. The mediator frequency also changes from -1.5 kHz (S-mode) to -2.5 kHz. The power of the drift wave fluctuations further decreases compared to that in the B1- mode. In addition, the

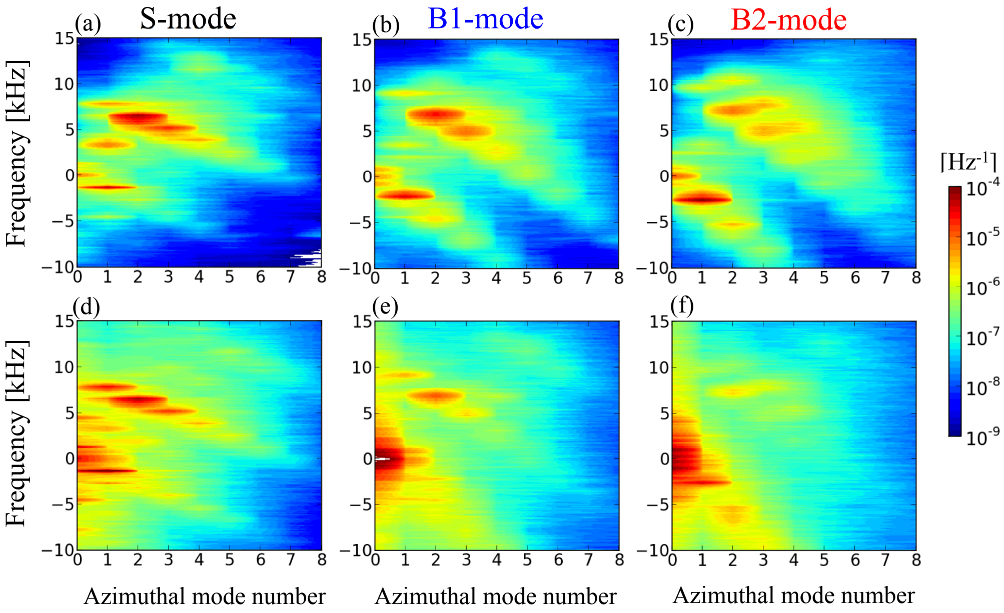

FIG. 5.9: 2-dimensional normalized power spectra of data measured with the 64ch probe array. (a), (b) and (c) indicate ion saturation current fluctuations and (d), (e) and (f) show floating potential fluctuations, respectively.

power of the mediator and its higher harmonics further increases.

The floating potential fluctuations during the biasing are considered; in the B1-mode, the mediator disappears and the power of drift waves decreases. In the B2-mode, the mediator is excited again and its higher harmonics are also excited, and the power of drift waves furtherer decreases. Increase in the power of a mode m = 0 during the biasing is not verified yet. These modes are not zonal flows, however, since the observed fluctuations oscillate radially at the same phase, and its radial wavenumber is almost 0.

In order to investigate the spatial structure of fluctuations, correlation analysis is performed. Figure 5.10 shows contours of real part of the complex cross spectra of the normalized density fluctuations between the 5ch radial probe data and the 64ch probe array data. Frequency of the m = -1 component, mediator, changes to (1.5 kHz, 2.0 kHz, 2.5 kHz) depending on the modes (S-mode, B1-

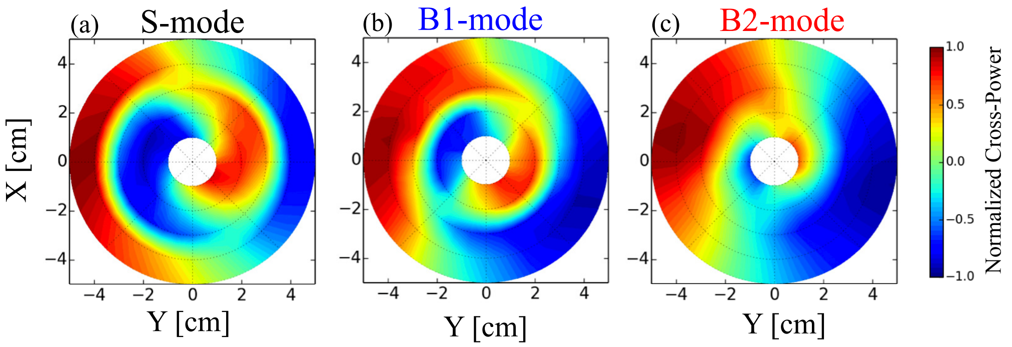

FIG. 5.10: Cross section of mediator of $m = -1$, deduced by real part of cross spectra between 5ch radial probe and 64ch probe array. Frequency components of (a) 1.5 kHz in the S-mode, (b) 2.0 kHz in the B1-mode, and (c) 2.5 kHz in the B2-mode are shown, respectively.

mode, B2-mode). A node is formed in the density fluctuation, and location of the node shrinks radially inward during the biasing. The mediator structure changes globally by the biasing.

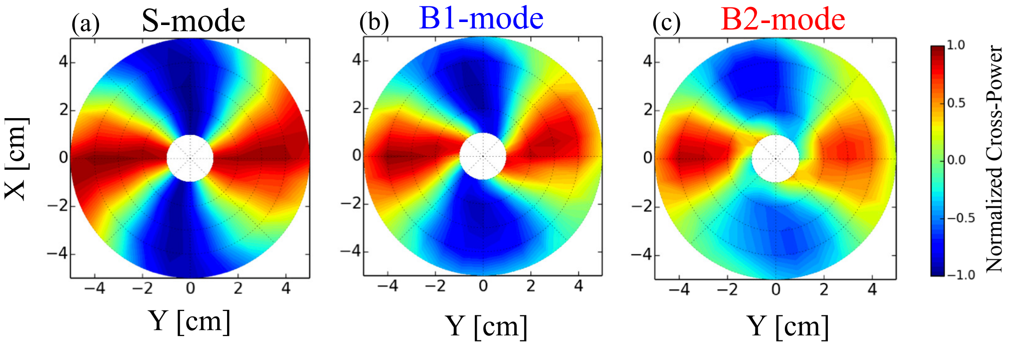

FIG. 5.11: Cross section of mediator of $m = 2$, deduced by real part of cross spectra between 5ch radial probe and 64ch probe array. Frequency components of (a) 6.5 kHz in the S-mode, (b) 7.0 kHz in the B1-mode, and (c) 7.5 kHz in the B2-mode are shown, respectively.

The drift wave cases are explained next. Figure 5.11 shows cross spectrum of the $m = 2$ component of density fluctuations in the (a) S-mode, (b) B1-mode and (c) B2-mode, respectively. The drift wave of $m = 2$ component has long radial correlation length in the S-mode. The correlation length tends to decrease in the

B1-mode, and is clearly shortened in the B2-mode. Not only the amplitude but the correlation length of the drift waves decreases by the biasing.

5.2.3 Change of nonlinear characteristics

First, to investigate the changes of the nonlinear couplings of the streamer, bi-spectrum analysis is performed. Auto-bi-coherence is obtained from 179 ensemble averaging (2 ms time window) from the 64ch probe array. To increase the number of ensemble averaging, the 32 probe signals of 64ch probe are averaged and thereby the bi-coherence is averaged over the azimuthal wave number domain.

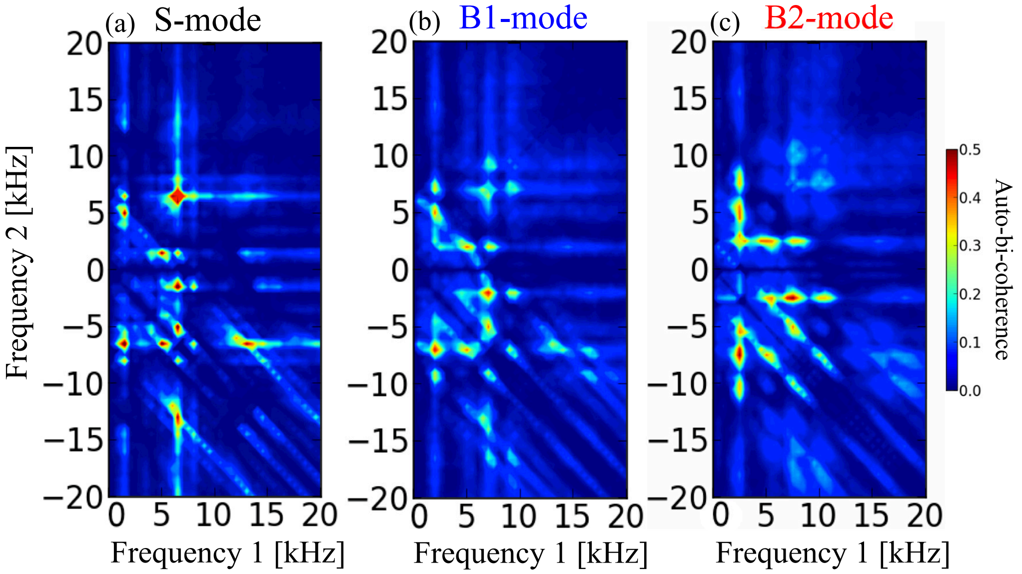

FIG. 5.12: Squared auto-bi-coherence of density fluctuations measured by 64ch probe array in (a) S-mode, (b) B1-mode and (c) B2-mode. Auto-bi-coherence changes during biasing.

Figure 5.12(a) shows the squared auto-bi-coherence of density fluctuations in the S-mode. Strong peaks are visible at $f_1 = 6.5$ kHz. These peaks mean the strong nonlinear coupling between $f_1 = 6.5$ kHz and peaked f_2 fluctuations. For example, $f_1 = 6.5$ kHz couples with $f_2 = \pm 1.5$ kHz and produces $f_3 = 5$ kHz and

8 kHz drift waves. In particular, a peak at (f_1, f_2) = (6.5 kHz, 6.5 kHz) is very strong. This suggests that the coherent mode at (m, f) = (4, 13 kHz) observed in the 2-dimensional power spectrum is exited by the self-coupling of the coherent drift wave at f = 6.5 kHz. Peaks aligned on the three lines, i.e., f_1 = 1.5 kHz, f_2 = 1.5 kHz and $f_1 + f_2$ = 1.5 kHz, indicate the nonlinear coupling with the $m = -1$ waves, i.e. the mediator.

In the B1-mode, Fig. 5.12(b) shows that the nonlinear coupling with the drift wave reduces, because peaks aligned on the lines of f_1 = 7 kHz and f_2 = 7 kHz become weak compared with those in the S-mode. In particular, the self-coupling reduces. On the other hand, the couplings with the mode at (m, f) = (-1, 2 kHz) increases compared to those in the S-mode.

Further changes appear in the B2-mode. Figure 5.12(c) indicates that the nonlinear coupling with the drift wave further reduces. The self-coupling considerably reduces. Nonlinear coupling with the mode at (m, f) = (-1, 2.5 kHz) is enhanced because peaks aligned on three lines, i.e. f_1 = 2.5 kHz, f_2 = 2.5 kHz and $f_1 + f_2$ = 2.5 kHz, become strong and broad. Especially, the self-couplings of this mode (i.e., f_1 = 2.5 kHz and f_2 = 2.5 kHz, 5.0 kHz and 7.5 kHz) are clearly shown in the B2-mode.

Although the couplings between the $m = -1$ waves and drift waves contribute the streamer formation, these self-couplings contribute not the streamer formation but the formation of the solitary structure. Unfortunately, the frequencies of the $m = 2$ drift wave and third harmonic of the $m = -1$ (7.5 kHz) overlap each other in the B2-mode, thereby it is difficult to distinguish the contributions of these two modes to nonlinear couplings at (f_1, f_2) = (2.5 kHz, 7.5 kHz). For more detailed discussion, wavenumber mode decomposition in the bi-coherence analysis is required, however, it requires large number of ensemble to obtain the converged bi-coherence. This point is discussed in the next section.

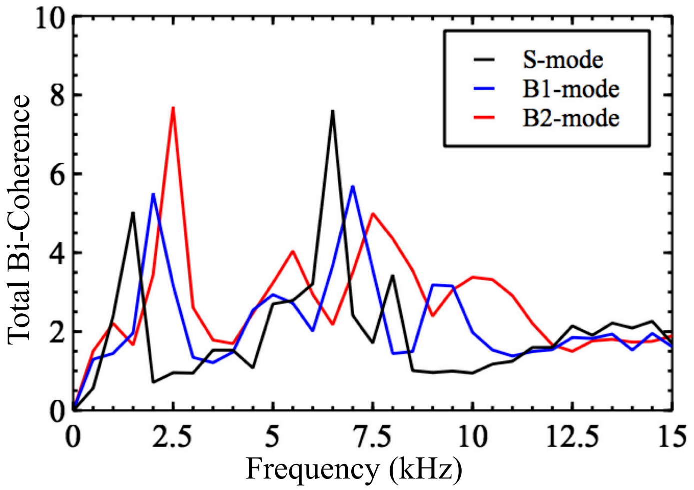

FIG. 5.13: Total bi-coherences in S-mode (black line), B1-mode (blue line) and B2-mode (red line). The nonlinear couplings of drift wave decrease, while that of $m = -1$ waves increase during the biasing.

The total bi-coherence is very useful to observe contribution of a certain mode to the nonlinear couplings with ambient modes. Figure 5.13 (a) shows that the total bi-coherence is large at $f = 6.5$ kHz in the S-mode and thus the $m = 2$ drift wave is strongly coupled with other fluctuations. With the biasing, the couplings with the $m = 2$ drift wave ($f = 7$ kHz in the B1-mode and 7.5 kHz in the B2-mode) decreases. On the other hand, the couplings of $m = -1$ waves ($f = 1.5$ kHz, 2.0 kHz and 2.5 kHz, for the S-mode, B1-mode and B2-mode, respectively) increases during the biasing. This result is consistent with the result of bi-coherence analysis.

To observe the nonlinear coupling features more directly, temporal evolutions of fluctuations are also considered. Figure 5.14 shows temporal evolution of density fluctuations. Figs. 5.14 denote mode-frequency resolved signals in the (a) S-mode, (b) B1-mode and (c) B2-mode, respectively. The upper rows denote the filtered signal in the range $f = 0.8$ - 3.0 kHz and $m = -1$ (mediator), the middle rows denote the filtered signal in the range $f = 4.8$ - 9.0 kHz and $m = 2$ and 3

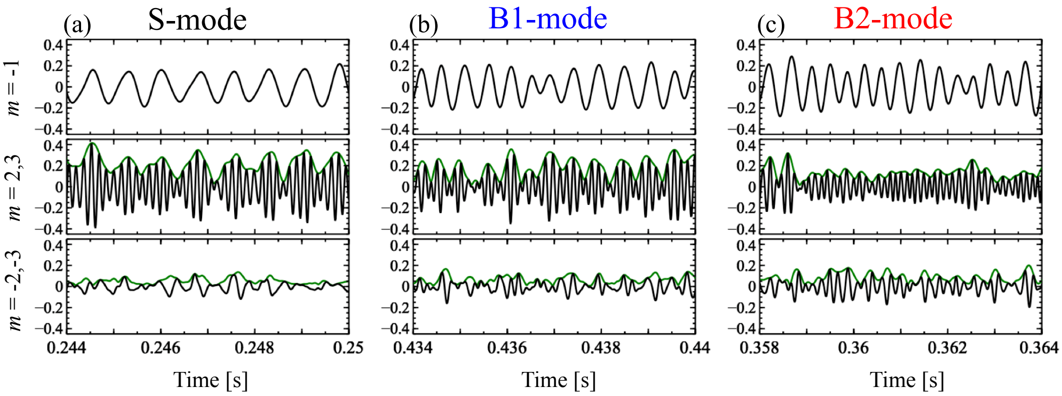

FIG. 5.14: Time evolution of density fluctuations are extracted by the spatio-temporal filter. In upper raws, fluctuations are filtered in the range f = 0.8 - 3.0 kHz and m = -1. In middle raws fluctuations are filtered in the range f = 4.8 - 9.0 kHz and m = 2, 3. In lower raws fluctuations are filtered in the range f = 1 - 8.5 kHz and m = -2, -3. Green line indicates envelope of each fluctuations.

(drift waves), and the lower rows represent the filtered signal in the range f = 1 - 8.5 kHz and m = -2 and -3 (harmonic components of mediator), respectively. Green line means envelops of fluctuations calculated by using Hilbert transform. In the S-mode, envelops of drift waves (m = 2 and 3) vary temporally and those frequencies are the same as that of the m = -1 mode. This means that the modes (m = 2 and 3) are modulated by the m = -1 mode. On the other hand, modulations of the envelops of the modes m = -2 and -3 are weak and doesn't synchronized with the m = -1 wave. Here the coupling among m = -1 and m = 2 and 3 are three-wave coupling, while coupling between m = -1 and m = -2 and -3 can be self-coupling of the m = -1 mode. Thus, three-wave couplings are dominant in the S-mode.

In the B1-mode, the $m = -1$ mode couples with the m = 2 and 3 modes, because the envelope modulation is observed. While m = -2 and -3 modes are merely couple with m = -1 mode especially for 0.438 s ~ 0.44 s.

In the B2-mode, modulations of m = 2 and 3 drift waves are small compared to those in the B1-mode, especially for 0.36 s ~ 0.364 s. The envelops of m = -2 and -3 modes, on the other hand, modulate strongly compared to those in the

B1-mode. The three-wave coupling among m = -1 mode and m = -2 and -3 modes is confirmed shown as the amplitude modulation, however, three-wave coupling between m = -1 and m = 2 and 3 modes decreases in the B2-mode compared to those in the S-mode and B1-mode.

These results suggest that the characteristics of three-wave (drift waves and mediator) couplings in the streamer disappear during the biasing. Instead, the coupling of m = -1 mode and its higher harmonics (m = -2 and -3) are excited. Next, for the confirmation, the nonlinear waveform of the mediator are extracted by the conditional averaging.

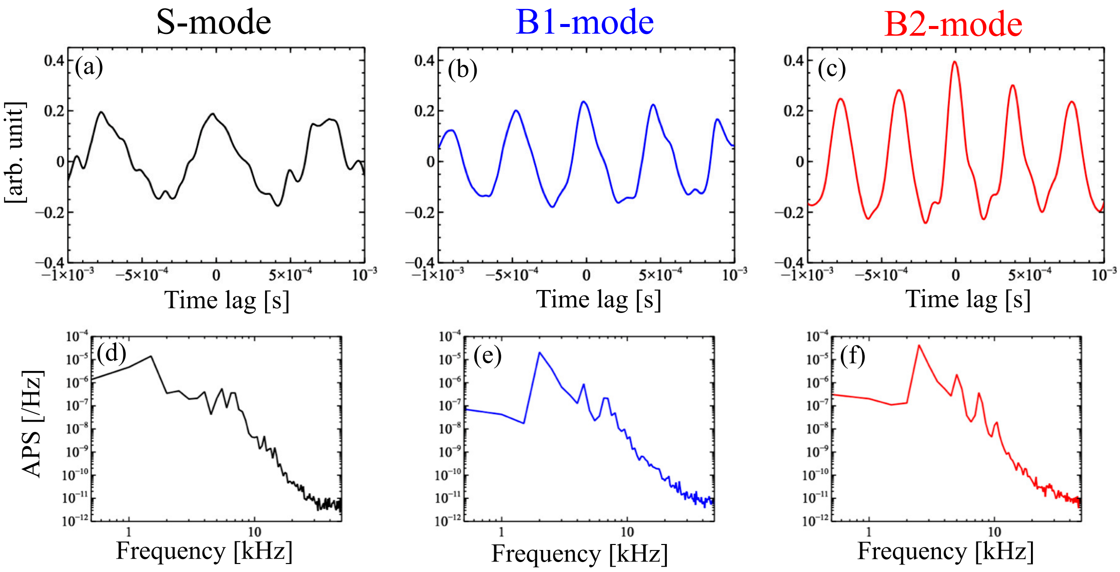

FIG. 5.15: Conditional averaging with phase tracking method is applied in (a) S-mode, at f = 1.5 kHz, (b) B1-mode, at f = 2 kHz and (c) B2-mode, at f = 2.5 kHz, respectively. Power spectra of the extracted waves are also described as (d), (e) and (f), respectively.

Here, frequency components of f = 1.5 kHz, 2.0 kHz and 2.5 kHz are used as reference tracking phase frequency in the S-mode, B1-mode and B2-mode, respectively. Conditional averaging is performed over more than 580 ensemble numbers. The extracted waveform of the mediator in the B1-mode has larger peak than that in the S-mode, and the peak additionally become larger in the B2-mode, as shown in Figs. 5.15(a)-(c).

Power spectra of the extracted waves show that there are more clear peaks of 2^{nd} and 3^{rd} harmonics of the mediator during the biasing. This suggests that the self-coupling of the $m = -1$ mode increases in the B1-mode and additionally increases in the B2-mode. The excitation of the harmonics suggests that the azimuthal localization of the mediator becomes strong during the biasing.

5.3 The change of transport

In previous section, it is explained that the nonlinear couplings between the drift waves and the mediator decreases during the biasing, and the mediator forms nonlinear waveforms strongly by their self couplings. During the biasing, due to the destruction of the streamer, the radial density gradient increases. In this chapter, the changes of particle flux associated with change in the streamer during the biasing are mentioned.

5.3.1 Frequency-mode decomposed particle flux

The total particle flux redueces during the biasing. At r = 4cm, time-averaged fluxes in the S-mode, B1-mode and B2-mode are 2.3, 2.2 and 1.7 [10^{19}/m^{2}s] , respectively. To understand fluctuation behaviours, the particle flux is decomposed into frequency-mode domain by using two-dimensional Fourier transform. In this case, the total particle flux is written as [101],

$$\Gamma_r = \frac{2}{B}\Re\left[\int_0^{\omega_{Nyq.}} d\omega \int_{-k_{Nyq.}}^{k_{Nyq.}} dk S_{\tilde{n},\tilde{E}}(k,\omega)\right], \tag{5.1}$$

where $S_{\tilde{n},\tilde{E}}(k,\omega)$ is the complex cross spectrum between density and electric field fluctuations, $\Re$ denotes real part of cross spectrum and $k_{Nyq.}$ and $\omega_{Nyq.}$ denote Nyquist wavenumber and frequency, respectively. The, k - ω resolved particle flux is given as,

$$\Gamma_r(k,\omega) = \frac{2}{B}\gamma_{\tilde{n},\tilde{E}}(k,\omega) \mid P_{\tilde{n}}(k,\omega) \mid^{1/2} \mid P_{\tilde{E}}(k,\omega) \mid^{1/2} \cos(\alpha_{\tilde{n},\tilde{E}}(k,\omega)) \tag{5.2}$$

where $P_{\tilde{a}}(k,\omega)$ indicates power spectrum of arbitrary fluctuation $\tilde{a}$, and $\gamma_{\tilde{n},\tilde{E}}(k,\omega)$ and $\alpha_{\tilde{n},\tilde{E}}(k,\omega)$ are coherence and phase delay between density and electric field fluctuations.

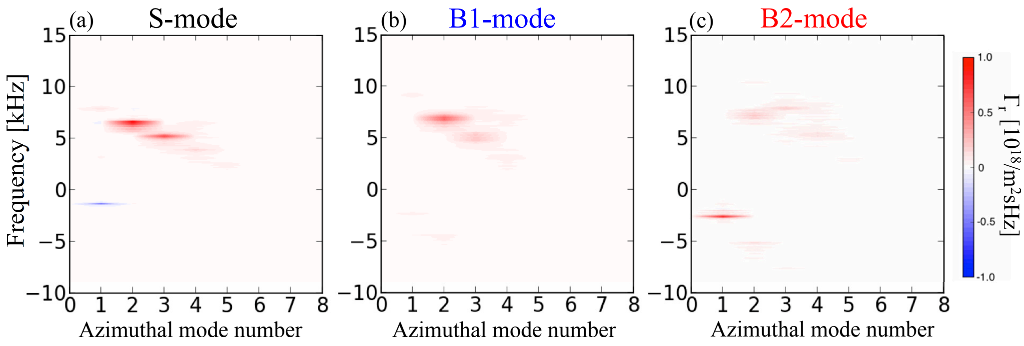

FIG. 5.16: Two-dimensional particle flux. (a), (b) and (c) represent those in S-mode, B1-mode and B2-mode. Positive flux indicates outward direction.

Figure 5.16 shows f - m ($f = \omega/2\pi$ and $m = rk$) decomposed particle fluxes in the S-mode, B1-mode and B2-mode, respectively. Positive (red) and negative (blue) signs denote direction of outward/inward particle fluxes. Positive frequency indicates that the fluctuation propagates in the electron diamagnetic drift direction. In the S-mode, the outward flux is mainly driven by drift waves with (m, f) = (2, 6.5 kHz) and (3, 5.2 kHz). The drift waves nonlinearly couple with the mediator with (m, f) = (1, -1.3 kHz). The mediator drives the inward flux. In the B1-mode, the $m = 2$ wave (drift wave) driven outward flux decreases, and the $m = -1$ wave (mediator) driven flux becomes obscure. In the B2-mode, the drift-wave-driven outward flux further reduces, and the $m = -1$ mediator-driven flux becomes outward. This suggests that the mediator changes its qualitative characteristics during the biasing.

5.3.2 Changes of fluctuations amplitude and phase relation

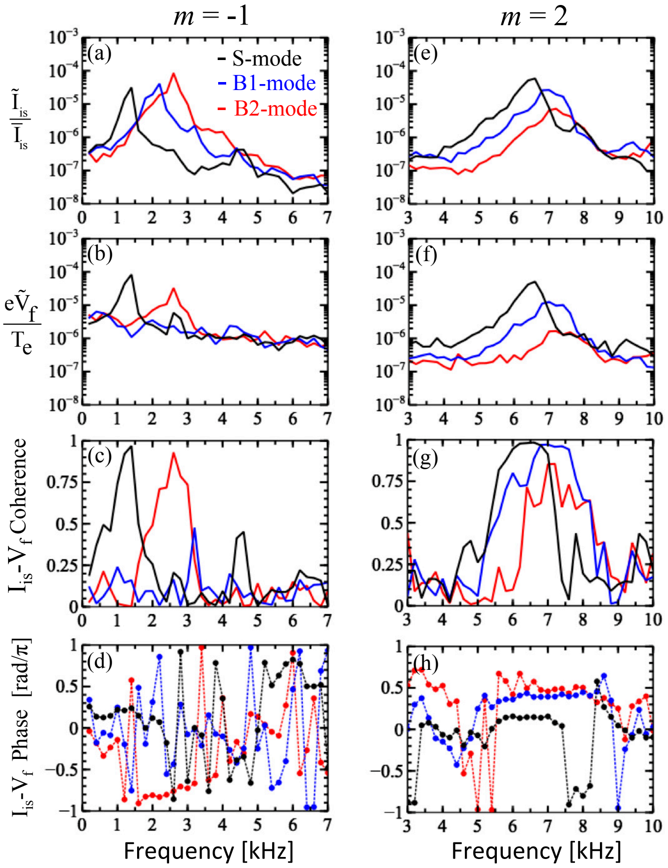

FIG. 5.17: Mode decomposed frequency spectra. (a), (b), (c) and (d) indicate those of $m = -1$ component, and (e), (f), (g) and (h) indicate those of $m = 2$ component. (a) and (e) show power spectra of ion saturation current, (b) and (f) show power spectra of floating potential. (c) and (g) show the squared cross coherence, (d) and (h) show the cross phase between $\tilde{I}_{is}$ and $\tilde{V}_f$. Black, blue and red lines indicate those in S-mode, B1-mode and B2-mode, respectively.

To understand the behaviours of the particle flux in the different 3 modes, spectra of $\tilde{I}_{is}$ and $\tilde{V}_f$ are verified. The band-pass filter in the k-domain is performed, and the $m = -1$ (mediator) and $m = 2$ mode (drift wave) are extracted. The cross spectra between two fluctuation components are calculated. Figures 5.17 (a), (b), (c) and (d) indicate the cross spectra of $m = -1$, i.e. power spectra of $\tilde{I}_{is}/\bar{I}_{is}$ and $e\tilde{V}_f/T_e$, squared coherence and cross phase between $\tilde{I}_{is}$ and $\tilde{V}_f$, respectively.

Black, blue and red lines denote the plots in the S-mode, B1-mode and B2-mode.

In the S-mode, power spectra of $\tilde{I}_{is}$ and $\tilde{V}_f$ have a maximum at f = 1.3 kHz, and the squared coherence is very high at the frequency. The phase difference between $\tilde{I}_{is}$ and $\tilde{V}_f$ ($\alpha_{\tilde{I}_{is}\tilde{V}_f}$) is 0.23$\pi$, corresponding to $\alpha_{\tilde{n}\tilde{E}}$ = 0.73π. In the B1-mode, power spectrum of $\tilde{V}_f$ doesn't have any clear peaks. Then, the coherence is low. Because of the low coherence, particle flux driven by m = -1 wave becomes almost zero. In the B2-mode, a peak appears in the power spectrum of $\tilde{V}_f$ at f = 2.6 kHz, and coherence becomes high. Phase difference of $\alpha_{\tilde{I}_{is}\tilde{V}_f}$ is -0.81π, corresponding to $\alpha_{\tilde{n}\tilde{E}}$ = -0.31π. The change of sign of the phase means inversion of direction of flux.

Concerning drift waves, the power spectrum of the m = 2 drift waves has a peak at 6.5 kHz in the S-mode. The phase difference of $\alpha_{\tilde{I}_{is}\tilde{V}_f}$ is 0.16π, corresponding to $\alpha_{\tilde{n}\tilde{E}}$ = -0.36π, which is a typical value for drift waves. During the biasing, the power spectra decrease in the B1-mode, and further decrease in the B2-mode. Cross coherence tends to decrease during the biasing. The phase relation changes from 0.16π to 0.36π during the biasing. Although the phase shift during the biasing has effects to enhance outward flux, reduction of power spectra has a stronger impact on the reduction of the particle flux and thus drift-wave-driven flux reduces in this experiment.

Relation between fluctuations power and particle flux are summarized in a diagram (in Fig. 5.18). Drift-wave (m = 2) driven particle flux decreases as decrease in fluctuations power. On the other hand, flux driven by the m = -1 mode becomes 0 due to the decrease in fluctuations power and reversed its direction with recovery of fluctuations power.

The qualitative feature of the turbulence becomes visible with Lissajous diagram of density and floating potential fluctuations. Figure 5.19 shows the Lissajous diagram of $m = 2$ and $m = -1$ waves, and black, blue and red lines denote

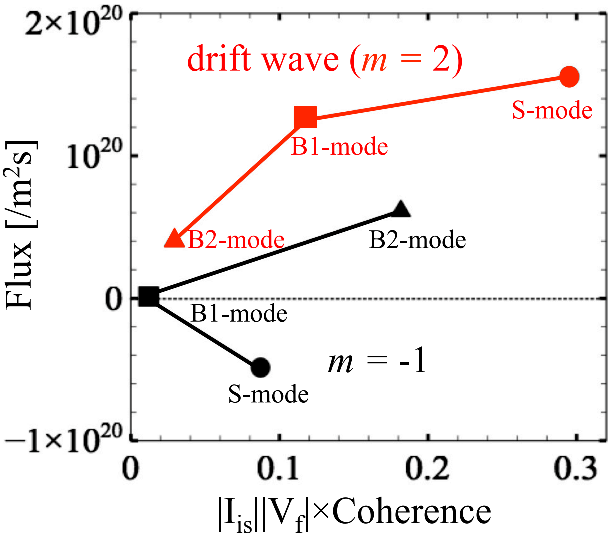

FIG. 5.18: Relation between fluctuations power spectrum and particle flux for $m = -1$ mediator and $m = 2$ drift wave. Black circle, square and triangle symbols indicate those in S-mode, B1-mode and B2-mode, respectively.

those in the S-mode, B1-mode and B2-mode respectively. The $m = 2$ wave, trajectory rotates in the same direction (counter-clockwise direction), which corresponds to the same direction of fluxes. During the biasing, the amplitude of fluctuations decreases, while the phase relations changes to enhance the positive fluxes. The area of closed trajectory is proportional to magnitude of flux, thus fluxes driven by the $m = 2$ wave decrease during the biasing, accompanying with decrease in the fluctuation amplitudes. Changes in the phase shift have small impact on the decrease in flux. The $m = -1$ wave in the S-mode and B2-mode rotates in different directions (counter-clockwise direction in the S-mode and clockwise direction in the B2-mode). The observation indicates that the directions of $m = -1$ wave-driven flux are different in different plasma modes. In addition, density/potential fluctuation increases/decreases from the S-mode to B2-mode. In the B1-mode, the potential fluctuation of the m = -1 mode disappears, then the flux becomes almost zero. For the $m = 2$ mode, the ratios in the B1/B2 modes of area to that in the S-mode are 0.86 and 0.28, which is consistent with those

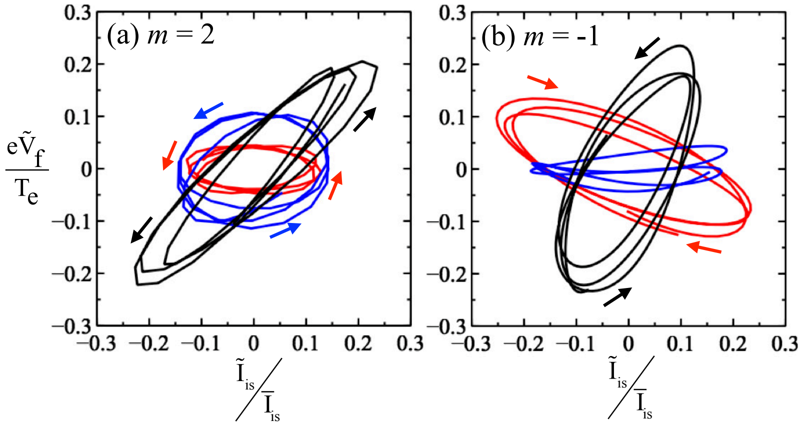

FIG. 5.19: Lissjous diagrams between ion saturation current fluctuation and floating potential fluctuation. Those for $m = 2$ waves and $m = -1$ waves are shown. Black, blue and red lines correspond to the S-mode, B1-mode and B2-mode, respectively. Colored arrows denote the direction of rotation.

estimated from the spectra indicated as Fig.5.18, 0.85 and 0.22. For the $m = -1$ mode, the ratio of area for the m = -1 mode is 1:1.2 (S-mode, B2-mode), while the ratio estimated from Fig. 5.18 is 1:1. These facts strongly support that the turbulence can form different states in the PANTA plasma during the biasing.

Chapter 6

Conclusion

The experimental observation of streamer has been really rare in spite of the importance. In particular, the real shape of streamer and its transport process have been unknown. This thesis focuses on the basic experimental observation of streamer. Advanced analytical methods, e.g., azimuthal mode analysis, wavelet-bicoherence and conditional averaging technique are first applied on the streamer. The streamer is studied in terms of its nonlinearity, transport process and response to the electric field. Here, the summary and the conclusion of the thesis are described.

(i) The nonlinear waveform of streamer is revealed

Since the streamer is nonlinearly evolved structure, there real waveform should contain nonlinearity. By using the conditional averaging, the typical waveforms of streamer and mediator are extracted. It is found that both waves are nonlinear waves, and satisfy the characteristics of solitons, i.e., the amplitude increases with squared of the parameters of localization width. The discovery is that the two different kinds of solitons, streamer and mediator, co-exist in the plasma.

(ii) The streamer-driven particle flux is investigated

In decades, the streamer has been expected to enhance transport, since streamer is radially elongated. The conditional averaging is applied to investigate the structure of the streamer and the accompanied particle flux simultaneously. The obtained patterns of the particle flux is found to follow the shape of the streamer which is radially elongated and azimuthally localized, and show to enhance the radial transport. The instantaneous maximum flux is about two times larger than the time averaged value, and the time scale of the flux is one-order faster than the diffusive transport. The occurrence of the streamer of larger transport deviates from the Gaussian, but should obey the power low. The structures of flux patterns are generated not only through the amplitude modulation, but also through phase modulation. Moreover, streamer-driven flux patterns are composed of DWs and mediator flux, and the mutually-induced flux components are important for the localization of the flux. These are the first experimental observations of streamer-driven flux.

(iii) The verification study of conditional averaging is performed

For obtaining the above-mentioned results, the validation of the conditional averaging is performed. In the conditional averaging process, determination of the trigger is a crucial issue. In this thesis, three methods to determine the trigger are introduced. The validation of the methods is made for the intermittent and non-monotonically increasing bursts observed in the I- mode of ASDEX-U. The study reveals that the template method should have excellent property, compared to the usual ones using the threshold to determine the trigger time. The verification studies of conditional averaging technique assure the analytical results of streamer practically.

(iv) The effect of electric field to the streamer is observed

It is known that the radial electric fields can suppress the turbulence by the sharing effect. Hence, for the candidate of the streamer control, the experiment to generate the electric field with end-plate biasing is carried out, and the streamer responses are observed. The end-plate biasing provides the strong shear of radial electric field, which is only localized at the end region of the axial direction. During the biasing, the DWs amplitudes are reduced with the nonlinear interaction between DWs and mediator, while the higher harmonics of the mediator increased. It is found that the particle flux is also reduced during the biasing. The possibility of streamer control through biasing experiment is indicated.

The experimental observation of streamer clarified about the streamer structure, transports and the response toward electric field. In addition to the confirmation of the streamer character, these results can contribute to the progress in the theory and simulation predictions of streamer. The understanding of the basics of streamer provides benefits to the progress of fusions and basic plasma physics.

Acknowledgment

First of all, I am deeply thankful to my supervisor, Professor Akihide Fujisawa. His continuous advices and heartening supports helped me in many situations. He has given me a chance to spend my doctor course under the ideal researching environment, e.g., open for discussions, new measurement tools and possible to do experiments whenever I want. Moreover, he always accept my research projects positively and thus I could do my works relaxing and enjoying. At the experiments in PANTA, I really express my gratitude to Professor Sigeru Inagaki. His gentle and patient teachings are my research basics. I could never complete this thesis without his supports. I would like to express my special thanks to Professor Sanae Itoh and Kimitaka Itoh for their great supports and encouragements. Their advices are always lead me to the right way and everything are benefits for me. I would like to express my gratitude to the experimental team members, Associated Professor T. Yamada, Associated Professor Y. Nagashima, Associated Professor H. Arakawa, Assistant Professor T. Kobayashi and Dr. K. Yamasaki, for their kind supports and guidance. I am deeply grateful to Assistant Professor M. Sasaki and Associated Professor Y. Kosuga, for their continuous guidance in theoretical studies and many discussions. I would like to express my thankfulness to Associate Professor N. Kasuya, Assistant Professor K. Ohsawa, and technical staff Mr. T. Mutaguchi. I would like to appreciate to the Proffessor N. Hayashi and Associated Proffessor T. Ido, for their great advisements to write this thesis. Special thanks

is for Associated Professor Y. Ngashima, who helps the revision of this thesis. As for the work in ASDEX-U, I am deeply thankful to Professor U. Stroth, Dr. G. Birkenmeier, Dr. T. Happel, Dr. P. Mantz and Dr. C. Moon.

I would like to express my appreciation to my Lab. members, especially for Mr. K. Hasamada, Mr. Y. Kawachi, Mr. Y. Iwasaki, Mr. H. Mastuo and Mr. H. Uehara. I have enjoyed campus life with their friendly help. I express my special thanks to Ms. H. Sugitani, Ms. Y. Hieida and Ms. Funaki for their kind supports. Finally, I would like to thank my family for their continuous supports.

Bibliography

[1] K. Miyamoto, *Plasma Physics and Nuclear Fusion, in Japanese* (Tokyo Univ. 2004).

[2] F. F. Chen, *Introduction to Plasma Physics and Controlled Fusion* (Plenum Press, 1984).

[3] K. Ikeda, *Nucl. Fusion* **47**, (2007).

[4] R. J. Hawryluk, *Phys. Plasmas* **5**, 1577 (1998).

[5] K. Itoh *et al., Transport and Structural Formation in Plasmas* (Institute of Physics, 1999).

[6] M. Ottaviani *et al., Phys. Plasmas* **6**, 3267 (1999).

[7] B. Labit *et al., Phys. Plasmas* **10**, 126 (2003).

[8] K. Ida *et al., Nucl. Fusion* **55**, 013022 (2015).

[9] N. Tamura *et al., Phys. Plasmas* **12**, 110705 (2005).

[10] S. Inagaki *et al., Nucl. Fusion* **53**, 113006 (2013).

[11] S. Sugita *et al., Plasma Phys. Control. Fusion* **54**, 125001 (2012).

[12] C. Z. Cheng *et al., Phys. Rev. Lett.* **38**, 708 (1977).

[13] H. Tennekes *et al., A First Course in Turbulence* (MIT Press 1972).

[14] N. Yokoi *et al., Turbulence and Flows, in Japanese* (Baifukan 2008).

[15] P. H. Diamond *et al., Plasma Phys. Control. Fusion* **47**, R35 (2005).

[16] A. Fujisawa, *Nucl. Fusion* **49**, 013001 (2009).

[17] A. Fujisawa *et al., Phys. Rev. Lett.* **93**, 165002 (2004).

[18] D. K. Gupta *et al., Phys. Rev. Lett.* **97**, 125002 (2006).

[19] H. Xia *et al., Phys. Rev. Lett.* **97**, 255003 (2006).

[20] G. S. Xu *et al., Phys. Rev. Lett.* **91**, 125001 (2003).

[21] H. Biglary *et al., Phys. Plasmas* **2**, 1 (1998).

[22] G. R. Tynan *et al., Phys. Plasmas* **8**, 2691 (2001).

[23] A. Fujisawa *et al., Plasma Phys. Control. Fusion* **49**, 211 (2007).

[24] M. Xu *et al., Phys. Rev. Lett.* **108**, 245001 (2012).

[25] Z. Lin *et al., Science* **281**, 1835 (1998).

[26] T.-H. Watanabe *et al., Phys. Rev. Lett.* **100**, 195002 (2008).

[27] M. G. Shats *et al., Phys. Rev. Lett.* **90**, 125002 (2003).

[28] G. D. Conway *et al., Phys. Rev. Lett.* **106**, 065001 (2011).

[29] T. Estrada *et al., Phys. Rev. Lett.* **107**, 245004 (2011).

[30] G. S. Xu *et al., Phys. Rev. Lett.* **107**, 125001 (2011).

[31] L. Schmitz *et al., Phys. Rev. Lett.* **108**, 155002 (2012).

[32] J. F. Drake *et al., Phys. Rev. Lett.* **61**, 2205 (1988).

[33] F. Jenko *et al., Phys. Plasmas* **7**, 1904 (2000).

[34] W. Dorland *et al., Phys. Rev. Lett.* **85**, 5579 (2000).

[35] S. Shampeaux *et al., Phys. Lett. A* **288**, 214 (2001).

[36] O. D. Gurcan *et al., Phys. Plasmas* **11**, 4973 (2004).

[37] Y. Kosuga, *Phys. Plasma* **24**, 122305 (2017).

[38] N. Kasuya *et al., Phys. Plasmas* **15**, 052302 (2008).

[39] Z. Lin *et al., Phys. Plasmas* **12**, 056125 (2005).

[40] P. Beyer *et al., Phys. Rev. Lett.* **85**, 4892 (2000).

[41] K. Nozaki *et al., J. Phys. Soc. Jpn.* **46**, 991 (1979).

[42] Y. Hamada *et al., Phys. Rev. Lett.* **96**, 115003 (2006).

[43] H. Arakawa *et al., Plasma Phys. Control. Fusion* **52**, 105009 (2010).

[44] T. Yamada *et al., Nature Phys.* **4**, 721 (2008).

[45] T. Yamada *et al., Phys. Rev. Lett.* **105**, 225002 (2010).

[46] S. Inagaki *et al., Sci. Rep.* **6**, 22189 (2016).

[47] N. Dupertuis *et al., Plasma Fusion Res.* **12**, 1201008 (2017).

[48] Y. Kawachi *et al., Plasma Fusion Res.* **13**, 3401105 (2018).

[49] T. Kobayashi *et al., Plasma Fusion Res.* **6**, 2401082 (2011).

[50] K. Hasamada *et al., Plasma Fusion Res.* **12**, 1201034 (2017).

[51] S. Oldenburger *et al., Plasma Phys. Control. Fusion* **54**, 055002 (2012).

[52] T. Kobayashi *et al., Phys. Plasmas* **22**, 112301 (2015).

[53] C. Holland *et al., Phys. Rev. Lett.* **96**, 195002 (2006).

[54] R. Hong *et al., Phys. Rev. Lett.* **120**, 205001 (2018).

[55] T. A. Carter *et al., Phys. Plasmas* **13**, 010701 (2006).

[56] D. A. Schaffner *et al., Phys. Rev. Lett.* **109**, 135002 (2012).

[57] C. Schroder *et al., Phys. Rev. Lett.* **86**, 5711 (2001).

[58] O. Grulke *et al., New J. Phys.* **4**, 67 (2002).

[59] T. Windisch *et al., Phys. Plasmas* **13**, 122303 (2006).

[60] B. Song *et al., Phys. Rev. Lett.* **70**, 2407 (1993).

[61] Th. Pierre *et al., Phys. Rev. Lett.* **92**, 065004 (2004).

[62] Y. Nagashima *et al., Phys. Plasmas* **16**, 020706 (2009).

[63] H. Arakawa *et al., Sci. Rep.* **6**, 33371 (2016).

[64] T. Kaneko *et al., Phys. Rev. Lett.* **90**, 125001 (2003).

[65] C. Moon *et al., Phys. Rev. Lett.* **111**, 115001 (2013).

[66] K. Terasaka *et al., Phys. Plasmas* **23**, 112120 (2016).

[67] M. Ignatenko *et al., J. Phys. Soc. Jpn.* **46**, 1680 (2007).

[68] T. Kobayashi *et al., Plasma Fusion Res.* **12**, 1401019 (2017).

[69] N. Kasuya *et al., Phys. Plasmas* **25**, 012314 (2018).

[70] M. Sasaki *et al., Phys. Plasmas* **24**, 112103 (2017).

[71] M. Sasaki *et al., Nucl. Fusion* **54**, 114009 (2014).

[72] H. Arakawa *et al., Plasma Phys. Control. Fusion* **53**, 115009 (2011).

[73] H. M. Mott-Smith *et al., Phys. Rev.* **28**, 727 (1926).

[74] S. Teii, *Fundamental Engineering of Plasmas, in Japanese* (Uchda Rokakuho, 1995).

[75] K. Kawashima *et al., Plasma Fusion Res.* **6**, 2406118 (2011).

[76] T. Klinger *et al., Phys. Plasmas* **4**, 3990 (1992).

[77] C. Schroder *et al., Phys. Plasmas* **11**, 4249 (2004).

[78] U. Stroth *et al., Phys. Plasmas* **11**, 2558 (2004).

[79] T. Yamada *et al., Rev. Sci. Instrm.* **78**, 123501 (2007).

[80] Y. Nagashima *et al., Rev. Sci. Instrm.* **77**, 045110 (2006).

[81] T. Kanzaki *et al., Plasma Fusion Res.* **11**, 1201091 (2016).

[82] A. Fujisawa *et al., Plasma Phys. Control. Fusion* **58**, 025005 (2016).

[83] H. Sinohara *et al., Introduction of reconstruction of image by using Excel, in Japanese* (Iryoukagakusya, 2007).

[84] K. Yamasaki *et al., Rev. Sci. Instrm.* **88**, 093507 (2017).

[85] M. Hino, *Spectrum analysis, in Japanese* (Asakurasyotenn, 1977).

[86] C. Torrence *et al., Bull. Am. Meteorol. Soc.* **79**, 61 (1998).

[87] Y. Nagashima *et al., Phys. Rev. Lett.* **95**, 095002 (2005).

[88] G. R. Tynan *et al., Phys. Plasmas* **11**, 5195 (2004).

[89] Y. Kim *et al., IEEE Trans. Plasma Sci.* **PS-7**, 120 (1979).

[90] G. Y. Antar *et al., Phys. Plasmas* **10**, 419 (2003).

[91] T. Kobayashi *et al., Plasma Phys. Control. Fusion* **54**, 115004 (2012).

[92] T. Happel *et al., Phys. Rev. Lett.* **102**, 255001 (2009).

[93] H. W. Muller *et al., Nucl. Fusion* **51**, 073023 (2011).

[94] G. Birkenmeier *et al., Plasma Phys. Control. Fusion* **56**, 075019 (2014).

[95] T. Happel *et al., Plasma Phys. Control. Fusion* **59**, 014004 (2017).

[96] F. Kin *et al., IPP report* **07**, pp1 (2018).

[97] D. G. Whyte *et al., Nucl. Fusion* **50**, 105005 (2010).

[98] F. Ryter *et al., Nucl. Fusion* **57**, 016004 (2017).

[99] F. Kin *et al., Phys. Plasmas* **25**, 062304 (2018).

[100] S. Inagaki *et al., Plasma Fusion Res.* **9**, 1201016 (2014).

[101] E. J. Powers, *Nucl. Fusion* **14**, 749 (1974).

[102] G. P. Agrawal, *Phys. Rev. Lett.* **59**, 880 (1987).

[103] F. Kin *et al., Plasma Fusion Res.* **10**, 3401043 (2015).

[104] F. Kin *et al., J. Phys. Soc. Jpn.* **85**, 093501 (2016).

[105] R. J. Taylor *et al., Phys. Rev. Lett.* **63**, 2365 (1989).

[106] C. Silva *et al., Plasma Phys. Control. Fusion* **48**, 727 (2006).

[107] S. Inagaki *et al., Jpn. J. Appl. Phys.* **36**, 3697 (1997).

[108] P. Manz *et al., Phys. Plasmas* **16**, 042309 (2009).

[109] S. Shinohara *et al., Phys. Plasmas* **9**, 4540 (2002).

[110] H. Biglari *et al., Phys. Fluids B* **2**, 1 (1990).

[111] T. Yamada *et al., Nucl. Fusion* **54**, 114010 (2014).